

PREDICTING THE RESPONSE OF AN UNDERACTUATED,
3D PRINTED PROSTHETIC HAND

By

Lucas Gallup

Bachelor of Science – Mechanical Engineering
University of Nevada, Las Vegas
2019

Master of Science in Engineering – Mechanical Engineering
University of Nevada, Las Vegas
2023

A dissertation submitted in partial fulfillment
of the requirements for the

Doctor of Philosophy – Mechanical Engineering

Department of Mechanical Engineering
Howard R. Hughes College of Engineering
The Graduate College

University of Nevada, Las Vegas
May 2024



Dissertation Approval

The Graduate College
The University of Nevada, Las Vegas

April 4, 2024

This dissertation prepared by

Lucas Gallup

entitled

Predicting the Response of an Underactuated, 3D Printed Prosthetic Hand

is approved in partial fulfillment of the requirements for the degree of

Doctor of Philosophy – Mechanical Engineering
Department of Mechanical Engineering

Mohamed Trabia, Ph.D.
Examination Committee Co-Chair

Brendan O'Toole, Ph.D.
Examination Committee Co-Chair

Janet Dufek, Ph.D.
Examination Committee Member

Woosoon Yim, Ph.D.
Examination Committee Member

Jeremy Cho, Ph.D.
Examination Committee Member

Szu-Ping Lee, Ph.D.
Graduate College Faculty Representative

Alyssa Crittenden, Ph.D.
*Vice Provost for Graduate Education &
Dean of the Graduate College*

Abstract

Predicting the Response of an Underactuated,
3D Printed Prosthetic Hand

By

Lucas Gallup

Dr. Mohamed Trabia, Examination Committee Chair
Associate Dean for Research, Graduate Studies & Computing

Dr. Brendan O'Toole, Examination Committee Co-Chair
Professor of Mechanical Engineering
University of Nevada, Las Vegas

The continuing need for hand prostheses has led to incredible developments in this area. However, due to the cost of the most sophisticated models, it is vital to develop simpler, low-cost, underactuated prostheses that can be produced rapidly. 3D printing is an important tool to achieve this goal. In particular, the 3D printed Flexy-Hand 2 has been one of the most common low-cost designs. A key feature of the Flexy-Hand 2 is its use of tendons and thermoplastic polyurethane (TPU) for joints that are strong and flexible. TPUs, however, lack a thorough understanding of their mechanical behavior, which makes it difficult to discern the forces needed to flex the prosthetic hand or to grip an object. The purpose of this research is to develop, and experimentally verify, a model that can predict the relationship between tendon forces and the flexion of the TPU joints of a prosthetic finger. First, a constitutive model for 3D printed TPU, NinjaFlex® was developed. This model accounts for the effect of filament extrusion temperature and material deposition orientations. Next, flexural tests of cantilevered specimens representing the finger joints were conducted to study the bending behavior of the TPU under realistic

conditions to simulate finger flexion. Lastly, the results of these two tasks were incorporated in a quasi-static model relating finger flexion to tendon tension inducing it. This model was verified experimentally.

Acknowledgments

The Ph.D. is often referred to as a “terminal” degree, which I find interesting as, having now obtained one, I can say that this is only the beginning of my journey. This degree has been one of the greatest challenges and achievements of my life, and yet I would be remiss if I did not give credit to those who made this possible; I have not done this alone, but with the help of so many.

To my advisors, Dr. Mohamed Trabia and Dr. Brendan O’Toole; I cannot thank you enough. Your continued patience and unwavering support of my work cannot be overstated. Thank you for your guidance and advice through challenging times, I am the researcher I am today because of it. You pushed me to be the best I could and taught me how to do so myself. I will be forever grateful for your role in my life. I would like to thank my committee members, Dr. Janet Dufek, Dr. Woosoon Yim, Dr. Jeremy Cho, and Dr. Szu-Ping Lee, for their time and advice for my dissertation.

I would like to thank the Nuclear Regulatory Committee for the Nuclear Engineering Doctoral Fellowship at UNLV. I would also like to thank the Howe Foundation for the Howe Biomedical Fellowship. I would like to thank the UNLV Graduate College for the Faculty Top Tier Doctoral Graduate Research Assistantship Grant.

I would like to thank my colleague, Youssef Fahmy, for his enthusiastic support throughout my degree. Thank you for helping me with my countless experiments, and for being there to talk through challenges. Your insight was always appreciated, and I wish you nothing short of success as you begin your Ph.D. soon.

Thank you to my friends and family, for supporting me and encouraging me. Thank you for listening to me talk endlessly about my work, and for believing in me.

Lastly, I would like to thank my wife, Lillie. There was never a doubt in your mind that I could do this, and you made sure that I knew that. Thank you for everything. Thank you for your unending patience when my work took longer than expected, thank you for your support when problems seemed unsolvable, and thank you for listening to me. No one knows this work better than me and my advisors than you do. I hope that I made you proud.

To my wife, Lillie.

Table of Contents

Abstract	iii
Acknowledgments.....	v
Table of Contents	viii
List of Tables.....	xii
List of Figures	xiv
Chapter 1: Overview	1
1.1 Workflow diagram.....	3
Chapter 2: Literature review and scope of work	4
2.1 3D printed prosthetic hands	4
2.2 Hyperelastic polymers in 3D printing.....	7
2.3 Modeling and analysis of robotic and prosthetic fingers.....	11
2.4 Scope of work.....	15
Chapter 3: Influence of 3D printing parameters on the constitutive model of hyperelastic thermoplastic polyurethane	17
3.1 Experimentation.....	18
3.1.1 Materials and preparation	18

3.1.2 Experimental setup	21
3.1.3 Data processing.....	23
3.2 Constitutive model.....	25
3.3 Results.....	25
3.3.1 Experimental results	25
3.3.2 Constitutive model results	29
3.3.3 Finite element validation	31
3.4 Discussion.....	34
Chapter 4: Characterizing the behavior of 3D printed hyperelastic thermoplastic polyurethane hand prosthetic joints	37
4.1 Specimen preparation.....	37
4.2 Bracket preparation	40
4.3 Experimental procedure	41
4.4 Image processing	42
4.5 Results.....	44
Chapter 5: Modeling the behavior of 3D printed hyperelastic thermoplastic polyurethane hand prosthetic joints	47

5.1 Analytical modeling of flexible 3D printed prosthetic joints using modified Euler-Bernoulli equations	47
5.2 Finite element analysis modeling	55
5.3 Comparison of analytical, finite element, and experimental results.....	58
Chapter 6: Deflection and experimental validation of the flexion of tendon-actuated prosthetic finger with flexible 3D printed hyperelastic thermoplastic polyurethane joints.....	64
6.1 3-digit prosthetic finger modeling	64
6.1.1 Kinematic analysis of the 3-digit prosthetic finger	65
6.1.2 Quasi-static analysis of the 3-digit prosthetic finger using the principle of virtual work	69
6.2 Experimentation.....	73
6.2.1 Material and preparation.....	73
6.2.2 Experimental setup	76
6.2.3 Data processing.....	79
6.3 Results and comparison	80
6.3.1 Measured model parameters	80
6.3.2 Experimental results	83
6.3.3 Comparison of the model and experiment.....	84

Chapter 7: Conclusion and future work	88
Appendix A: Mooney-Rivlin constitutive model derivation	91
Appendix B: Derivation of modified Euler-Bernoulli (MEB) method for flexible joints	97
Appendix C: Results of flexible beam experiment	108
Appendix D: Finger digit kinematic derivation.....	115
Appendix E: Conversion of flexible beams to torsional springs	117
References.....	123
Curriculum Vitae	135

List of Tables

Table 2.1: NinjaFlex® mechanical characteristics.....	10
Table 3.1: Test Matrix of tensile specimens	19
Table 3.2: Tensile specimen dimensions	23
Table 3.3: Measured dimensions of printed specimens (ten tensile specimens for each group)	26
Table 3.4: Mechanical properties of specimen groups	26
Table 3.5: Fitted model coefficients and fitness results.....	31
Table 3.6: Maximum tensile loads for model validation	32
Table 3.7: Model error values for each specimen group	34
Table 4.1: Bending specimen dimensions.....	39
Table 4.2: 3D printing parameters	40
Table 4.3: Loading parameters of the bending experiments	42
Table 6.1: Local coordinates of finger model	67
Table 6.2: Dimensions of the proximal and middle/distal joints	74
Table 6.3: Lulzbot® Taz Mini 2 printing parameters for finger joints	74
Table 6.4: Full finger bending experiment loading conditions.....	77

Table 6.5 Definition of the local coordinate vectors for each digit markers	81
Table 6.6 Kinematic constants used in the analytical model	82
Table 6.7 Mass of 3D printed finger digits	82
Table 6.8 Torsional spring coefficients used in the analytical model.....	82
Table 6.9: Measured dimensions and mass of experimental finger joints	83
Table B.1: Variables of MEB method.....	98
Table C.1: ID and dimensions of flexible beam joints	114
Table E.1: Nonlinear torsional stiffness coefficients and R^2 values	121
Table E.2: Nonlinear torsional stiffness coefficients and R^2 values for 3-digit finger.....	122

List of Figures

Figure 1.1: Flow chart of the work done to achieve the research goals.....	3
Figure 2.1: Flexy-Hand 2.....	7
Figure 2.2: Example of a tendon-actuated robotic hand, [39].....	11
Figure 2.3: Underactuated prosthetic finger designs: (a) a hinged finger with a single actuation tendon; (b) flexible beam joints with a single actuation tendon.....	12
Figure 3.1: 3D printed tensile specimens; (a) a dog bone specimen; (b) zoomed-in view showing discontinuities; (c) infill only specimen; (d) wall-only specimens.....	19
Figure 3.2: Lulzbot® Taz Mini 2	20
Figure 3.3: Tensile testing experiment; (a) low-force uniaxial tensile testing machine, (A) actuating DC motor, (B) load cell, (C) specimen in grips, (D) linear rail system, € ball screw; (b) specimen while being loaded.....	22
Figure 3.4: Typical phases of the tensile testing experiment; a) Infill specimen initial image; b) Infill specimen final image	24
Figure 3.5: Average and standard deviation experimental results of wall and infill region specimens at different extrusion temperatures; a) 225°C; b) 235°C; c) 250°C. The thick lines are the average values while the shaded regions represent the standard deviations	28
Figure 3.6: Stretch modulus of all specimen groups.....	29

Figure 3.7: Sample MCalibration® material curve fitting of wall region specimens printed at 225°C
..... 30

Figure 3.8: 0.25 mm mesh of tensile validation models..... 31

Figure 3.9: Sample of model validation results, model in black dotted line, experimental data in colored shaded lines 33

Figure 4.1: Specimen preparation: (a) variables of the specimens; (b) specimen representation in the Cura Lulzbot® edition software; (c) printing a specimen using the Lulzbot Taz Mini 2® 38

Figure 4.2: A loaded specimen between brackets 41

Figure 4.3: Specimen image processing: (a) images were cropped and binarized; (b) the cylindrical ends were identified and removed, and the edges of the middle portion were determined; (c) two sets of equally spaced points were created on the top (blue) and bottom (red) borders and averaged to determine the neutral axis (yellow); (d) the top and bottom edges and the neutral axis were fitted with 2nd order polynomials, and the intersection of the neutral axis and the right cylindrical section was used for the tip point deflection (pink)..... 43

Figure 4.4: Experimental deflection in the x and y direction; (a) a relatively stiff Specimen 15 x deflection; (b) a relatively stiff Specimen 15 y deflection; (c) a relatively flexible Specimen 1 x deflection; (d) a relatively flexible Specimen 1 y deflection 45

Figure 5.1: Specimen diagrams; a) diagram of experimental system: P_w is the load applied, P_B is the load applied by the weight of the bracket. The lengths a_B and a_W represent the moment arms

for each respective load. Angle θ is equivalent to $\tan^{-1}(v_x(l))$ at the tip of the beam; b) retraction of a differential element on inextensible beam..... 48

Figure 5.2: Tensile stress-strain curve for NinjaFlex®, [9] 54

Figure 5.3: FEA setup of bending experiments, the green represents the free end bracket, the blue area represents the wall region of the specimen, and the gray area represents the infill region of the specimen; (a) typical mesh density); (b) image of zoomed mesh; (c) applied forces 57

Figure 5.4: Comparison of experimental results and MEB method: (a) a relatively stiff Specimen 15; (b) a relatively flexible Specimen 1 59

Figure 5.5: Comparison of experimental results to the FEA method; (a) a relatively stiff Specimen 15; (b) a relatively flexible Specimen 1 60

Figure 5.6: Deviation of MEB and FEA with respect to average experimental results; (a) Specimens with $l=10$ mm; (b) Specimens with $l=15$ mm 62

Figure 6.1: Prosthetic finger diagram; (a) original 3D printed finger; (b) diagram of original finger; (c) diagram of finger with torsional springs 65

Figure 6.2: Diagram of local frames and coordinate vectors 66

Figure 6.3: Diagram of modified finger joints 74

Figure 6.4: Painted ends of the finger joints and markers; (a) raised markers on digits; (b) painted markers and joint ends 75

Figure 6.5: Base bracket design; (a) CAD model; (b) printed bracket 76

Figure 6.6: Assembled finger bending experiment setup; (a) finger with diagram: A) finger digits; B) finger joints; C) base bracket; D) hook for holding applied weights; (b) typical deformed finger 77

Figure 6.7: Experimental setup of 3-digit prosthetic finger experiment 78

Figure 6.8: Image processing of finger deflection experiments; (a) cropped image from pulled from video; (b) Image converted to gray scale; (c) Image converted to binary and markers isolated; (d) markers identified in image 79

Figure 6.9: Diagram of marker locations in full finger model 80

Figure 6.10: Markers for image processing flexion; (a) labeled markers on finger digits; (b) mean deflection results for all nine trials 84

Figure 6.11: Comparison of finger model and prosthetic finger; a) unloaded initial condition; b) flexion under 1.06 N tension; c) final flexion under 2.43 N tension. The red line represents the finger digits from the model, the green dots represent the model markers, the black lines represent the model tendons, and the blue error bars represent the experimental markers .. 85

Figure 6.12: Comparison of the experimental results and the modeling marker coordinates .. 86

Figure 6.13: Flexion error of markers on each digit; a) body 2, proximal digit markers; b) body 3, middle digit markers; c) body 4, distal digit markers 86

Figure B.1: Diagram of loads on flexible joints 97

Figure B.2: Simplified system diagram 98

Figure B.3: Differential unit for retraction calculation	106
Figure C.1: Experimental results of flexible beam joints, in the x (i) and y (ii) directions; (a) specimen 1; (b) specimen 2; (c) specimen 3; (d) specimen 4; (e) specimen 5; (f) specimen 6; (g) specimen 7; (h) specimen 8; (i) specimen 9; (j) specimen 10; (k) specimen 11; (l) specimen 12; (m) specimen 13; (n) specimen 14; (o) specimen 15; (p) specimen 16; (q) specimen 17; (r) specimen 18	108
Figure D.1: Global position matrices of an arbitrary point P^i	115
Figure E.1: Representation of the hinge/joint nonlinear spring equivalent of a beam joint....	117
Figure E.2: Calculation of angular deflection	118
Figure E.3: Calculation of equivalent moment for torsional stiffness.....	119
Figure E.4: Example of angular displacement with respect to moment.....	120
Figure E.5: Moment-angle plot for finding nonlinear stiffness coefficients of proximal and middle/distal joints in the 3-digit finger modeling; (a) proximal joint; (b) middle/distal joint	122

Chapter 1: Overview

Early hand prostheses were intended to replace the missing limb segment for cosmetic purposes or to increase limb functionality for the user, but were limited by available technology, materials, and techniques. Since then, recent developments in this field have allowed for all kinds of hand prosthetics to become more complex, functional, and realistic. For example, haptic feedback can provide vibration to simulate touch, and thermal sensors can allow users to feel the temperature of the object they are grasping, [1,2]. Similarly, more anthropomorphic designs have been developed which have near-human level articulation and motion, [3]. However, the high cost of modern prosthetics, ranging from a few thousand to hundreds of thousands of dollars [4], restricts the users from access to advanced options, especially for families of children who will often outgrow their prostheses multiple times throughout their life, causing costs to stack. This problem becomes even more prevalent as the number of children born with underdeveloped upper limbs increases by approximately 2000 children annually, [5]. Therefore, there needs to be research and development focused specifically on affordable, accessible hand prostheses. Specifically, underactuated hand prostheses that do not require electronic control and are open source to allow for customization and alterations for repeat users. 3D printing provides the opportunity for almost anyone to design and build their own hand prosthesis at an affordable rate and with very little startup time and experience needed. Customized prosthetics could address the most common reasons for prosthesis adoption: functionality and cost [6].

The expansion and potential of 3D printing has led to advancements in many aspects, from technology, to methodology, to available materials, which in turn has helped develop 3D printing

methods. Over the last few decades, 3D printers have increased in accuracy, size, and speed, while decreasing cost. This means that more people and researchers have access to printers and can design their own objects to print. The downside to this rapid development is that materials and impact of the manufacturing processes have not all been well-understood, especially since recent studies show that the printing parameters have been found to have a definite impact on the mechanical performance of a 3D printed object, [7–10]. Therefore, a model of both the filament material and the printing parameters used is required to fully understand a 3D printed object, particularly one that has to perform functions and withstand certain stress levels like a prosthetic hand.

In this study, we investigated the 3D printed TPU, which is commonly used for joints in underactuated upper limb prosthetics. The study started by identifying constitutive model for the material. Effects of various 3D printing parameters were considered. The constitutive model was incorporated in finite element analysis to predict the behavior of these joints in bending. The results of the FEA were compared with experiments. Finally, the information obtained about 3D printed TPU joints was incorporated in a quasi-static model that described the relation between tendon tension and the flexion of a three-digit prosthetic finger. Experimental verification indicated that this model is accurate.

1.1 Workflow diagram

The flowchart below represents the major steps that were needed to complete the goals of this research, Figure 1.1.

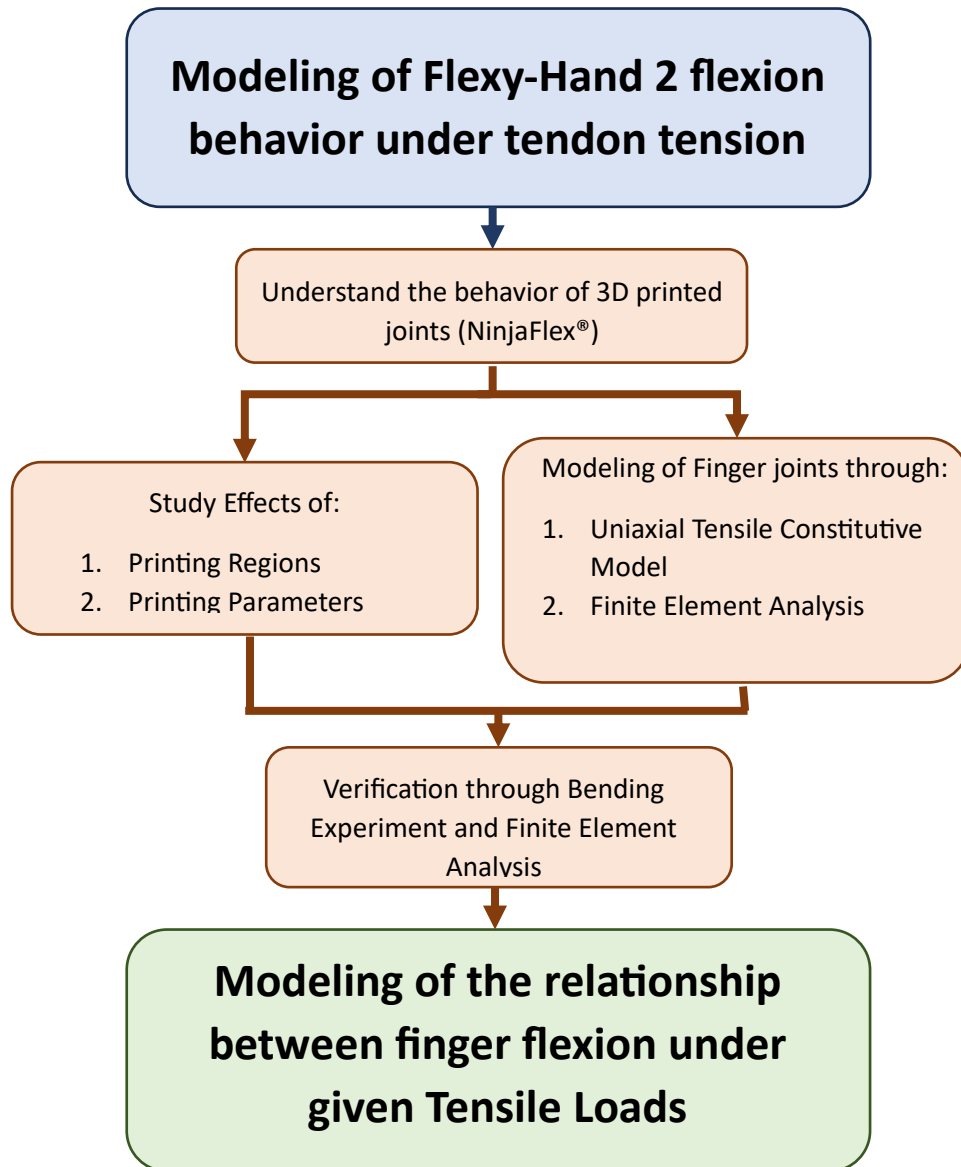


Figure 1.1: Flowchart of the work done to achieve the research goals

Chapter 2: Literature review and scope of work

In this literature review, we will introduce the topic of 3D printed prosthetic hands as well as the two common actuation methods: tendon and 4-bar mechanism. Next, we will discuss 3D printing polymer filaments commonly used in prosthetics and the characterization studies conducted thus far. Impactful and relevant research will be reviewed, and key gaps will be identified and highlighted.

2.1 3D Printed prosthetic hands

Prosthetic hands have been used to help people as early as the Roman Empire, [11]. Since then, developments in materials and technology have allowed for great leaps in design and functionality. The advent of 3D printing has ushered in a new vector of prosthetic design. Rapid, small batch, easily accessible machines allow for research and industry production of new prosthetic hands. Prosthetic hand designs aim to be anthropomorphic, mimicking human anatomy, [3,12–17], containing the same three phalanges: proximal, middle, and distal. Two common features of current 3D printed prosthetic hand designs are the actuation source and the actuation method. The actuation source is what provides the energy needed to move the fingers, such as the user's body, a motor, or pneumatics. The actuation method is the mechanism through which the source causes the hand to move, namely tendons or multi-bar mechanisms.

Of the actuation sources, there are two common options: body driven, and motor driven. Body driven hands utilize the user's intact body motions and forces for actuation of the prosthetic hand and tend to be the most utilized actuation source for prostheses, [18]. When a user actuates

a limb the motion transfers to the prosthetic hand, often through some amount of wire, tendons, and cords like with the Cyborg Beast, Flexy Hand 2, Phoenix Hand, and Falcon Hand [19–22]. Commonly, these hands are designed for people with underdeveloped hands and therefore the user's wrist actuation acts as the actuation source. Body-driven prosthetic hands benefit from simpler, and therefore less expensive, designs since they do not need batteries, motors, and controllers. However, they have a limited output force proportional to the user's own strength and range of motion. Prosthetic hands can also be motor driven. Onboard motors are attached to the actuation method and bend the fingers, such as with the Mark V hand, [23]. Motor driven hand prosthetics provide higher force output and reduce the need for input force from the user. Major downsides to motor-actuated prostheses come in the forms of the need for maintenance, cost, and weight, [18].

Two of the most common actuation methods are tendons and multi-bar mechanisms. Tendons are characterized by one or more wires or cables running the length of the finger through the digits. Pulling on the wire causes the finger to curl in order to compensate for the shorter length of tendon. Tendon actuation is common among prosthetic hands, [19,21–26]. This method is often used due to its high functionality and ease of use in simple prosthetic designs, as well as in advanced, anthropomorphic hands due to the ability to actuate higher degrees of motion by adding more tendons. The tendons are typically light weight and take up very little space, allowing for a high number of wires with little increase in weight or hand size. The second actuation method is a multi-bar mechanism. This design is not as common due to the fixed range of motion. Typically, a multi-bar mechanism is designed to be anthropomorphically accurate while allowing for full finger closure, [27–30]. These designs benefit from a predictable movement of the finger

under actuation, as well as a typically more robust design. However, the predictable, fixed motion limits the possible grasping techniques and holdable objects due to the set digit rotation upon actuation.

The Flexy-Hand 2 is a unique 3D printed prosthetic hand, Figure 2.1, [21]. It is designed to be utilized by those with under-developed or partially amputated hands. The hand is body-driven; a gauntlet is fixed to the user's forearm, and tendons run from the gauntlet through the back side of the prosthetic hand. These tendons then go through the palmer side of the fingers, as a typical tendon actuated prosthetic hand does. What sets the Flexy-Hand 2 apart from typical prosthetics is the novel method of finger joint design. A typical finger joint in a prosthetic is composed of a number of revolute joints. These types of joints fixed the rotation about a single axis and require extra actuation or energy storage to move and return to the neutral position. For instance, a tendon driven finger will use the wire for flexion but needs either another wire or spring to return the finger to a neutral position. This increases the number of parts necessary, as well as the weight. The Flexy-Hand 2 uses a hyperelastic cantilever beam as the joint to overcome this challenge. The joint beam is 3D printed from a thermoplastic polyurethane (TPU) filament called NinjaFlex®, which can undergo the large deflection bending common in finger flexion without experiencing permanent deformation. This configuration presents a unique solution to creating a functional, low-cost prosthetic hand design.

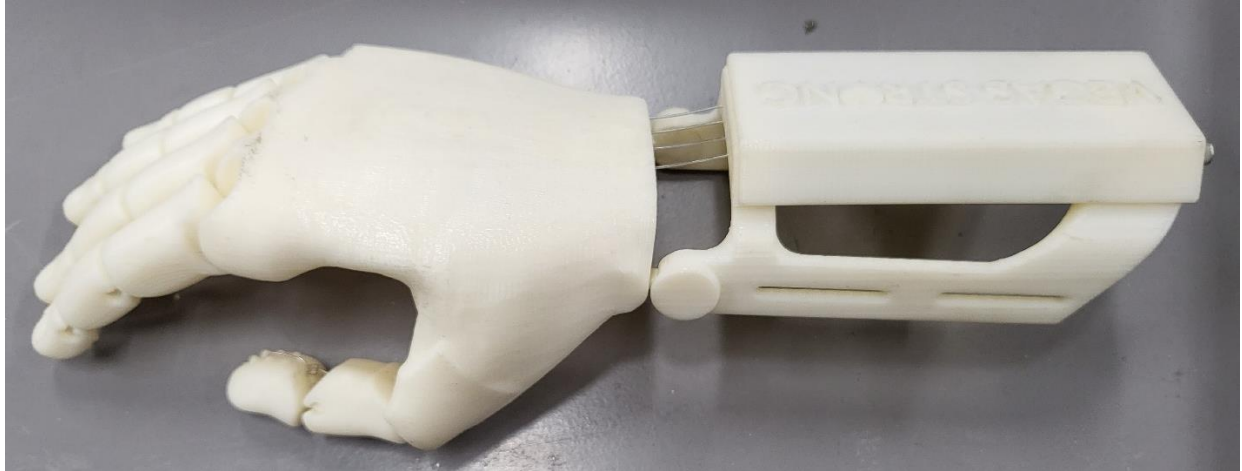


Figure 2.1: Flexy-Hand 2

2.2 Hyperelastic polymers in 3D printing

Scientific and technological advancements have allowed the use of polymer synthesis to develop materials for many applications. An example of these new materials is the hyperelastic thermoplastic polyurethanes (HTPUs). HTPUs offer the manufacturing advantage of being processed as a thermoplastic while maintaining rubber-like properties due to their molecular structure, which contains two specific regions: soft and hard. The soft regions allow for high flexibility, while the hard ones contribute to preventing permanent deformation, tensile strength, and hysteresis of the material, [31,32]. This combination provides HTPUs with a composite-like behavior that is hyperelastic and nonlinear, [32].

Simultaneously, hardware development has allowed 3D printing to speed up the process of developing prototypes and part production, especially when a relatively small number of components are needed. However, incorporating 3D printing in the industry has been limited by

changes that the materials, especially polymers, experience during material deposition. These changes affect the mechanical behavior as compared to traditionally manufactured materials because 3D printing introduces a plethora of factors including: print orientation, which is the angle and direction of an object in the printer workspace; infill raster angle, which describes the angle of the material that composes the inner volume of an object; infill density, which is the amount of material used to fill the inner closed volume of an object typically denoted from 0-100% infill; and shell thickness, which is the thickness of the outer-most surface of a printed object. In the following, a brief overview of research in this area is presented.

Some mechanical properties of hyperelastic polymers can be readily determined using uniaxial tensile testing. A brief overview follows of relevant research in this area. By 3D printing dog-bone shaped specimens from Elastosil M4061 and translucent soft silicones, stress-strain curves as well as elastic moduli were obtained, [33]. The effects of infill density on uniaxial tensile strength of 3D printed Polylactic acid (PLA) specimens were considered, [34]. Increasing the infill density consistently increased the modulus of elasticity, yield strength, and ultimate strength. The variation in the mechanical characteristics of Polyamide 12 (PA12 or Nylon 12) was studied with respect to changing the laser power and hatch orientation; it was found that 95% full power at 0° with respect to the printer's x-axis resulted in higher tensile strength, modulus of elasticity, and elongation at break, [35]. The effects of varying the printer platform temperature and print speed were studied for Onyx, a Nylon filament mixed with carbon fibers, [36]. It was found that increasing either printer platform temperature or print speed caused an increase in modulus of elasticity and tensile strength. The effects on tensile properties of polyetherimide (PEI) caused by

print speed and nozzle temperature were studied, and it was found that increasing either parameter caused a decrease in modulus of elasticity, [37].

The influence of infill raster angle on various polymers including NinjaFlex® was assessed under uniaxial tensile loading, [8]. It was found that as the raster angle approached the loading direction, these materials' moduli of elasticity increased. The ultimate tensile strength of NinjaFlex® increased as the raster angle approached the loading direction. The infill density of NinjaFlex® was varied, and its effects on hardness, maximum stress, and flexure force were studied, indicating that the hardness increased as the infill density increased, [38]. The maximum stress increased with infill density for NinjaFlex®. The flexural force increased to 70/80% infill density, then dropped slightly for the higher density values. The effects of infill density were evaluated on 3D printed NinjaFlex® hollow cells with gyroid units of varying unit sizes while under compressive loads, [10]. The resulting stress–strain curves showed that as the size of cell unit increased, the stress at any given strain decreased. Similarly, the modulus of elasticity increased as the cell size decreased. The influence of infill density and print orientation on NinjaFlex® under uniaxial tensile loading was considered with respect to ultimate strength and modulus of elasticity, [7]. When varying the printing orientation, it was found that ultimate stress increased when the printing orientation was parallel to the loading direction rather than perpendicular to it. The modulus of elasticity remained relatively constant for specimens with a print orientation parallel to the direction of loading when the infill density increased. On the other hand, specimens with a printing orientation perpendicular to the loading direction had the modulus of elasticity increase as the infill density increased. The effects of the shell thickness on NinjaFlex® 3D printed specimens with shell thickness varying between one and four filament lines were

considered, [9]. Uniaxial tensile testing showed that tensile strength and modulus of elasticity increased in proportion to the number of wall lines.

While these studies addressed important questions related to the mechanical behavior of the 3D printed polymers, they did not study the regions of the material individually, namely the infill and wall material. Rather than varying the infill density of a test specimen, the wall and infill material will be tested separately to understand their individual characteristics. These studies also show a wide variety of material characteristics, so further testing should be conducted to form a more consistent model, Table 2.1. Similarly, the behavior of 3D printed HTPUs under bending causing large deformation is not well-understood. The bending behavior of NinjaFlex® will be studied to create a more complete model.

Table 2.1: NinjaFlex Mechanical Characteristics

Source	Yield Strength, (MPa)	Ultimate Strength, (MPa)	Tensile Modulus, (MPa)	Elongation at Yield, (%)	Elongation at Break, (%)	Toughness, (m×N/m ³ × 10 ⁶)	Hardness, (Shore)
Manufacturer [15]	4.00	26.00	12.00	65.00	660	82.70	85A
Pitaru et al. [8]	2.80	-	8.51	51.85	-	-	-
Mogan et al. [9]	-	13.19	-	-	-	-	55.7D
Holmes et al. [10] 1	0.16	-	1.50	-	-	-	-
Messimer et al. [11], 25% infill	-	7.01	5.17	-	476	-	-
Messimer et al. [11], 50% infill	-	8.61	5.19	-	487	-	-
Messimer et al. [11], 75% infill	-	10.21	5.22	-	497	-	-
Messimer et al. [11], 100% infill	-	11.81	5.24	-	508	-	-
Reppel and Weinberg [12]	-	27.80	12.2	-	1200	133.40	-

1 The values reported are for gyroid printed samples.

2.4 Modeling and analysis of robotic and prosthetic fingers

Traditional robotic finger design typically uses simple hinges to connect digits which are typically actuated using separate motors located in the gauntlet, in an enclosure that surrounds the lower arm, or in the palm of the hand. Each of these motors is connected to the digit it controls through a separate set of cables (tendons) that move in respective channels, Figure 6.1. Gears are also sometimes used to connect the hinges with the motors. These designs are typically complex and require sophisticated control algorithms. Additionally, such configurations are bulky even when miniature motors are used.

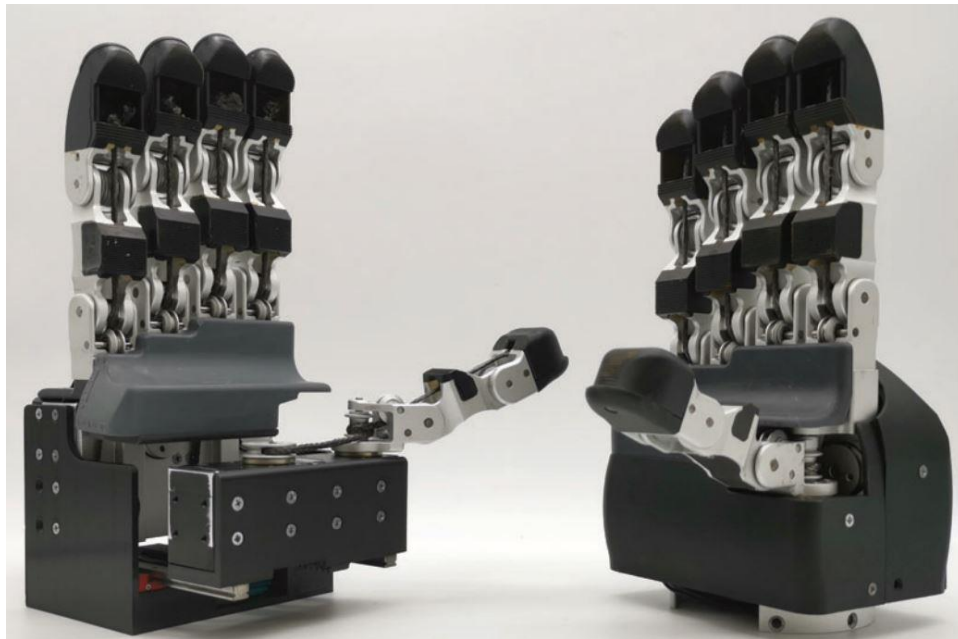


Figure 2.2: Example of a tendon-actuated robotic hand, [39]

An alternative to these designs is an underactuated finger where a single tendon goes through all the finger digits, Figure 6.2(a). When the tendon is subjected to a tensile load the

finger bends in a predetermined manner. While such a design lacks the versatility of multiple motors, it is relatively simple and can achieve the kinematic and gripping goals of the prosthetic hand. Recently, advances in 3D printing of thermoplastic polyurethane (TPU) resulted in innovative designs where simple hinges are replaced by 3D printed TPU beam joints. Each of these beams are fitted into two opposite recesses on two digits thereby connecting them, Figure 6.2(b). The TPU beam fulfills two objectives simultaneously: connecting the digits and providing spring action that would return the finger to its original configuration once the tendon tension is removed. These two areas, tendon-actuated underactuated fingers and TPU hinges, have received relatively limited attention and are not fully understood yet. In the following, we present a brief survey of research in these two topics.

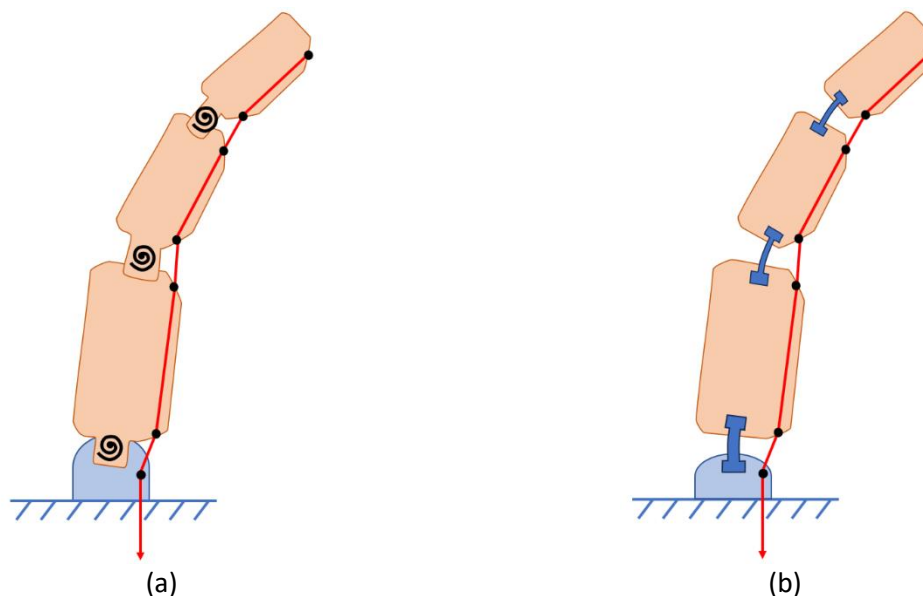


Figure 2.3: Underactuated prosthetic finger designs; a) a hinged finger with a single actuation tendon; b) flexible beam joints with a single actuation tendon

Some researchers proposed various models to relate tension of tendons to flexion of fingers and grasping forces. For example, a model for the kinematic behavior of a 3D printed, tendon-driven robotic hand was derived, [40]. The deflection of the digits was modeled and qualitatively compared to experimental results. This model did not relate tension in tendons and joint angles. The dynamic behavior of a tendon-actuated prosthetic finger while contacting and grasping a simple object was modeled, [41]. It was found that an appropriate reaction force was necessary to achieve a certain level of control of the finger while grasping. Likewise, the ability to perform a quality grasp depends on the size of the grasped object. No experiments were presented. This model used torsional springs at the joints as potential energy components rather than flexible beams. The joint design of a prosthetic finger was proposed using elastic ligaments to store energy during deflection from tendon actuation, [42]. The minimum tendon force required for static joint deflection was derived, and experiments were conducted to test joint durability and grasp capabilities. Tendon force calculations were not confirmed through experimentation, and a relationship between finger deflection and tendon force was not proposed. A kinematic model of a tendon-actuated robotic hand with torsional springs at the joints was proposed, [43]. The proposed model was simulated, and the workspace of the fingers was described. No experiments were conducted to validate the model. A relationship between the finger tendon tension and finger deflection was not derived.

The deflection of a 3D printed, tendon-actuated prosthetic finger was studied with both tendon extension and tendon force as an independent input as well as for an unobstructed and an obstructed grasp, [44]. Equations for the joint angles at static equilibrium were derived. This work does not consider the nonlinear behavior of the elastomer joints, which would experience

stiffening or softening under large strains. A molded polymer finger actuated by two tendons was presented to relate the parameters that affect the workspace and abduction/adduction angles of $\pm 45^\circ$, [45,46]. This model, which did not consider the nonlinearity of the urethane elastomer joints, resulted in approximately 35% error in terms of the force needed to achieve full flexion. A fully 3D printed tendon-actuated robotic finger with flexible beam joints was studied and compared to a human finger, [47]. It was found that varying the dimensions of the beam joints affect the digits trajectories and consequentially the joint angles. This work did not consider the effects of printing parameters on the behavior of the flexible joints, nor the typical nonlinear behavior of a highly material, LB-313J. Similarly, the authors do not derive a relationship between the load on the tendon and the deflection of the finger digits. The kinematic and dynamic behavior of a 3D printed, tendon-actuated prosthetic hand was modeled using the Lagrangian Method, [48]. Similar flexion when the finger was unobstructed and digit deflection when an object was grasped was achieved. However, a quantitative comparison was not provided.

This work investigated the flexion of the Flexy-Hand 2 prosthetic hand, which combines TPU flexible joints and tendon-actuation. This prosthetic hand design has not received sufficient attention relative to understanding the relationship between tendon tension and finger flexion. Our quasi-static model, which incorporated the nonlinear behavior of the joints, was derived using the principle of virtual work to account for the nonlinear behavior of the TPU beam joints. Experimental setup was developed to validate the proposed model.

2.3 Scope of work

First, a series of uniaxial tensile tests was conducted to study the mechanical behavior of two common print geometries found in most printed objects: infill geometry and wall geometry. Similarly, sets of the two regions were printed at 225 °C, 235 °C and 250 °C. This allowed the creation of a 3D printing parameters material model that was based on experimental data. Force-time data and image processing were used to create stress-strain curves for each specimen. We hypothesized that the infill material will be softer than the wall material. Similar to composites, the printed material that lies parallel to the loading direction should increase the strength of an object in that direction. Infill region specimens are printed, by default, with lines at $\pm 45^\circ$ from the loading direction, while wall region specimens are printed with lines parallel to the loading direction. We also hypothesized that increasing the extrusion temperature will increase the strength and stiffness of both regions, as described by modulus elasticity, stretch modulus, and stress at various strain values. Increasing the extrusion temperature of a printed specimen should allow for an increase in internal material adhesion as well as a reduction in the number of internal voids. The material models for both infill and wall materials were compared to results from earlier papers.

Next, a bending experiment was conducted using NinjaFlex in eighteen different dimensional configurations to create a comprehensive model of the bending characteristics of the material. The bending data was compared to modeling using the previously found material characteristics. The deflection from the experiments was recorded and analyzed with image processing. A closed form solution was derived to model the deflection of the bending specimens

based on Euler-Bernoulli beam theory, which we call Modified Euler-Bernoulli (MEB) method. A finite element analysis (FEA) model was also made to describe the specimen bending. The two modeling methods were compared to the experiment, and a mean non-dimensional difference value was calculated to compare the deflection-per-load of the three sets of data. We hypothesized that the MEB method would be just as accurate at predicting the deflection of the flexible beams as the FEA method, due to the inclusion of retraction and use of virtual work and strain energy.

Then, the results of the bending experiments and modeling were applied to the Flexy-Hand 2. A series of quasi-static bending experiments using a 3-digit prosthetic finger were conducted by applying weights to the tendon and recording the deflection. By applying the modeling to the 3-digit finger, its validity was confirmed. Three sets of joints will be bent in three trials each. The resultant deflection will be averaged and compared to ensure consistency. Lastly, FEA modeling was applied to the whole finger, and the results compared to the experiment. We hypothesized that substituting the flexible beams for torsional springs and hinged joints would be sufficient at modeling the behavior of the flexible beam joints. This is due to the consistent rotation seen in the experiments, and the elastic behavior exhibited by the flexible joints. We also hypothesized that the flexion of the 3-digit finger will accurately simulated due to the consistency of the TPU and flexible joint modeling.

Chapter 3: Influence of 3D printing parameters on the constitutive model of hyperelastic thermoplastic polyurethane

The infill and wall material of a 3D printed object behave differently. The printed material in the infill region commonly runs in $\pm 45^\circ$ alternating angles from the orthogonal x-y axis of the printer, while the material printed in the wall region is limited to the outer surface and edges of the object. The influence of wall thickness on the percent elongation at failure, tensile strength, Young's Modulus, and toughness of NinjaFlex[®] was studied [9]. Using tensile specimens, increasing the thickness of the wall region results in an increase in all these properties: 5% in percent elongation, 45% in tensile strength, 14% in Young's Modulus, and 50% in toughness. The number of wall lines, or the "shell thickness," was tested in flexion and uniaxial tension [49]. The results were generally consistent with [9], suggesting that mechanical properties of wall regions are higher than infill, as the properties increase with as wall thickness increased.

Similarly, parts printed at different extrusion temperatures have different mechanical properties as well, [49–53]. PLA tensile specimens were printed at four different extrusion temperatures, [50]. The average Young's Modulus, yield strength, and tensile strength increased with the temperature, plateauing as the temperature reached peak values. Two different grades of PLA filaments, PLA 4032D[®] and PLA 2003D[®], were printed with and without the clay nanocomposite C30B[®] at three different temperatures [51]. The extrusion temperature had a clear correlation with the elastic modulus of all tested materials, with PLA 2003D[®] and PLA4023D+C30B[®] having a negative correlation to temperature, and PLA 2003D+C30B[®] and PLA4023D[®] having a positive correlation to temperature. Polyether Ether Ketone (PEEK) dog bone

tensile specimens were printed at seven different temperatures and the mechanical properties were considered [52]. It was found that the tensile strength and the elastic modulus increased as the extrusion temperature increased. However, both of which leveled off at higher temperatures similar to previous PLA results.

In this chapter, material characterization experiments were conducted to understand the difference between infill and wall regions printed at different extrusion temperatures. By understanding how the printing parameters affect the 3D printed NinjaFlex® constitutive model, the prosthetic finger joints can be more accurately modeled. Due to alternating angles of material in the infill region, we hypothesize that the infill material will be softer than the wall material. We also hypothesize that increasing the extrusion temperature will increase the mechanical properties of the specimens, such as elastic modulus and stresses at corresponding strains.

3.1 Experimentation

3.1.1 Materials and preparation

Specimens were prepared using Cura LulzBot Edition [53]. NinjaFlex® tensile specimens were initially developed based on ASTM D638-14 standards [54] as shown in Fig. 3.1(a). However, using dog bone specimens resulted in a number of discontinuities due to the transition between the two cross sectional areas as shown in Figure 3.1(a). Therefore, the flared ends were removed, and

long, rectangular specimens were used, Figure 3.1(b), (c), and (d) show the infill and wall-only specimens. The test matrix is presented in Table 3.1.

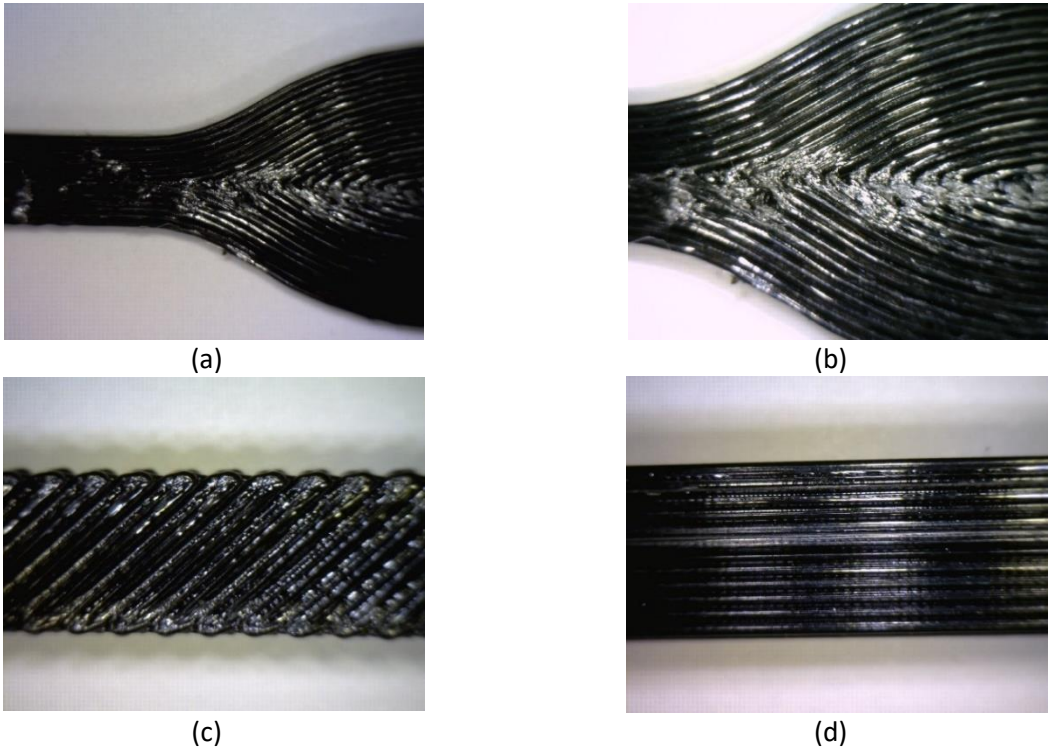


Figure 3.1: 3D printed tensile specimens; a) a dog bone specimen; b) zoomed-in view showing discontinuities; c) infill only specimen; d) wall-only specimens.

Table 3.1: Test matrix

Material Deposition Method	Extrusion Temperature (°C)
Infill	225
	235
	250
Wall Only	225
	235
	250

Ten tensile specimens of each group were printed, resulting in a total of 60 experimental specimens. All specimens were then printed on a Lulzbot® Taz Mini 2 [55] with an Aerostruder® tool head (3D printer, Fargo Additive Manufacturing Equipment 3D, LLC, Fargo, North Dakota, United States), Figure 3.2. Batches of five infill and five wall region specimens were printed on the build plate at a time.

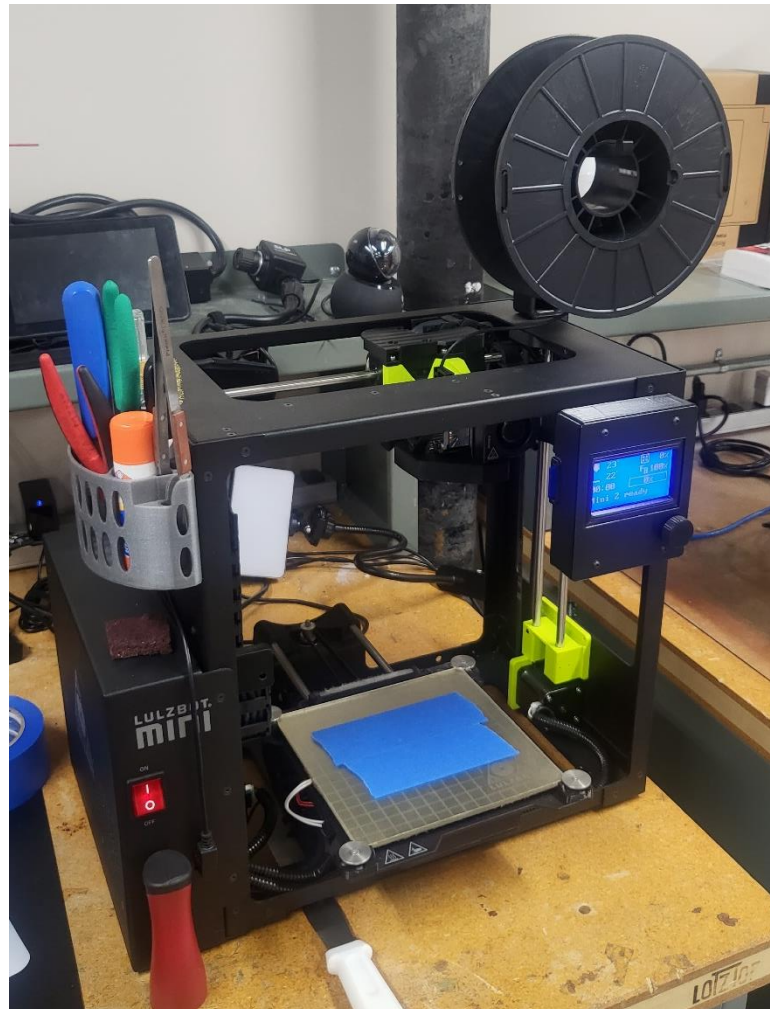


Figure 3.2: Lulzbot® Taz Mini 2

3.1.2 Experimental setup

The 3D printed specimens were tested on a custom-built low-force uniaxial tensile testing machine, Figure 3.2(a). The testing machine used a stepper motor in conjunction with a ball-screw and linear rail system to apply a specified displacement per unit time. A 25 lbf (111 N) load cell (Interface® SML-25, Scottsdale, AZ, USA) measured the tensile reaction force at a rate of 30 samples per second using a National Instrument Data Acquisition System (DAQ) with LabView (Austin, TX, USA). The extensions of the specimens were recorded with a Back-Bone Modified GoPro Hero 10® camera (San Mateo, CA, USA) and with a Nikon AF-S Nikkor® 18–140 mm Lens (Tokyo, Japan) at a rate of 30 frames per second. The camera was located on the other end of the optical table, 1.5 meters to the right of the tested specimens, not shown in Figure 3.3(a). The videos were recorded at 5.3 k resolution or 15.8 MP for each frame. After testing multiple background colors, a pink backdrop covered the area behind the specimens to best reduce optical noise, Figure 3.3(b).

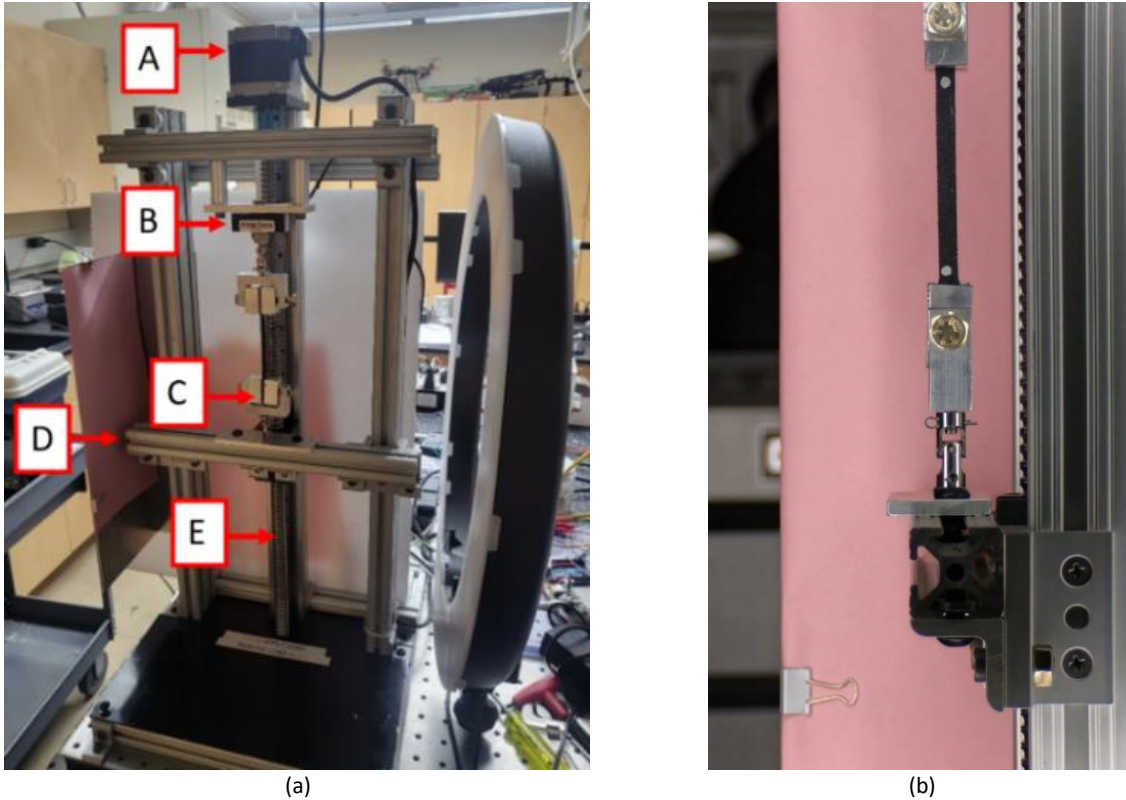


Figure 3.3: Tensile testing experiment; a) low-force uniaxial tensile testing machine, (A) actuating DC motor, (B) load cell, (C) specimen in grips, (D) linear rail system, (E) ball screw; b) specimen while being loaded.

The following summarizes the testing procedure. After the tensile specimens were placed in the grips, circular paint markers approximately 3.5 mm in diameter were added to both ends of the face of the specimen, approximately 5 millimeters in from the grips, Figure 3.3(b). Next, grips with the installed specimen were placed in the tensile machine. The experiment was conducted at a displacement rate of 0.2 mm/s.

The dimensions of the tensile specimen can be found in Table 3.2. These dimensions were based on several factors:

- 1) ASTM638-14 states that the minimum width of a tensile specimen is 6 mm.

- 2) The capacity of the loading range of the load cell used in the tensile testing machine is 0-111N.
- 3) It is desirable to capture the behavior of the printed specimen under large deformation. Earlier research on NinjaFlex® had a wide range of maximum strain, ranging from 0.1-12 engineering strain [8,9,56].

Based on the ultimate strength suggested by the manufacturer [57] and the thickness limitations of ASTM638-14, the thickness was assigned a value of 3 mm. The goal of an engineering strain of 2, which is equivalent to a 1.1 true strain, was based on the range of the camera lens, the placement of the camera, and load cell limitations.

Table 3.2: Tensile specimen dimensions

Width, w , (mm)	Thickness, t , (mm)	Total Length, l_t , (mm)	Free Length, l_f , (mm)
6	3	115	50

3.1.3 Data processing

Frames were extracted from the experimental videos and cropped based on the first and last images of the experiment, Figure 3.3. The images were converted to grayscale and then binarized with respect to the two markers using a custom Matlab® code (Natick, MA, USA). The two markers were identified in each image, and their coordinates of the innermost points were recorded. The distance between the inner edges of the markers of the post-trimmed data set was identified as

the initial gage length of the specimen, L_0 , as shown in Figure 3.3(a). The current length of the specimen, L_n , was measured between the inner edges of the markers while the specimen was loaded, as shown in Figure 3.3(b).

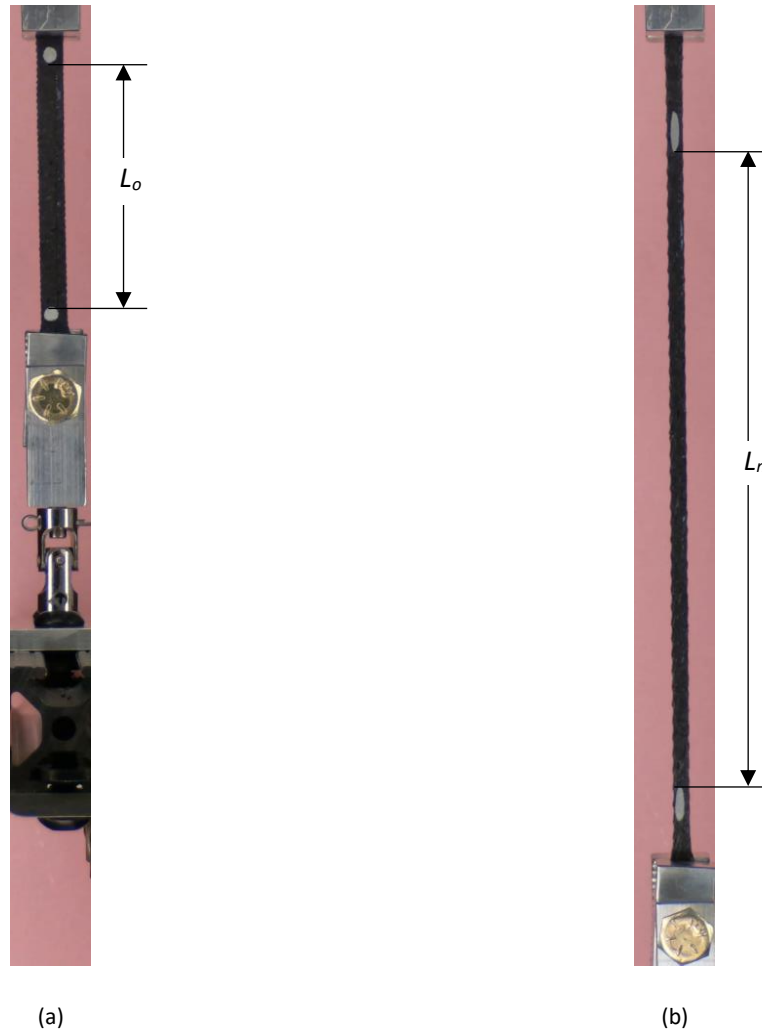


Figure 3.4: Typical phases of the tensile testing experiment; a) infill specimen initial image; b) infill specimen final image.

Load cell data was trimmed to synchronize with the actual testing. A custom Matlab® code (Natick, MA, USA) was used to calculate the stress and strain using the respective dimensions of each test specimen.

3.2 Constitutive model

Earlier researchers have presented possible constitutive models for TPUs. For example, it was found that a 2nd or 3rd Order Ogden constitutive models were accurate for strains from 550-1200% [9,56]. Neither the effect of the material deposition regions nor the influence of extrusion temperature was considered. This work considers the Mooney-Rivlin constitutive model, since it was considered suitable for polymers undergoing strains up to 200% [58]. The governing equations of the Mooney-Rivlin model are summarized in Appendix A.

3.3 Results

3.1 Experimental results

The measured dimensions of the printed specimens of each group can be found in Table 3.3. The engineering stress and strain were calculated using each specimen's dimensions. These data were then converted into their equivalent true stress and strain. The average and standard deviation of true stress were then calculated for each group. **Error! Reference source not found.** shows the resulting true stress-strain curves.

Table 3.1: Measured dimensions of printed specimens (ten tensile specimens for each group)

Print Region	Extr. Temp. (°C)	Width, w, (Std. Dev.) (mm)	Thickness, t, (Std. Dev.) (mm)	Mass, m, (Std. Dev.) (g)
Nominal		6.0	3.0	2.5*
	225	5.8 (0.10)	3.0 (0.06)	1.7 (0.04)
Infill	235	5.8 (0.04)	3.0 (0.02)	2.0 (0.01)
	250	5.9 (0.02)	3.0 (0.13)	2.1 (0.02)
	225	5.9 (0.05)	2.9 (0.04)	1.8 (0.07)
Wall	235	5.9 (0.02)	3.1 (0.02)	2.2 (0.02)
	250	6.1 (0.17)	3.0 (0.13)	2.2 (0.02)

* Mass calculated from nominal volume and manufacturer reported density of 1.19 g/cc [57] and assumes no voids.

Since the specimens did not experience the same maximum strain, the stress response of all specimen groups was compared at 0.9 strain, Table 3.4. The elastic modulus for all groups was also calculated using the corresponding engineering stress-strain curves based on the linear portions. This differed for each specimen group, ranging from 0.04 to 0.06 strain.

Table 3.2: Mechanical properties of specimen groups

Print Region	Extr. Temp. (°C)	Elastic Modulus (MPa)	Stress at 0.9 Strain (MPa)
	225	8.14	7.69
Infill	235	15.84	10.61
	250	17.63	10.99
	225	15.36	9.59
Wall	235	18.73	11.25
	250	19.48	11.62

While elastic modulus may not be the most appropriate measure for hyperelastic materials, it is presented here due to its usage in other studies that previously investigated the stress-strain response of NinjaFlex® and similar TPUs. Additionally, the manufacturer stated that

NinjaFlex® has an elastic modulus of 12 MPa, [57]. The print temperature and other key printing parameters like wall thickness were not specified, so it is not clear as to the cause of the higher elastic modulus in comparison to our experimental results. The elastic modulus of specimens similar to our infill and wall region printed between 230-240 °C was reported by [8]. Their infill comparable specimens were reported to have an elastic modulus of 7.768 MPa, and their wall comparable specimens were reported to have an elastic modulus of 8.505 MPa. These values are significantly lower than our experimental results for specimens printed at 235 °C. The authors of [8] reported using multiple printers and printing the NinjaFlex® specimens, which could all contribute to the different elastic modulus values.

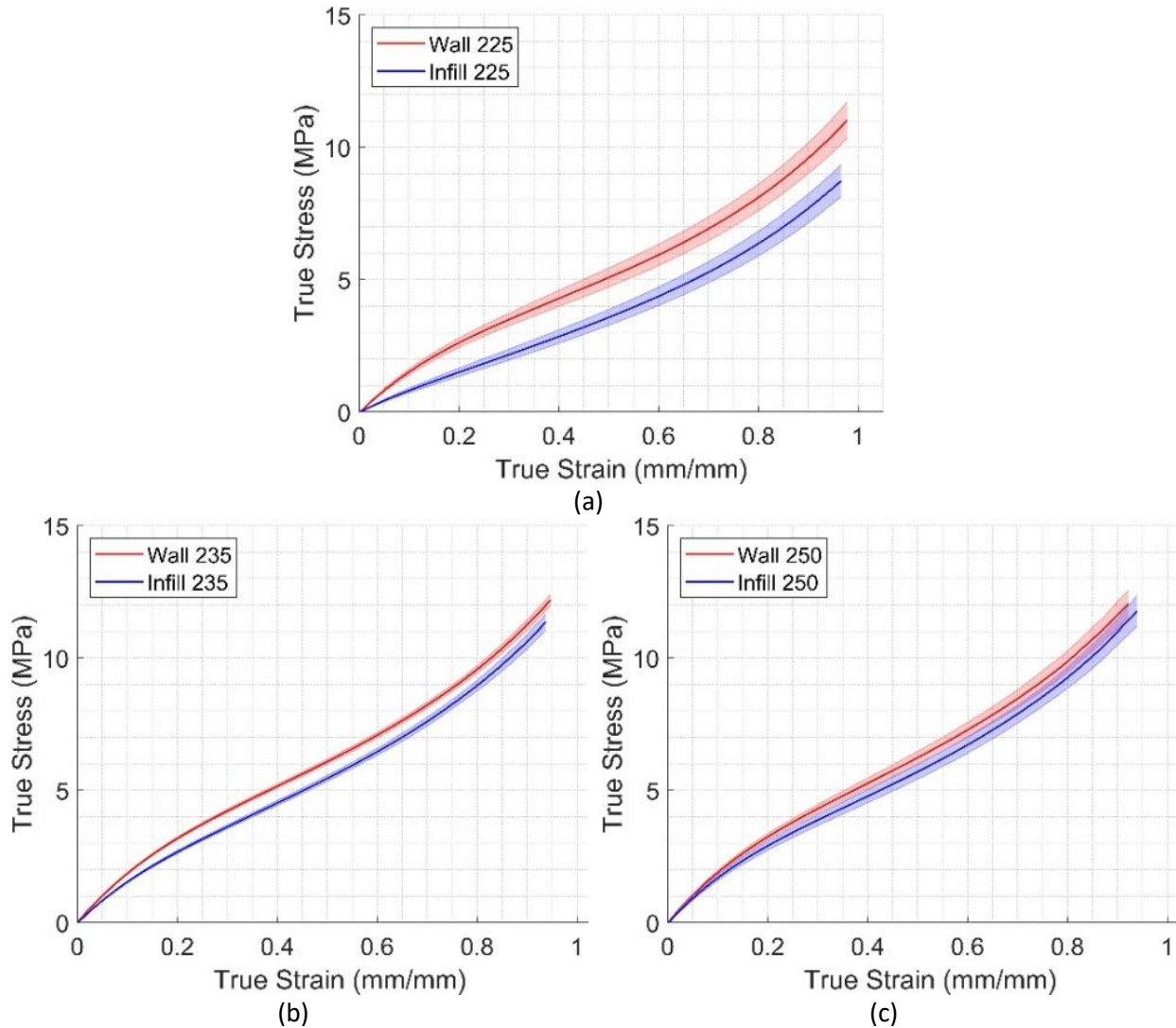


Figure 3.5: Average and standard deviation experimental results of wall and infill region specimens at different extrusion temperatures; a) 225°C; b) 235°C; c) 250°C. The thick lines are the average values while the shaded regions represent the standard deviations

Due to the nonlinear behavior of TPUs and the narrow linear portion of the stress-strain curves, it would be appropriate to use the stretch modulus to describe the nonlinear elastic response of an isotropic hyperelastic material under uniaxial loading [59,60]. Stretch modulus can be defined as:

$$S = \frac{\sigma}{\ln(\lambda)} \quad (3.1)$$

where λ is the principal stretch ratio ($1 + \epsilon$) and σ is the corresponding Cauchy principal stress. Based on the average stresses and strains of Figure 3.5, the stretch modulus of each group was calculated, Figure 3.5.

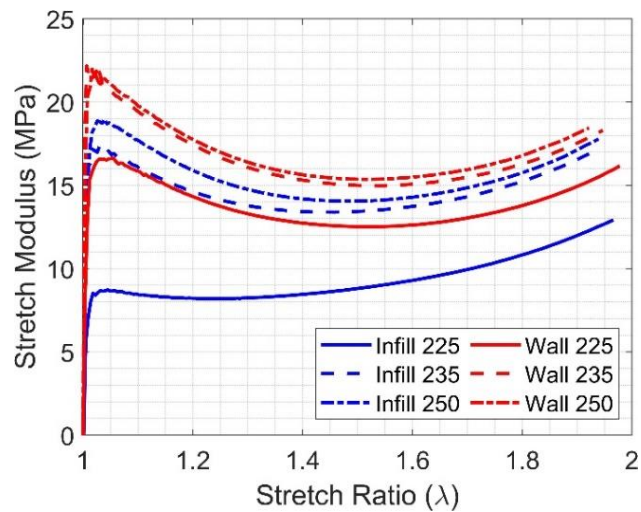


Figure 3.6: Stretch modulus of all specimen groups

3.2 Constitutive model results

Using the material calibration software, MCalibration® (Dover, Massachusetts, USA), the experimental data were fitted into the constitutive model. For all models, a global optimal search was used to fit to the experimental data. The best values for the coefficients, C_{10} , C_{01} , and C_{11} of the 3rd Order Mooney Rivlin constitutive model, Appendix A, were identified for each of the six

experimental groups. The coefficients were determined with the goal of minimizing the normalized mean absolute difference (NMAD) fitness value:

$$NMAD = \frac{\sum_{i=1}^n \left(\frac{\frac{\sum_{j=1}^m |e_{i,j} - p_{i,j}|}{m}}{\max\left(\frac{\sum_{j=1}^m |e_{i,j}|}{m}, \frac{\sum_{j=1}^m |p_{i,j}|}{m}\right)} \right)}{n} \quad (3.2)$$

where e is the vector of experimental stress data for one trial, p is the corresponding vector of the predicted model, m is the number of points on the stress-strain curve, and n is the number of specimens. The fitness values for multiple experiments are averaged to produce the overall NMAD value. A representative result for wall regions printed at 225°C is shown in Figure 3.7. The resulting coefficients and NMAD values for each specimen group are found in Table 3.3.

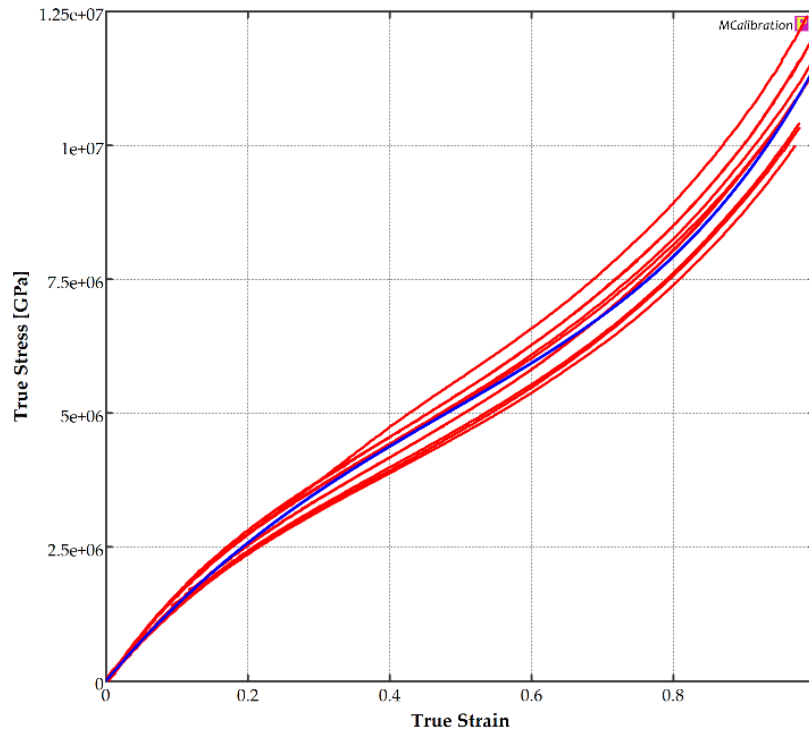


Figure 3.7. Sample MCalibration® material curve fitting of wall region specimens printed at 225°C

Table 3.3: Fitted model coefficients and fitness results

Print Region	Extr. Temp. (°C)	C_{10} (Pa)	C_{01} (Pa)	C_{11} (Pa)	NMAD (%)
Infill	225	-2.04e5	1.64e6	6.30e4	5.97
	235	-1.40e6	4.05e6	1.95e5	1.98
	250	-1.68e6	4.56e6	2.21e5	3.18
Wall	225	-1.55e6	4.21e6	1.90e5	4.96
	235	-1.93e6	5.12e6	2.34e5	1.76
	250	-2.33e6	5.70e6	2.93e5	3.30

3.3. Finite element validation

To assess the validity of the constitutive models, FEA models were developed for each group using ANSYS® (Canonsburg, PA, USA). Planar geometry was chosen using the nominal dimensions of the tensile specimens, Table, with the thickness, t , being defined in the ANSYS® Mechanical. A mesh stability study was conducted on the models to ensure a stable solution. A mesh with an average element side length of 0.25 mm was adequate when compared to 0.1 mm and 0.5 mm element sizes. This mesh resulted in 4,800 elements, Figure 3.8.

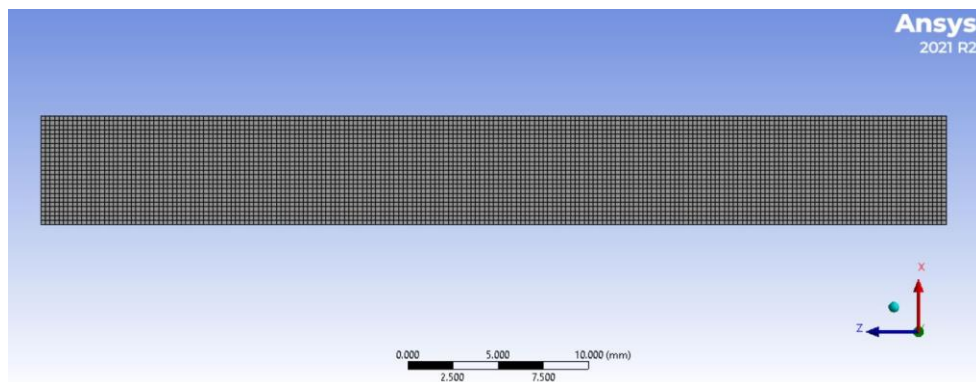


Figure 3.8: 0.25 mm mesh of tensile validation models

A fixed boundary condition was applied to the left edge of the model. A ramped tensile load was applied to the right edge of the model. The maximum loads corresponded to the average maximum load experienced by each experimental group, Table 3.4.

Table 3.4: Maximum tensile load for model validation

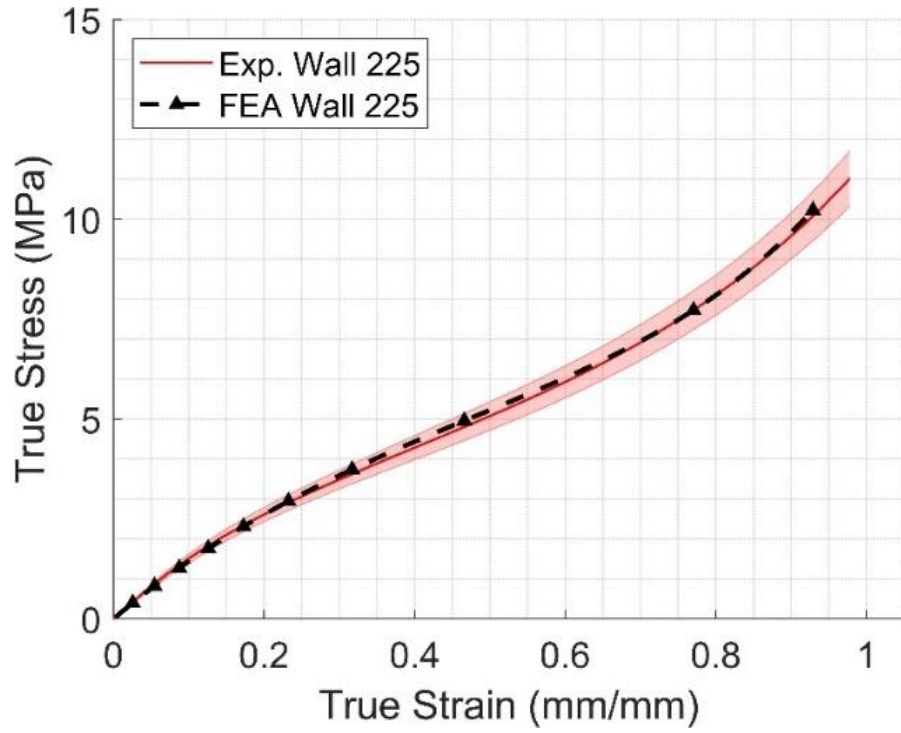
Print Region	Extrusion Temperature (°C)	Average Maximum Load (N)
Wall	225	72.7
	235	86.2
	250	88.2
Infill	225	58.7
	235	78.2
	250	80.8

Typical results of the FEA model overlapping with the experimental results are shown in Fig. 9, which are the lowest model error in Figure 3.9(a) and the highest model error in Figure 3.9(b). The black dashed line represents the stress-strain behavior of the model. All specimen groups fall between these two results in terms of model error. To compare the model to the experimental results, an error function was defined, Eqn. 3.3, which compares the stress of the experiment and model for a given strain value.

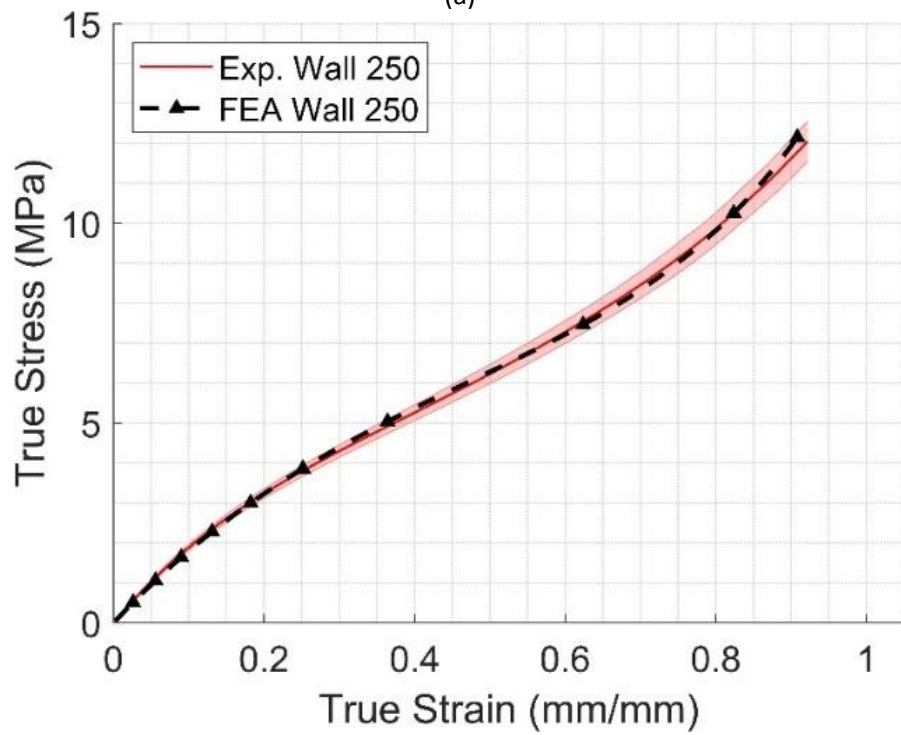
$$E = \frac{\sum_{i=1}^n \frac{|\sigma_{mi} - \sigma_{exp.i}|}{\sigma_{exp.i}}}{n} \quad (3.3)$$

where n is the number of stress values, the subscript m represents the model, and $exp.$ represents the experiment. The errors for each group are found in

Table 3.5.



(a)



(b)

Figure 3.9: Sample of model validation results, model in black dotted line, experimental data in colored shaded lines

Table 3.5: Model error values for each specimen group

Print Region	Extrusion Temperature (°C)	E (%)
Wall	225	3.02
	235	3.45
	250	5.18
Infill	225	4.53
	235	4.99
	250	3.46

3.4 Discussion

It is apparent from the experimental stress-strain results, Figure 3.5, that the filament deposition and extrusion temperatures have significant influence on NinjaFlex's® mechanical behavior. As the extrusion temperature increases, the difference between the stress-strain curves of infill and wall groups decreases, suggesting that an object printed at 250°C will behave more homogeneously. Interestingly, specimens printed at 235 °C resulted in the lowest standard deviation of the extrusion temperatures. This is likely due to the higher consistency of the specimen dimensions, Table 3.3.

The elastic modulus, despite representing only a small portion of the strain range, also shows the same increase in magnitude as the stress strain curves, Table 3.4. The stress at 0.9 strain increased with the extrusion temperature for all groups.

Lastly, the stretch modulus describes a wider range of behavior that also increased as temperature increased, Figure 3.6. For all these properties, the difference between values of infill and wall specimen groups also decreased as temperature increased. Overall, the wall region specimens had consistently higher elastic modulus, stretch modulus, and stress at 0.9 strain. This is likely due to the orientation of TPU filament as wall specimens have filament that runs the length of the specimens, while infill specimens have material lines that sit at $\pm 45^\circ$.

Material lines that are along the direction of loading have stronger tensile properties, similar to fibers in composite materials; elastic modulus, for example, corresponding to different fiber orientations is higher in the normal principal directions, [61]. The groups also show an increase in quantity of material printed with an increase in temperature, Table 3.3, with wall region specimens consistently showing greater mass than infill material. The increase in masses contributes to each group resisting more stress. Similarly, the increase in mass suggests better material adhesion due to fewer voids within the specimens, also noted in [62]. Our hypothesis of infill specimens being “softer” than the wall specimens was proved correct, as well as increasing the extrusion temperature increasing mechanical properties, like modulus of elasticity and stretch modulus.

It should be noted that infill specimens printed at 225°C were consistently lower than all other groups in terms of stress-strain behavior, elastic modulus, stress at 0.9 strain, and stretch modulus. Additionally, this group had two phases of the stress strain curves, while all others had three. The linear elastic portion of the stress strain curves continued for more strain than any

other group. This behavior is likely due to poor material adhesion between layers and print lines and voids as is shown in Figure 3.1(b).

The constitutive model coefficients were found with a reasonable level of accuracy, with all specimen groups having an NMAD value of less than 6%, Table 3.3. Model coefficient values increased in magnitude as the extrusion temperature increased, following a similar trend to the elastic modulus. This suggests that the 3rd Order Mooney-Rivlin constitutive model is consistent and sufficient in modeling this TPU at the given temperatures.

Lastly, the model validation was able to replicate the experimental results with sufficient accuracy. The stress-strain behavior of each specimen group was replicated with approximately 5% error or less. This shows that the models can sufficiently predict the behavior of wall and infill deposition at the used extrusion temperatures.

This work has some limitations. Firstly, the only material tested was NinjaFlex[®]. While this is a widely available material, every TPU will have different material properties. As discussed in Chapter 2, Section 2.2, the characteristics of a printed material are affected by all printing parameters, as well as the printer used. A comprehensive study should include these effects. Lastly, the upper engineering strain limit for Mooney-Rivlin constitutive model is approximately 2 [58]. It is of interest to assess the validity of this model beyond this range.

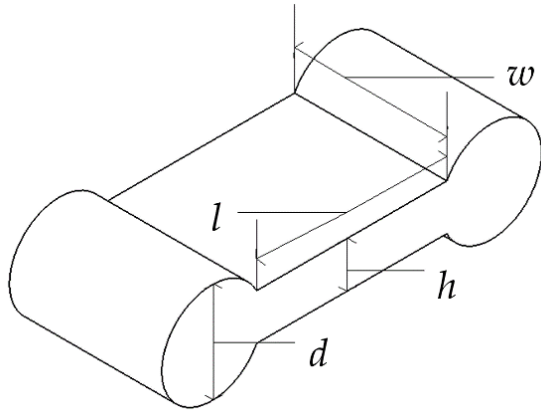
Chapter 4: Characterizing the behavior of 3D printed hyperelastic thermoplastic polyurethane hand prosthetic joints

In this chapter, the bending behavior of the hyperelastic thermoplastic polyurethane filament, NinjaFlex® is studied. A variety of specimen configurations were subjected to quasi-static loads similar to what would be induced by tendon tension to understand how the performance of NinjaFlex® 3D printed joints.

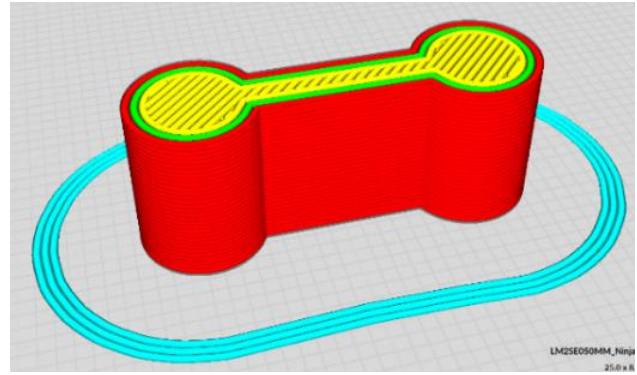
4.1 Specimen preparation

The manufacturer of NinjaFlex® has provided several key mechanical properties that were found following ASTM D638 standards, [63] Table 2.1. However, other researchers have provided different values for these characteristics. This variation may be due to the 3D printer used as well as the printing parameters. Additionally, some researchers have provided different stress–strain curves for NinjaFlex®, [7–10,56].

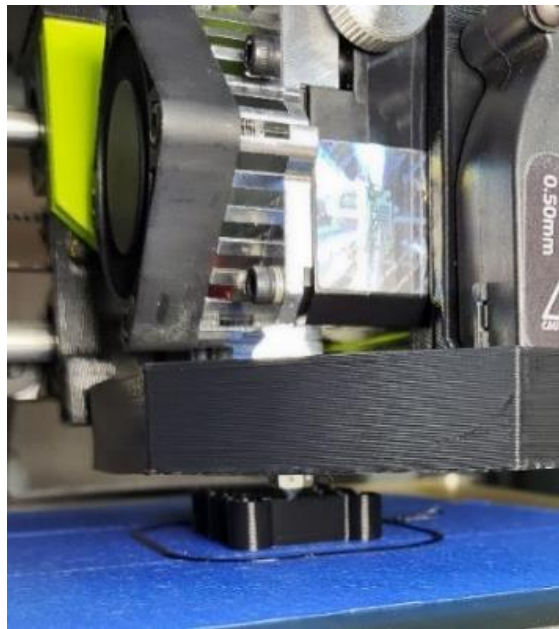
In this research, experiments were conducted using 3D printed NinjaFlex® dog-bone specimens with varying rectangular cross sections, Figure 4.1(a). The length (l), width (w), and height (h) were varied to create eighteen unique specimens, Table 4.1. The diameters of the two cylindrical ends, d , depended upon the height of the specimen. Each of the eighteen specimens were printed three times for a total of fifty-four samples.



(a)



(b)



(c)

Figure 4.1: specimen preparation: (a) variables of the specimens; (b) specimen representation in the Cura LulzBot® edition software (infill: yellow, walls: green and red); (c) printing a specimen using the LulzBot Taz Mini 2®

Table 4.1: Specimen dimensions

Specimen ID	l (mm)	h (mm)	w (mm)	d (mm)	Number of Wall Lines
1			8	3.85	2
2	10.0	1.8	10	3.85	2
3			12	3.85	2
4			8	3.85	2
5	15.0	1.8	10	3.85	2
6			12	3.85	2
7			8	5.70	3
8	10.0	2.7	10	5.70	3
9			12	5.70	3
10			8	5.70	3
11	15.0	2.7	10	5.70	3
12			12	5.70	3
13			8	7.70	3
14	10.0	3.6	10	7.70	3
15			12	7.70	3
16			8	7.70	3
17	15.0	3.6	10	7.70	3
18			12	7.70	3

The CAD models of the specimens were converted to .stl files using the Cura Lulzbot® Edition (model slicing software, Fargo Additive Manufacturing Equipment 3D, LLC, Fargo, North Dakota, United States), [53], Figure 4.1(b). This software has a library of print parameters for numerous filament materials including NinjaFlex®. To represent typical 3D printing, the print quality was set to standard; print parameters are listed in Table 4.2. Using the default slicing settings, the number of wall lines for each specimen varied depending on the specimen height, h, as shown in Table 4.1. All specimens were printed on the same machine with the same black NinjaFlex® filament using a Lulzbot Taz Mini 2® with an Aerostruder® tool head (3D printer, Fargo Additive Manufacturing Equipment 3D, LLC, Fargo, North Dakota, United States), with an extruder diameter of 0.5 mm, [55]. A single layer of painters’ tape was used on the heated print plate for

print adhesion, Figure 4.1(c). If specific mechanical properties are desired, the analysis of Chapter 3 can be used to determine the appropriate non-standard printing parameters.

Table 4.2: 3D Printing parameters

Print Parameter	Value
Filament Diameter	1.75 mm
Infill Density	100%
Quality	Standard (0.32 mm layer height)
Nozzle Temperature	225 °C
Bed Temperature	60 °C
Print Speed	15 mm/s
Wall thickness	1 mm

4.2 Bracket preparation

To apply the proper boundary conditions to the two ends of the specimens, ABSplus P430 (3D printer filament, Stratasys, Ltd., Eden Prairie, Minnesota, United States) custom brackets were designed, Figure 4.2, and printed using a Stratasys® Fortus 250mc (3D printer, Stratasys, Ltd., Eden Prairie, Minnesota, United States), [64,65]. The left bracket, which was attached to a fixed base, allowed one end of the specimens to be completely fixed while the right bracket, which had a hole where weights were attached to a fishing line, bent the specimens as cantilevers. Three sets of brackets were created to tightly fit the three specimen diameters, d.

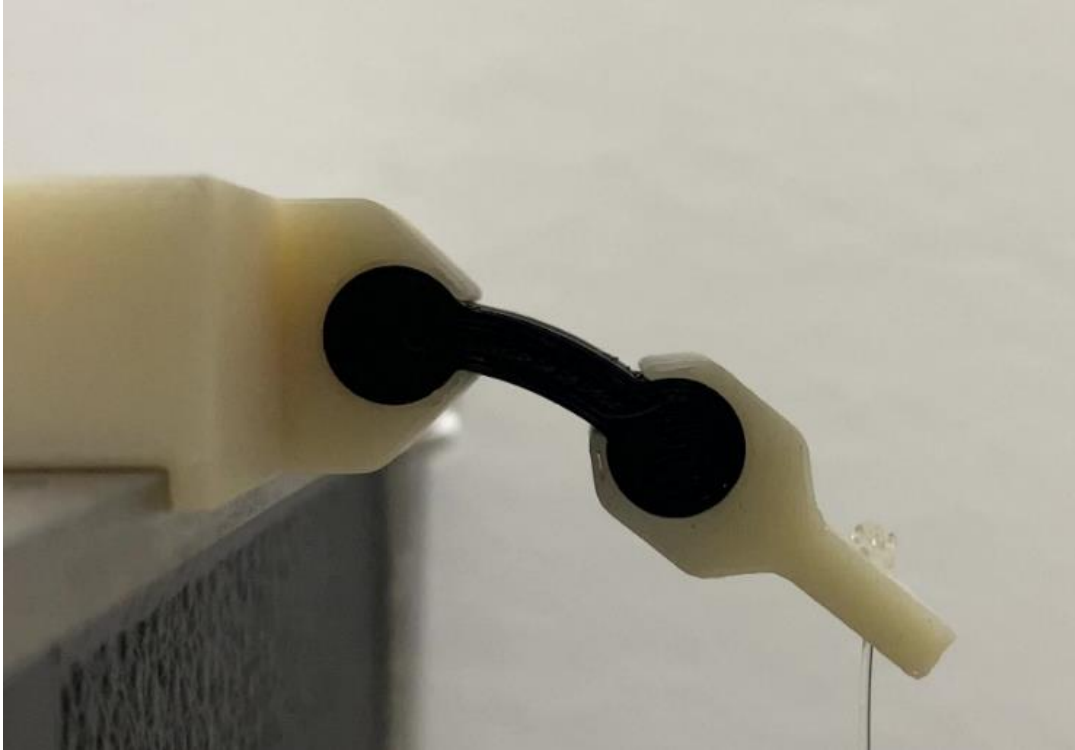


Figure 4.2: A loaded specimen between brackets

4.3 Experimental procedure

Loads were specimen-dependent and chosen to induce large bending in the specimens (Table 4.3). Stiffer specimens were, therefore, subjected to heavier loads. Loads were applied in a quasi-static manner by incrementally increasing weight attached to the right bracket, as shown in Table 4.3. The whole experiment was recorded using an iPhone 11 Pro® (cellphone, Apple Inc., Cupertino, California, United States) at 4k resolution at a rate of 60 frames per second.

Table 4.3: Loading parameters of the bending experiments

Specimen ID	Load Increment (g)	Maximum Applied Load (g)	Bracket Weight (g)	Center of Mass of the Right Bracket ¹ (mm)	Location of External Weights ¹ (mm)
1, 2, 3	5	50	3.88	9.3	17.86
4, 5, 6	5	25	3.88	9.3	17.86
7, 8, 9	10	70	3.70	9.5	17.21
10, 11, 12	10	60	3.70	9.5	17.21
13, 14, 15	20	120	3.41	10.4	16.87
16, 17, 18	20	100	3.41	10.4	16.87

¹ Distances were measured from the right end of the free length of the beam.

4.4 Image processing

For each specimen, frames corresponding to a steady-state configuration after the load was applied were extracted from the videos of the experiment; corresponding loads were recorded. A custom code utilizing the MATLAB® Image Processing Toolbox (software, The MathWorks, Natick, Massachusetts, United States) was written for processing the images to extract the location of the tip point deflection of the free length, l , [66]. First, all images were cropped to reduce unnecessary noise. Next, each image was binarized to isolate the specimen, Figure 4.3(a). The two cylindrical ends of a specimen were identified using morphological detection and removed to leave the middle section, Figure 4.3(b). The four edges of this section were determined using a border detection function, *bwboundaries*. To identify the neutral axis specimen's middle section, an equal number of equally spaced points were created on the top and bottom edges. For each corresponding point on these two curves, the midpoint was identified to be on the neutral axis, Figure 4.3(c). Second-order polynomials were fitted to the top and bottom edges and the neutral axis to reduce any noise associated with the averaging, Figure

4.3(d). The last point on the neutral axis of the rectangular section was identified by the intersection of the two cylindrical sections with the neutral axis curve, Figure 4.3(d). Finally, all relevant information was converted from pixels to millimeters based on camera parameters.

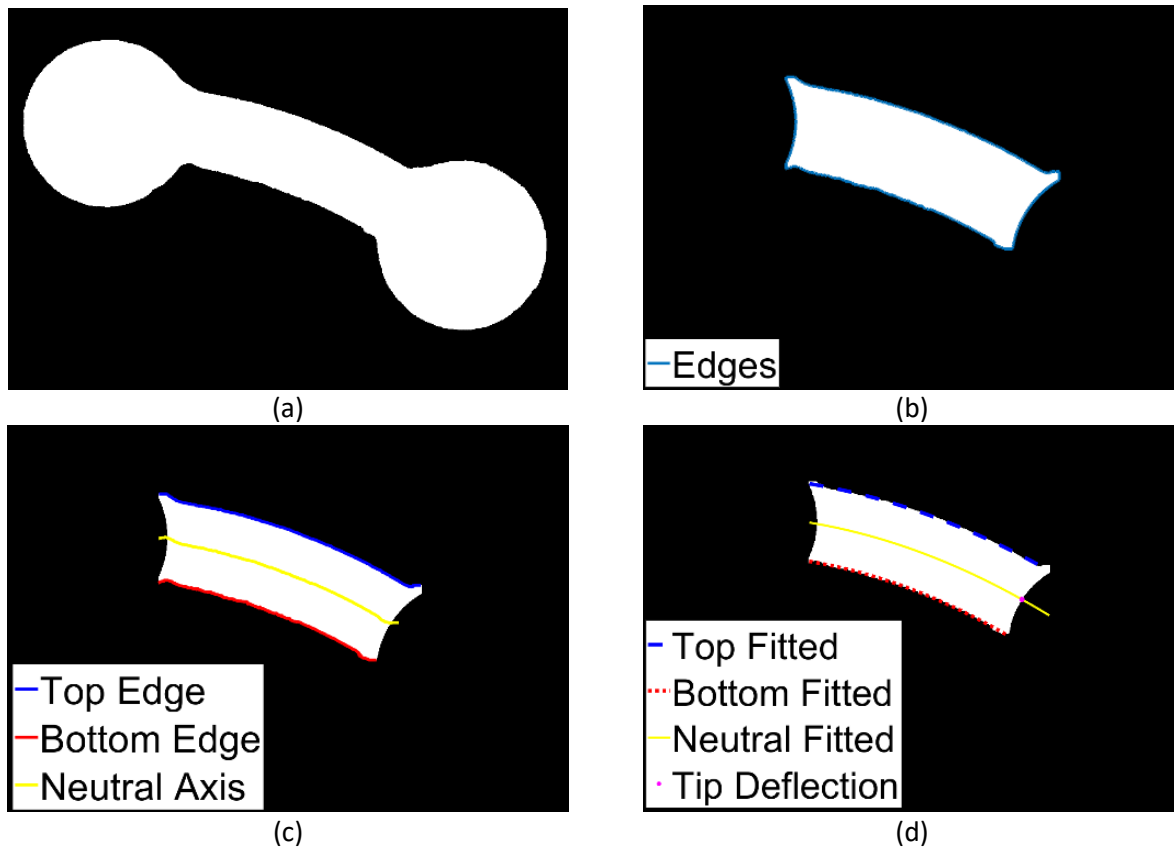


Figure 4.3: Specimen image processing: (a) images were cropped and binarized; (b) the cylindrical ends were identified and removed, and the edges of the middle portion were determined; (c) two sets of equally spaced points were created on the top (blue) and bottom (red) borders and averaged to determine the neutral axis (yellow); (d) the top and bottom edges and the neutral axis were fitted with 2nd order polynomials, and the intersection of the neutral axis and the right cylindrical section was used for the tip point deflection (pink).

4.5 Results

The experimental results for the three samples of each specimen were averaged, and their standard deviations were calculated in the y and x directions. To compare the relative motion when loaded, the first, unloaded state was used as a datum for the deflection of the beam joint. Figure 4.4 shows the x and y deflections of one of the stiffest and most flexible specimens, Specimen 15 and 1, respectively. The dimensions of the specimens are listed in Table 4.1. The loads were adjusted in the same manner as the motion, where the first load was set as the datum and the subsequent were adjusted accordingly. The adjusted load is denoted as “normalized” load.

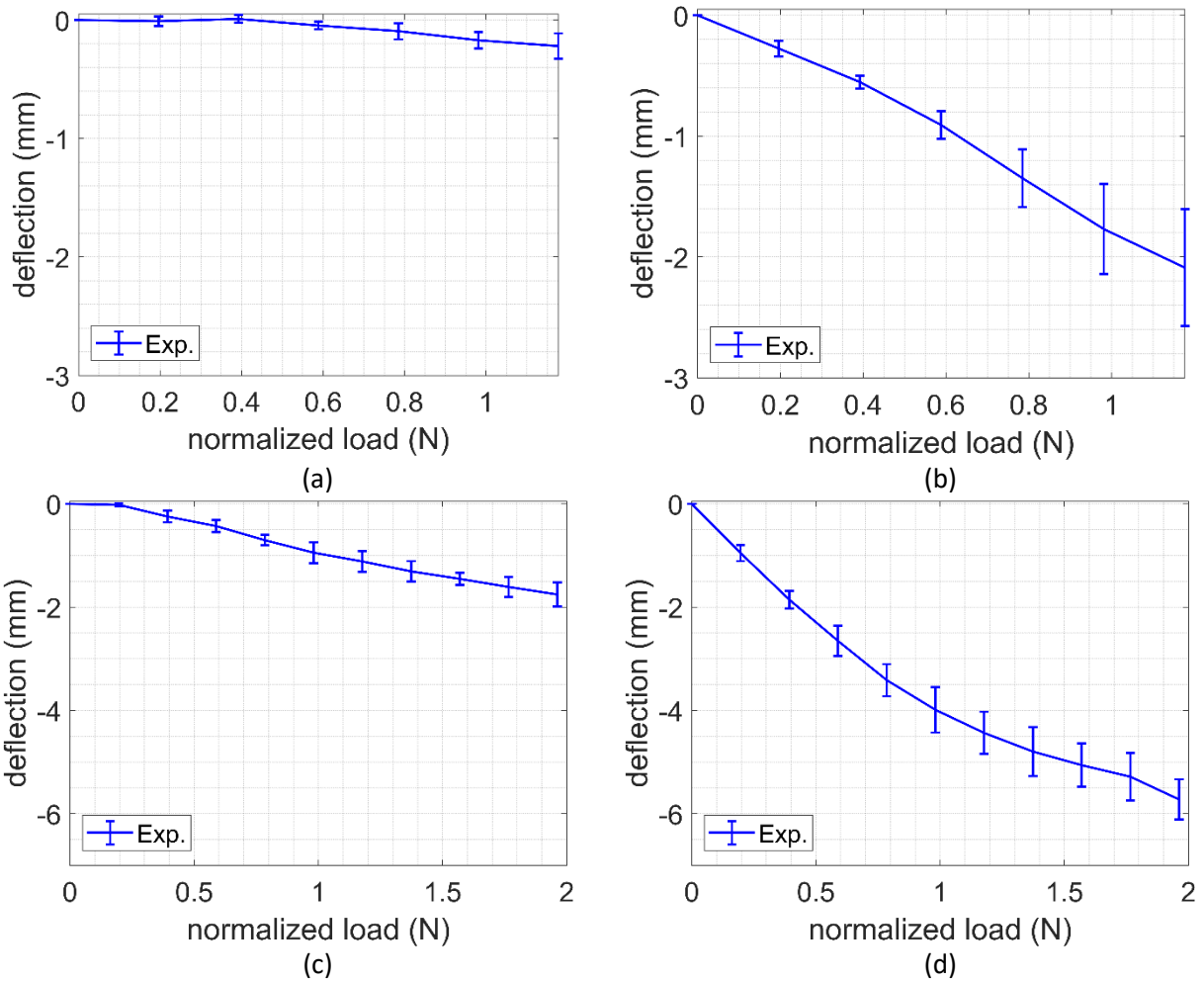


Figure 4.4: Experimental deflection in the x and y direction; (a) a relatively stiff Specimen 15 x deflection; (b) a relatively stiff Specimen 15 y deflection; (c) a relatively flexible Specimen 1 x deflection; (d) a relatively flexible Specimen 1 y deflection

In the case of Specimen 15, which was relatively stiff, the experimental tip deflection deviated slightly from moving along a smooth curve, most noticeably in the x-direction. On the other hand, the tip point of Specimen 1 moved along a smoother curvature. All other tested specimens followed these trends. For example, the tip points of Specimens 7–9 and 13–15, which were relatively stiff, did not follow a smooth curvature. This may be the combined result of small magnitudes of motion, the camera quality, and the inevitable blur. Additionally, it was observed

that the standard deviation increased as loading increased for all specimens, which may be the result of built-up issues with the experimental setup or variation in the 3D printer quality.

Chapter 5: Modeling the behavior of 3D printed hyperelastic thermoplastic polyurethane hand prosthetic joints

In this chapter, a novel method was presented to help understand the behavior of the 3D printed hyperelastic thermoplastic joints of the Flexy-Hand 2. This method is based on a modified form of Euler-Bernoulli beam theory, denoted here as the MEB method, to approximate the deflection and retraction of the joint tip under loading. The results were compared with the results of the experiment presented in Chapter 4 as well as finite element analysis (FEA) simulations.

5.1 Analytical modeling of flexible 3D printed prosthetic joints using a modified Euler–Bernoulli equations

Classical equations of material mechanics can be used to predict the component deformations under known loads. For example, traditional beam theory was used to model a multibody system composed of NinjaFlex[®] and rigid links of acrylonitrile butadiene styrene (ABS), [67]. Similarly, Euler–Bernoulli beam theory was used to model hyperelastic pneumatic actuators made of silicone, [33]. However, classical beam equations may not be able to accurately describe the deformation of parts such as those made of NinjaFlex[®] due to the hyperelastic material behavior and the large deflection these parts may experience.

We proposed modifying the Euler–Bernoulli beam theory to account for the retraction and deflection of the beam in the axial direction due to bending. As such, the component of the

normal load were a function of the load point's rotation and the load variation, Figure 5.1(a). This accounted for the forces and moments acting upon the experimental specimen as well as the load variation as the angle of deflection increased. Euler–Bernoulli beam equations were used as a basis, though through the comparison of the virtual work done on the system and the strain energy in the system, the deflections of the beams were derived. Therefore, the virtual work and virtual strain energy of the system were assumed to be equivalent.

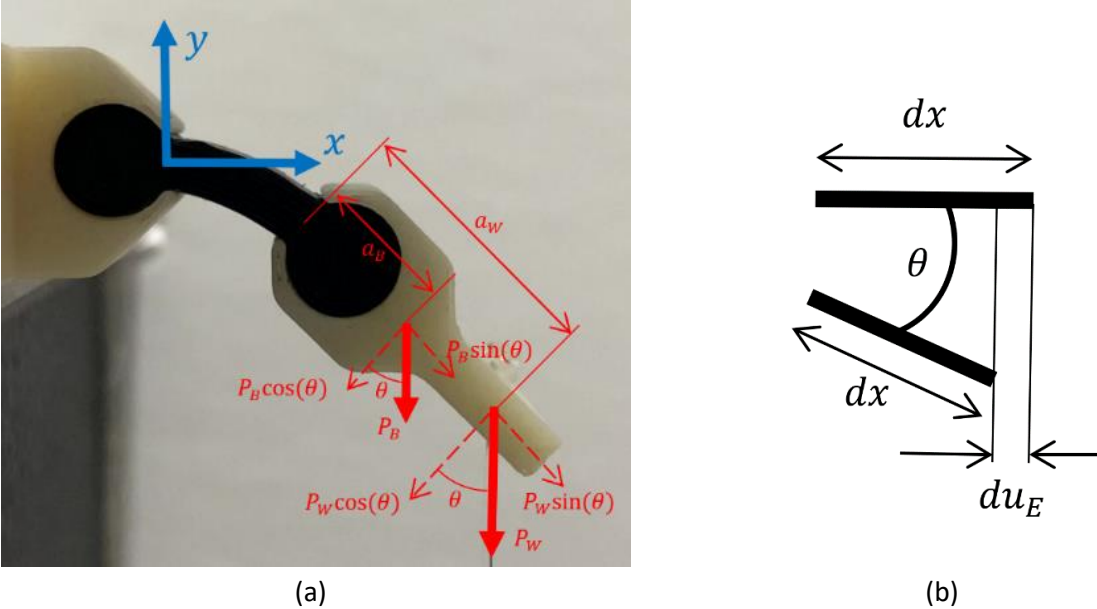


Figure 5.1: Specimen diagrams. (a) diagram of experimental system: P_W is the load applied, P_B is the load applied by the weight of the bracket. the lengths a_B and a_W represent the moment arms for each respective load. the angle θ is equivalent to $\tan^{-1}(v_x(l))$ at the tip of the beam. (b) retraction of a differential element on inextensible beam

Flexi hands joints were rectangular with two cylindrical ends. It was assumed that the cylindrical ends of the beam joints were fitted perfectly within all fixtures, causing no slippage during the experiment, Figure 5.1(a). The free-end bracket had a significantly higher stiffness than the specimen and was assumed to be rigid. Each beam joint deformed under a point load and was allowed to reach a state of static equilibrium, therefore, the variations in the virtual work done by the external loads and strain energies of the beam joint were equated to zero:

$$\delta W - \delta U_A - \delta U_B = 0 \quad (5.1)$$

where W is the virtual work, U_A is the axial strain energy, and U_B is the bending strain energy.

First, the work done on the system is defined as:

$$\begin{aligned} W = & (P_W + P_B) \sin(\theta(l)) u(l) + \\ & (P_W + P_B) \cos(\theta(l)) v(l) + \\ & (P_W a_W + P_B a_B) \cos(\theta(l)) \theta(l) \end{aligned} \quad (5.2)$$

where P_W is the load from the applied weight, P_B is the load from the bracket weight, θ is the angle between the plane cross-section and the vertical axis, u is displacement in the x-direction of the beam, v is displacement in the y-direction of the beam, a_W is the moment arm from the applied weight on the free bracket to the free end of the beam, and a_B is the moment arm from the center of mass of the bracket to the free end of the beam.

Simplifying,

$$W = P \left(\sin(\theta(l)) u(l) + \cos(\theta(l)) v(l) \right) + M \cos(\theta(l)) \theta(l) \quad (5.3)$$

where the total applied load is $P = P_W + P_B$ and the total applied moment is $M = P_W a_W + P_B a_B$.

It should be noted that the slope of the tip point is related to the deflection derivative using the following equation:

$$\theta(l) = \tan^{-1}(v_x(l)) \quad (5.4)$$

Next, the strain energy equations for both the axial and bending strain are defined, respectively, as:

$$U_A = \frac{1}{2}EA \int_0^l u_x^2 dx \quad (5.5)$$

$$U_B = \frac{1}{2}EI \int_0^l v_{xx}^2 dx \quad (5.6)$$

where E is the modulus of elasticity, A is the rectangular cross-sectional area, and I is the area moment of inertia of the rectangular cross-section. A and I are defined as:

$$A = wh \quad (5.7)$$

$$I = \frac{1}{12}wh^3 \quad (5.8)$$

Eqn. (5.9) and (5.10) lead to these two differential equations in terms of v and u :

$$v_{xxxx} = 0 \quad (5.9)$$

$$u_{xx} = 0 \quad (5.10)$$

These differential equations are subject to the following displacement boundary conditions:

$$v(0) = v_x(0) = u(0) = 0 \quad (5.11)$$

By solving Eqn. (5.9) and (5.10), the deflections u and v are defined as:

$$u(x) = Dx \quad (5.12)$$

$$v(x) = \frac{1}{6}Bx^3 + \frac{1}{2}Cx^2 \quad (5.13)$$

These differential equations have the following force boundary conditions:

$$P\cos(\theta(l)) = -Elv_{xxx}(l) \quad (5.14)$$

$$\begin{aligned} & -P\sin(\theta(l))\left(\frac{1}{1+v_x^2(l)}\right)v(l) - M\sin(\theta(l))\left(\frac{1}{1+v_x^2(l)}\right)\theta(l) \\ & + M\cos(\theta(l))\left(\frac{1}{1+v_x^2(l)}\right) + P\cos(\theta(l))\left(\frac{1}{1+v_x^2(l)}\right)u(l) = Elv_{xx}(l) \end{aligned} \quad (5.15)$$

$$P\sin(\theta(l)) = EAu_x(l) \quad (5.16)$$

or,

$$P\cos(\theta(l)) = -EIv_{xxx}(l) \quad (5.17)$$

$$\left(\frac{1}{1+v_x^2(l)}\right)\left((Pu(l) + M)\cos(\theta(l)) - (Pv(l) + M\theta(l))\sin(\theta(l))\right) = EIv_{xx}(l) \quad (5.18)$$

$$P\sin(\theta(l)) = EAu_x(l) \quad (5.19)$$

Using the force boundary conditions, the coefficients B , C , and D are found,

$$B = -\frac{P}{EI}\cos(\theta(l)) \quad (5.20)$$

$$C = \frac{\left((Pu(l) + M)\cos(\theta(l)) - (Pv(l) + M\theta(l))\sin(\theta(l))\right) + PL\cos(\theta(l))}{EI(1+v_x^2(l))} \quad (5.21)$$

$$D = \frac{P}{EA}\sin(\theta(l)) \quad (5.22)$$

It can be seen that B , C , and D are functions of the external forces, specimen dimensions, and $u(x)$, $v(x)$, and $v_x(x)$. These three equations can be solved simultaneously using the MATLAB® function `fsolve`, which requires an initial guess. It was decided to use the classical beam theory to provide the initial guess for the first step, i.e., a beam is deforming under the weight of the bracket. In this case the initial guesses for B , C , and D were $-\frac{P_B}{EI}$, $\frac{P_B l + P_B a_B}{EI}$, and $\frac{P_B l}{EA}$ respectively. Subsequently, the results of an iteration were used as the initial guesses for the next one. To ensure convergence of the solution, each load step was divided into ten sub-steps.

These deflection equations only described bending and axial deflection. They do not, however, account for the retraction along the x direction that is typically associated with large deformation, [68]. Based on Figure 5.1(b), the differential retraction, du_E , of the beam can be expressed as:

$$du_E = dx(1 - \cos(\theta)) = dx \left(2\sin^2 \left(\frac{\theta}{2} \right) \right) \quad (5.23)$$

By integrating this equation, the retraction of the tip point, u_E , can be obtained:

$$u_E = - \int_0^l \left(2\sin^2 \left(\frac{\tan^{-1}(v_x)}{2} \right) \right) dx \quad (5.24)$$

Applying the derivative of Eqn. (5.9), the tip point retraction equation becomes:

$$u_E = - \int_0^l \left(2\sin^2 \left(\frac{\tan^{-1} \left(\frac{1}{2} Bx^2 + Cx \right)}{2} \right) \right) dx \quad (5.25)$$

The total deformation of the tip point can be expressed as a combination of this retraction in addition to the extension caused by the axial portion of the applied loads, $(P_W + P_B)\sin(\theta(l))$:

$$u(l) = - \int_0^l \left(2\sin^2 \left(\frac{\tan^{-1} \left(\frac{1}{2} Bx^2 + Cx \right)}{2} \right) \right) dx + Dl \quad (5.26)$$

$$v(l) = \frac{1}{6} Bl^3 + \frac{1}{2} Cl^2 \quad (5.27)$$

A complete derivation of the MEB method is found in Appendix B.

It should be noted that the equations derived here for the MEB method do not account for the nonlinear behavior of NinjaFlex[®] and is therefore an approximation. Since the value of the elastic modulus can vary depending on the circumstances of the specimens, it was decided to use the experimental stress-strain curve from a previous study, Figure 5.2, [9]. Their tensile specimens have a similar ratio of infill to wall region as our bending test specimens.

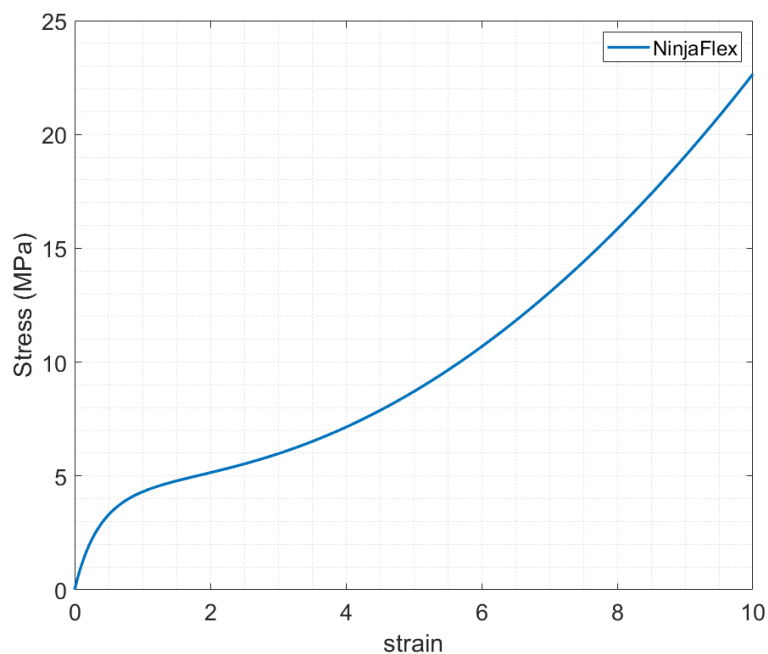


Figure 5.2: Tensile stress-strain curve for NinjaFlex[®], [9]

Based on the stress strain curve of Figure 5.2, the elastic modulus, E , was assigned a value of 9.45 MPa by calculating the slope of the linear range of the stress–strain curve: 0 to 0.2 m/m, [9]. This value is lower than that reported by the manufacturer as well as our 225°C infill and wall

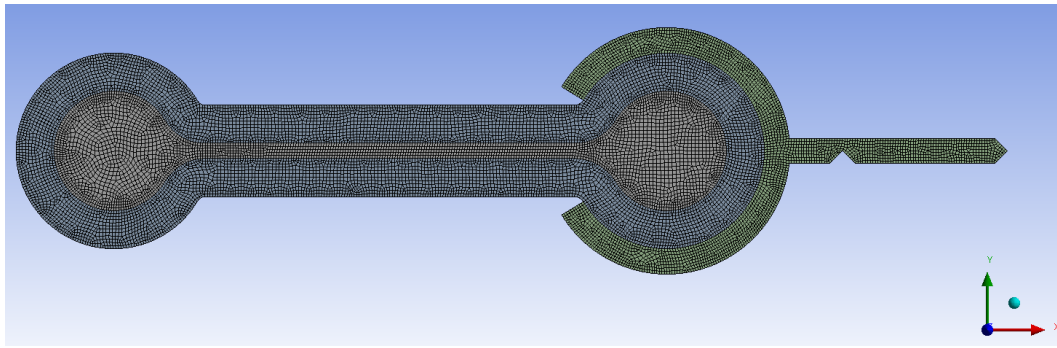
region elastic modulus values, but falls within the range reported by other researchers, between 5.24–12.2 MPa Table 2.1, [7–9,38,57].

5.2 Finite element analysis modeling

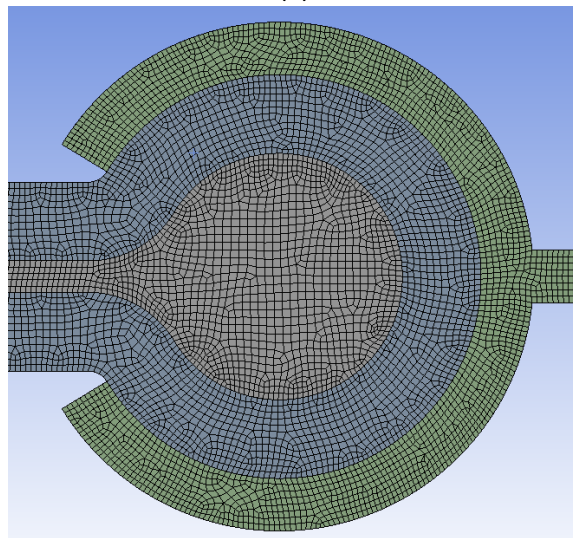
Several researchers have investigated the factors that affect the modeling of 3D printed components using FEA, [69,70]. These studies did not consider hyperelasticity of the 3D printed material, large deflections, or the region-specific material properties. We aim to include these factors for better understanding of the behavior of 3D printed hyperelastic polymers.

ANSYS® (simulation software, ANSYS, Inc., Canonsburg, Pennsylvania, United States) was used for the FEA simulations, [71]. The models of the specimens were imported as a 2D IGES file and processed as plane stress problems. The free end bracket was simplified from the one used in the experiments, Figure 5.2(a), to reduce the computational load of the simulations. To ensure that this model was comparable to the experiment, two issues were addressed. Firstly, the specimen geometry model was split into the infill and wall regions as per the actual specimens from Chapter 4; each region was assigned respective material properties found in Chapter 3. Secondly, the effect of gravity on the beam joints was not considered, so gravity was turned off in the simulation. Therefore, to ensure that the contribution of the free end bracket weight was properly considered, it was applied as an external force at the center of gravity's location. Consequentially, the material properties of the free end bracket were free to be any material that was sufficiently stiffer than the NinjaFlex® material models. For simplicity, the bracket was assigned structural steel material properties.

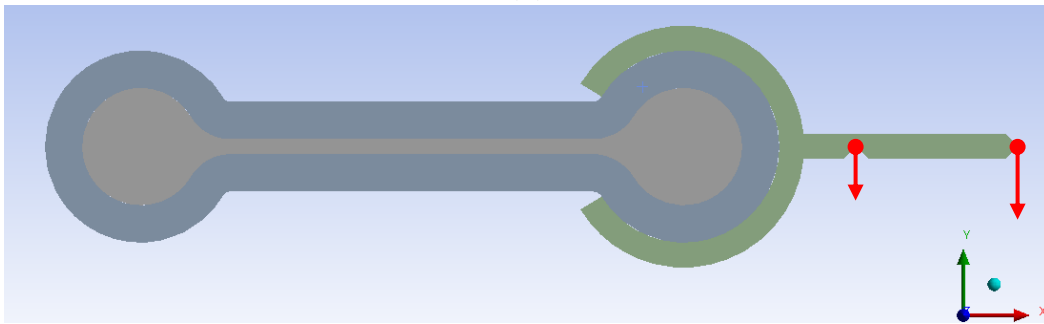
The setup and conditions of the deflection simulations are found in Figure 5.3. A mesh stability study was conducted, and it was found that an average element size of 0.10 mm was stable, Figure 5.3(a) and (b). The number of elements in simulations ranged from 5603 elements in Specimens 1–3 to 12,756 in Specimens 16–18. The weight of the free end bracket and tension loads were applied, Figure 5.3(c), the values of which are found in Table 4.3.



(a)



(b)



(c)

Figure 5.3: FEA setup of bending experiments, the green represents the free end bracket, the blue area represents the wall region of the specimen, and the gray area represents the infill region of the specimen; (a) typical mesh density; (b) image of zoomed mesh; (c) applied forces

5.3 Comparison of analytical, finite element, and experimental results

The results of the MEB method were compared to the experiment x and y deflections in Figure 5.5. The MEB method reasonably predicted the deflection of the relatively stiff Specimen 15, Figure 5.5(a) and (b). The deflection was overestimated for the lower loads and then underestimated as the load increased. For Specimen 1, the MEB lagged behind the experimental results, although it followed the average experimental tip point curvature, Figure 5.5(c) and (d). The MEB method worked generally well for stiff specimens, such as Specimen 15. For all tested specimens, the curvature of the MEB deflection consistently followed the curvature of the experiments.

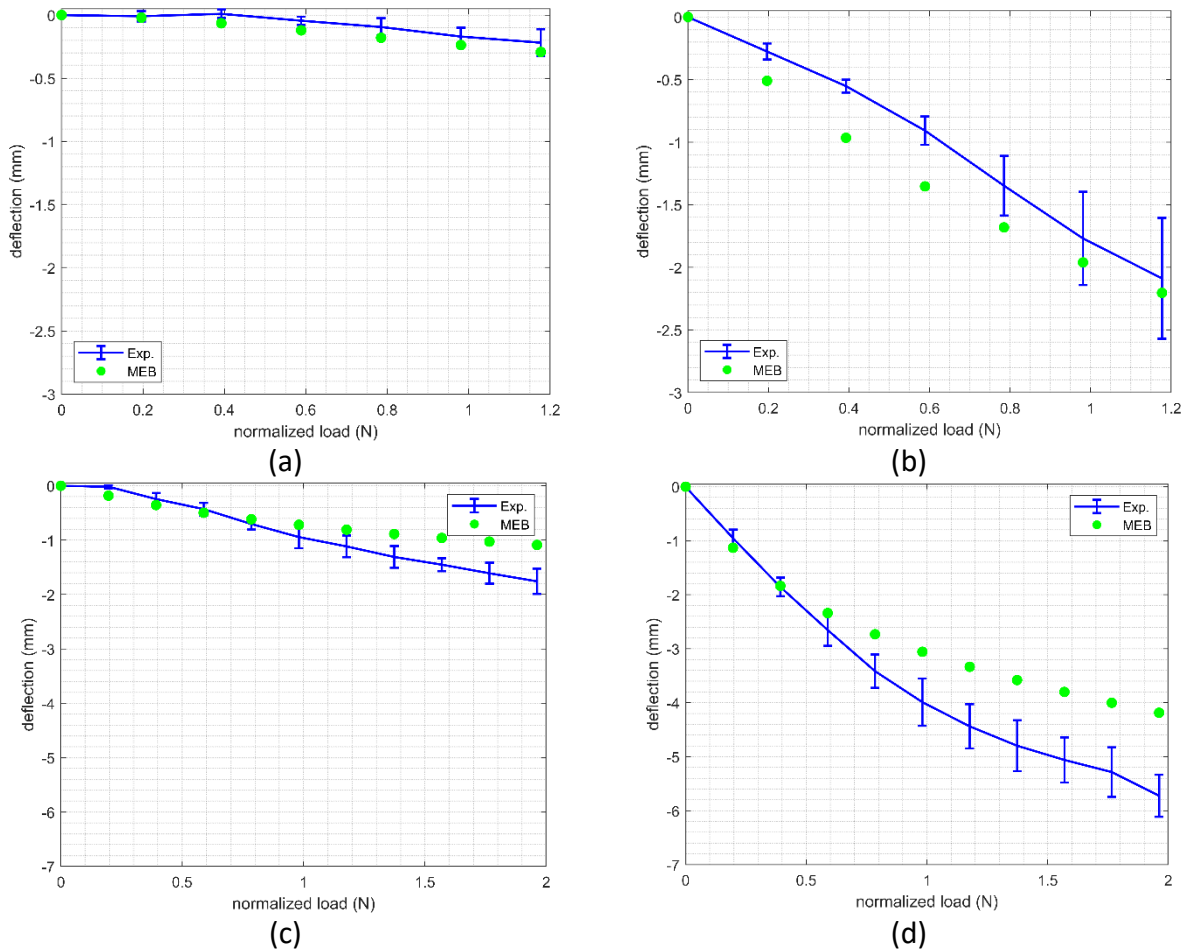


Figure 5.4: Comparison of experimental results to the MEB method; (a) a relatively stiff Specimen 15; (b) a relatively flexible Specimen 1

The FEA method slightly overestimated the deflection of Specimen 15, Figure 5.6(a) and (b). Similar to MEB, the curvature of the FEA tip point deflection matched the experiment well. However, the FEA resulted in an overestimation of the tip point retraction in the case of Specimen 1, as shown in Figure 5.6(c). A possible reason for this behavior may be due to the way ANSYS analyzes bodies experiencing large deflection. When a body experiences large strain, the deformation triggers reorientation of the applied loads. It may be possible that this load distribution was less accurate, resulting in the excessive retraction that can be observed in the figure. Also, the material model is based on uniaxial tensile data. The TPU may not behave

symmetrically for compression as it does in tension; the bottom edge of the bending model would therefore behave differently.

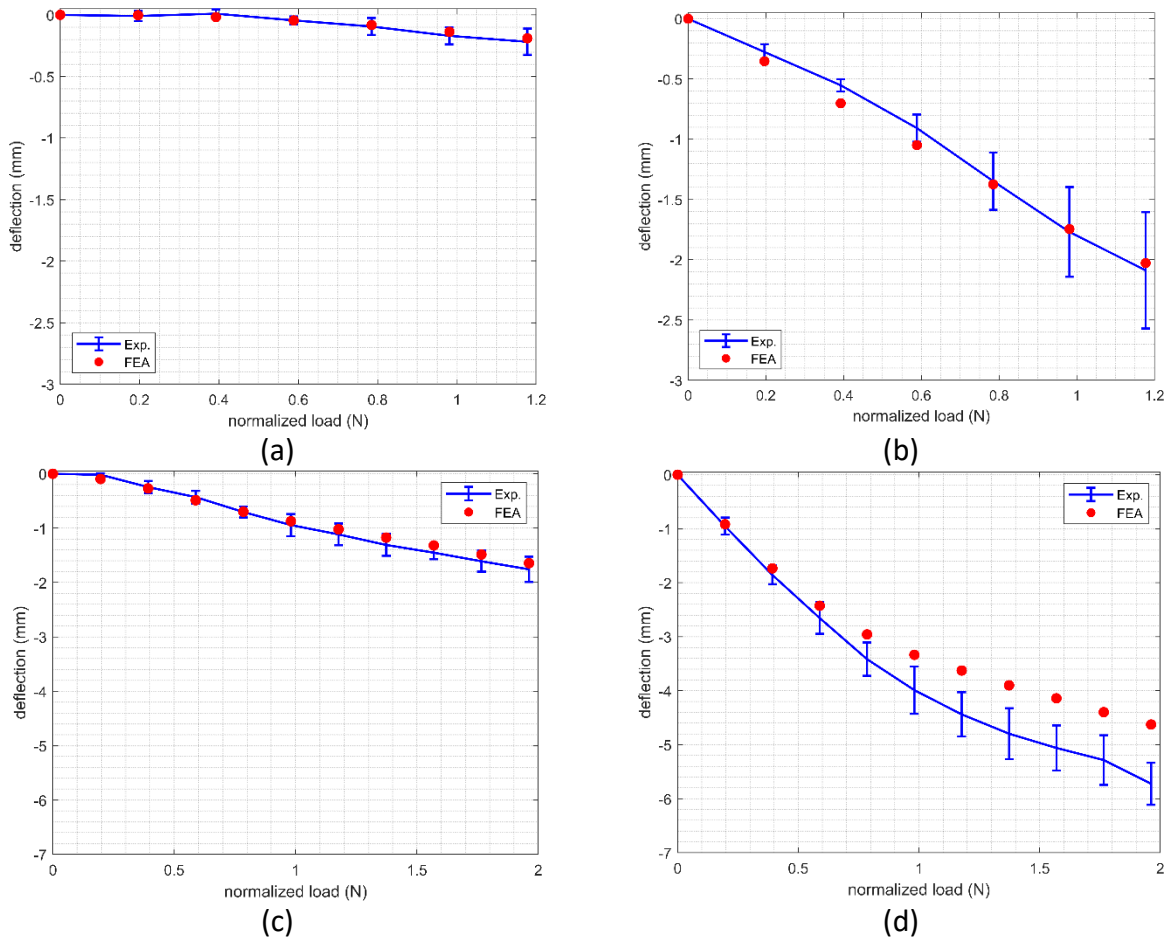


Figure 5.5: Comparison of experimental results to the FEA method; (a) a relatively stiff Specimen 15; (b) a relatively flexible Specimen 1

To compare the experimental and modeling data, a measure of the difference of each loading case of a specimen was performed. These measures were averaged as follows:

$$Z_{m,i} = \frac{\sum_{j=1}^{J_i} \sqrt{(x_{e,i,j} - x_{m,i,j})^2 + (y_{e,i,j} - y_{m,i,j})^2}}{J_i (l_i + a_{w_i})} \quad (5.28)$$

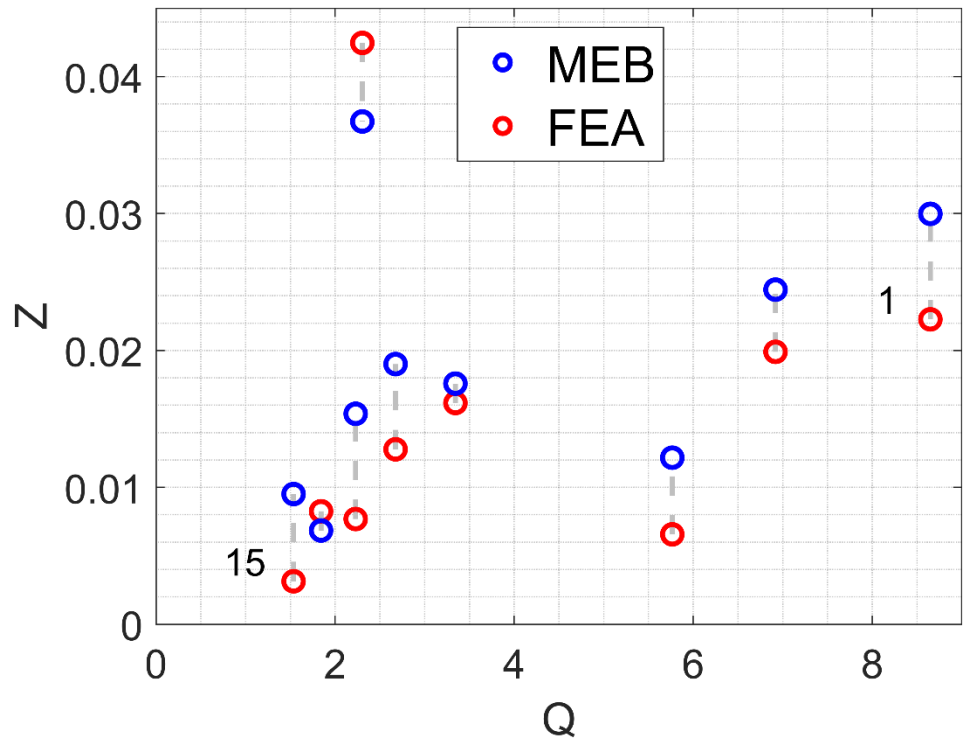
where m is the modeling method (MEB or FEA), i is the specimen number, j is the load number, J_i is total number of loads, x_e , x_m , y_e and y_m are the experiment and model deflection in the x and y directions, respectively, l_i is the length of the specimen, and a_{w_i} is the moment arm of the applied load.

All results from experiments, MEB, and FEA were combined using the following nondimensional stiffness parameter, Q , [72–74]:

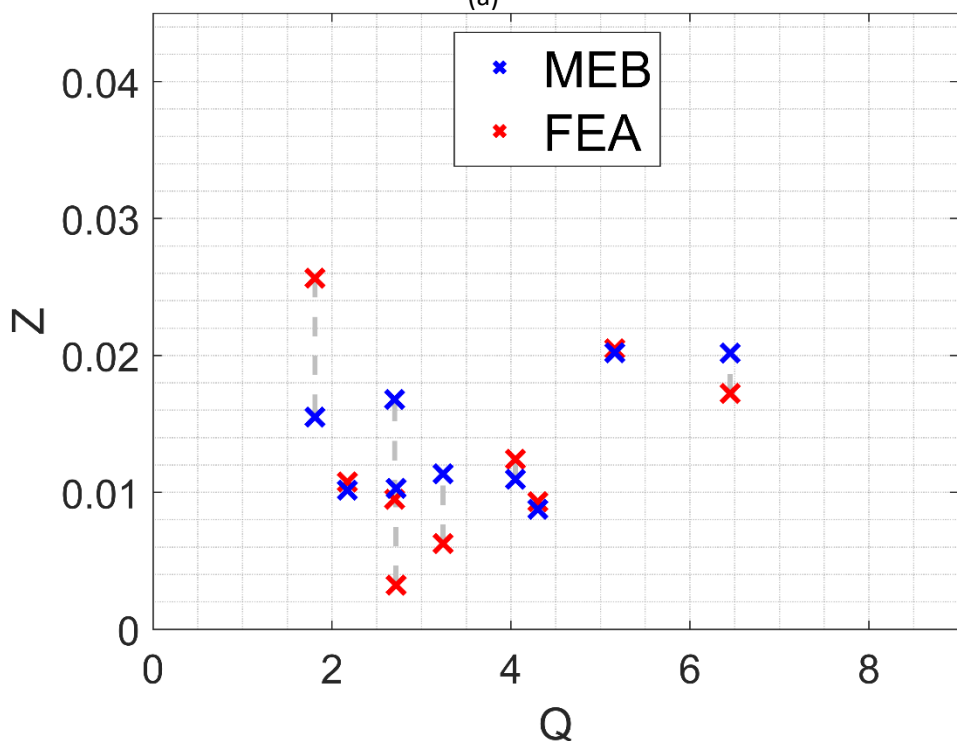
$$Q_i = \frac{(P_{B_i} + \max(P_{W_i}))(l_i + a_{w_i})^2}{EI_i} \quad (5.29)$$

It should be noted that lower Q values typically correspond to higher bending stiffness.

Overall, both MEB and FEA underestimated the deflection of most specimens when compared to the respective experimental results. The results of the average difference, Z_m , were plotted with respect to the non-dimensional parameter Q , Figure 5.7. The data were split by length for clarity. For specimens with $l = 10$ mm length, Figure 5.7(a), both MEB and FEA predictions were of the same order for values of Q below 4. The same observation was valid for all tested specimens in the case of $l = 15$ mm, Figure 5.7(b). However, when l was equal to 10 mm and Q was above 5, the FEA was more accurate. However, the retraction along the x direction was significantly higher than that with MEB, where the displacement closely followed the experimental curve. It was also observed that the FEA showed more stable Z values as Q increased.



(a)



(b)

Figure 5.6: Deviation of MEB and FEA with respect to average experimental results; (a) Specimens with $l = 10$ mm; (b) Specimens with $l = 15$ mm

One specimen showed significantly higher error than the others: Specimen 13. There is a strong possibility that the experimental Specimen 13 was printed incorrectly, as specimens with similar dimensions, such as Specimens 14 and 15, exhibit significantly lower deflection magnitudes. It would be of interest to reprint Specimen 13 and retest it in future work to confirm this.

Overall, our hypothesis was proven correct. Despite MEB having consistently higher non-dimensional error, the magnitude of error was still in the same order of FEA and was even lower for some specimen. The MEB method provides a viable option for predicting the behavior of TPU flexible joints.

Chapter 6: Modeling and experimental validation of the flexion of tendon-actuated prosthetic finger with flexible 3D printed hyperelastic thermoplastic polyurethane joints

6.1 3-digit prosthetic finger modeling

The objective of this research was to determine the relationship between the tension in the tendon and joint angles of a prosthetic finger. Since the motion of the finger digits is reasonably slow, it is reasonable to study the finger as a sequence of static equilibrium conditions (quasi-static conditions). The principle of virtual work was applied to a three-digit prosthetic finger actuated by tensile force to a single tendon that runs through all digits, [75]. Fig. 6.1 shows the prosthetic finger, a diagram of the key components of the finger, and the equivalent, simplified model of the finger used for analysis. It should be noted that the flexible beams in the physical prosthesis have been replaced in the model with revolute joints and torsional springs. Therefore, the digits of the prosthetic finger were artificially extended, Figure 6.3(c), to maintain a comparable configuration to the original design, Figure 6.3(b). The effects of gravity acting on the finger digits were considered.

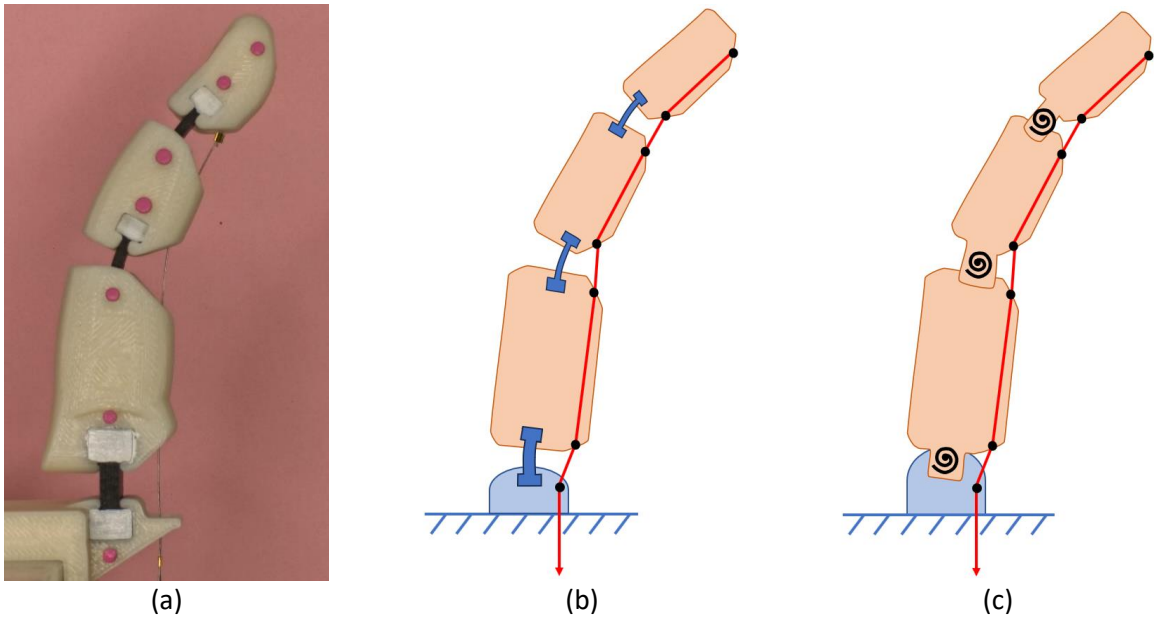


Figure 6.1: Prosthetic Finger Diagram; a) original 3D printed finger; b) diagram of original finger; c) diagram of finger with torsional springs

6.1.1 Kinematic analysis of the 3-digit prosthetic finger

Fundamental kinematic parameters were defined in Appendix D. It is recommended that those unfamiliar with computational kinematics check this Appendix before proceeding. Local frames were assigned to each digit, Figure 6.2. The origin of each local frame coincides with the center of mass for each digit. A tension force, T , is applied in the negative y direction of the global frame. This tendon is assumed to be inextensible. The definitions of the local position vectors for tendon and joint locations were provided in Table 6.1.

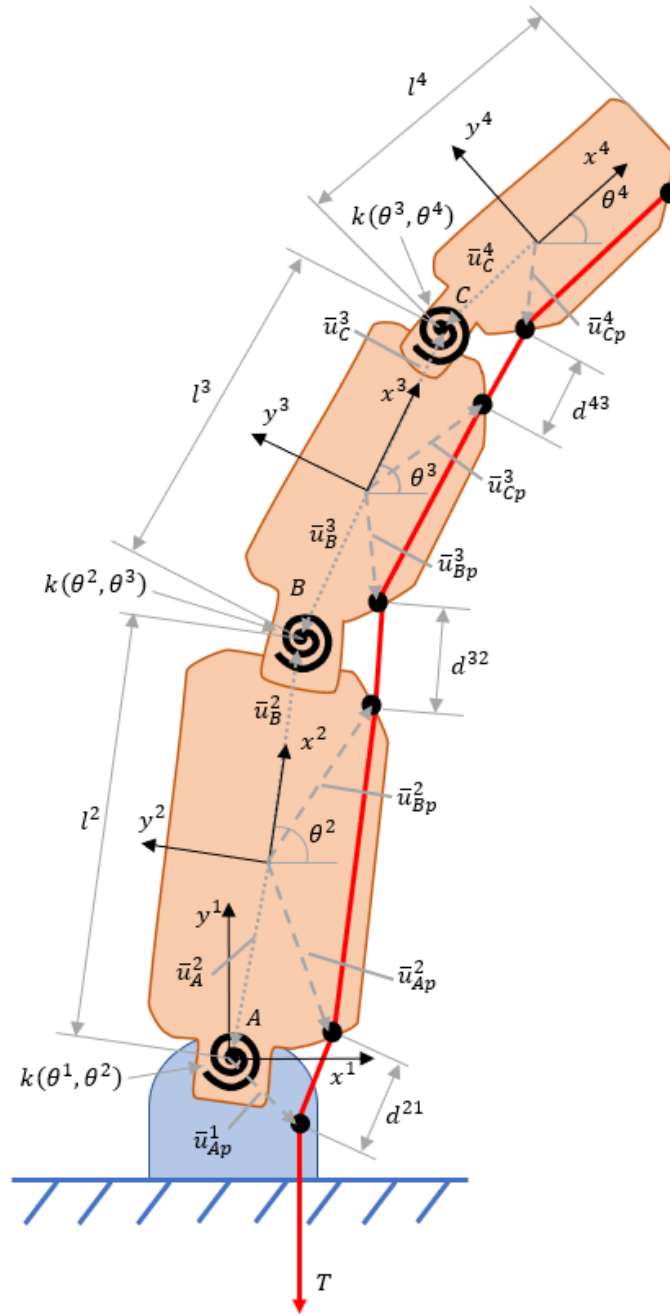


Figure 6.2: Diagram of local frames and coordinate vectors

Table 6.1: Local coordinates of finger model

Definition	Description
$\bar{u}_A^1 = [u_{Ax}^1 \ u_{Ay}^1]^T$	Location of joint A with respect to local frame x^1, y^1
$\bar{u}_A^2 = [u_{Ax}^2 \ u_{Ay}^2]^T$	Location of joint A with respect to local frame x^2, y^2
$\bar{u}_B^2 = [u_{Bx}^2 \ u_{By}^2]^T$	Location of joint B with respect to local frame x^2, y^2
$\bar{u}_B^3 = [u_{Bx}^3 \ u_{By}^3]^T$	Location of joint B with respect to local frame x^3, y^3
$\bar{u}_C^3 = [u_{Cx}^3 \ u_{Cy}^3]^T$	Location of joint C with respect to local frame x^3, y^3
$\bar{u}_C^4 = [u_{Cx}^4 \ u_{Cy}^4]^T$	Location of joint C with respect to local frame x^4, y^4
$\bar{u}_{Ap}^1 = [u_{Apx}^1 \ u_{Apy}^1]^T$	Location of the tendon opening at joint A with respect to local frame x^1, y^1
$\bar{u}_{Ap}^2 = [u_{Apx}^2 \ u_{Apy}^2]^T$	Location of the tendon opening at joint A with respect to local frame x^2, y^2
$\bar{u}_{Bp}^2 = [u_{Bpx}^2 \ u_{Bpy}^2]^T$	Location of the tendon opening at joint B with respect to local frame x^2, y^2
$\bar{u}_{Bp}^3 = [u_{Bpx}^3 \ u_{Bpy}^3]^T$	Location of the tendon opening at joint B with respect to local frame x^3, y^3
$\bar{u}_{Cp}^3 = [u_{Cpx}^3 \ u_{Cpy}^3]^T$	Location of the tendon opening at joint C with respect to local frame x^3, y^3
$\bar{u}_{Cp}^4 = [u_{Cpx}^4 \ u_{Cpy}^4]^T$	Location of the tendon opening at joint C with respect to local frame x^4, y^4

Now we define the kinematic joint constraint equations, C , for the finger system of Figure 6.2. C

for this system is a 9x1 matrix. R^i and A^i are defined in Appendix D.

$$C = \begin{Bmatrix} R^1 \\ \theta^1 \\ R^2 + A^2 \bar{u}_A^2 - R^1 - A^1 \bar{u}_A^1 \\ R^3 + A^3 \bar{u}_B^3 - R^2 - A^2 \bar{u}_B^2 \\ R^4 + A^4 \bar{u}_C^4 - R^3 - A^3 \bar{u}_C^3 \end{Bmatrix} = 0 \quad (6.1)$$

The coordinate matrix of the system, q , is equivalent to,

$$q = \begin{Bmatrix} R^1 \\ \theta^1 \\ R^2 \\ \theta^2 \\ R^3 \\ \theta^3 \\ R^4 \\ \theta^4 \end{Bmatrix} \quad (6.2)$$

At this stage, it should be mentioned that the study of both velocities and static forces are related to the Jacobian matrix, C_q , which is the partial derivatives of C with respect to q :

$$C_q = \frac{\partial C}{\partial q} = \begin{pmatrix} I & 0 & 0 & 0 & 0 & 0 & 0 & 0 \\ 0 & 1 & 0 & 0 & 0 & 0 & 0 & 0 \\ -I & -A_{\theta}^1 \bar{u}_A^1 & I & A_{\theta}^2 \bar{u}_A^2 & 0 & 0 & 0 & 0 \\ 0 & 0 & -I & -A_{\theta}^2 \bar{u}_B^2 & I & A_{\theta}^3 \bar{u}_B^3 & 0 & 0 \\ 0 & 0 & 0 & 0 & -I & -A_{\theta}^3 \bar{u}_C^3 & I & A_{\theta}^4 \bar{u}_C^4 \end{pmatrix} = 0 \quad (6.3)$$

where I represents a 2x2 identity matrix. Note that the number of rows in C_q is equal to the number of constraint equations while the number of columns is equivalent to the number of coordinates in the system.

As q is a general matrix describing the motion of the system, it is important to express the static balance problem in terms of the independent coordinates, which can be done by splitting q into dependent and independent variables:

$$q = \begin{Bmatrix} q_d \\ q_i \end{Bmatrix} \quad (6.4)$$

where,

$$q_d = \begin{Bmatrix} R^1 \\ \theta^1 \\ R^2 \\ R^3 \\ R^4 \end{Bmatrix} \quad (6.5)$$

$$q_i = \begin{Bmatrix} \theta^2 \\ \theta^3 \\ \theta^4 \end{Bmatrix} \quad (6.6)$$

The virtual work is based on introducing arbitrary displacements, δq , into the system. The virtual work associated with the displacement must be equal to zero for static balance. It is easy to see that $C_q \delta q = 0$. This equation can be partitioned as,

$$C_{qd} \delta q_d + C_{qi} \delta q_i = 0 \quad (6.7)$$

where,

$$C_{qd} = \begin{bmatrix} I & 0 & 0 & 0 & 0 \\ 0 & 1 & 0 & 0 & 0 \\ -I & -A_\theta^1 \bar{u}_A^1 & I & 0 & 0 \\ 0 & 0 & -I & I & 0 \\ 0 & 0 & 0 & -I & I \end{bmatrix} \quad (6.8)$$

$$C_{qi} = \begin{bmatrix} 0 & 0 & 0 \\ 0 & 0 & 0 \\ A_\theta^2 \bar{u}_A^2 & 0 & 0 \\ -A_\theta^2 \bar{u}_B^2 & A_\theta^3 \bar{u}_B^3 & 0 \\ 0 & -A_\theta^3 \bar{u}_C^3 & A_\theta^4 \bar{u}_C^4 \end{bmatrix} \quad (6.9)$$

Lastly, we solve for the dependent variables in terms of the independent variables:

$$\delta q_d = -C_{qd}^{-1} C_{qi} \delta q_i = B \delta q_i \quad (6.10)$$

6.1.2 Quasi-static analysis of the 3-digit prosthetic finger using the principle of virtual work

To describe the virtual work done in the system, several assumptions must be defined. Firstly, gravity is active in the negative y^1 direction. There are virtual work terms that are associated with the gravity effects on the three digits. It is assumed that gravity effects on the joints are negligible. Next, the tendon is inextensible. This means that the work done by the force acting on the tendon is a function of the change in tendon length between each two digits, d^{21} , d^{32} , and d^{43} in Figure 6.2. As described in Section 6.1, the flexible beam joints were substituted

with equivalent nonlinear torsional springs and revolute joints, Appendix E. The virtual work of the prosthetic finger is,

$$\begin{aligned}
\delta W = & T(\delta d^{21} + \delta d^{32} + \delta d^{43}) \\
& -(a_A(\theta^0 - \theta^2)^2 + b_A(\theta^0 - \theta^2))(-\delta\theta^2) \\
& -(a_B(\theta^2 - \theta^3)^2 + b_B(\theta^2 - \theta^3))(\delta\theta^2 - \delta\theta^3) \\
& -(a_C(\theta^3 - \theta^4)^2 + b_C(\theta^3 - \theta^4))(\delta\theta^3 - \delta\theta^4) \\
& -m^2 g \delta R_y^2 - m^3 g \delta R_y^3 - m^4 g \delta R_y^4
\end{aligned} \tag{6.11}$$

where θ^0 is the initial angle of the proximal digit.

To begin, we first addressed the work done by the tension in the tendon. The distance $\delta d^{i+1,i}$ is defined as the change in the Euclidean length of the tendon between two bodies $i + 1$ and i at a given joint, J , which can be either A , B , or C ,

$$d^{i+1,i} = \left(r_j^{i+1,iT} r_j^{i+1,i} \right)^{\frac{1}{2}} \tag{6.12}$$

The vector composing the tendon distance is formed by noting where the tendon exits one body, i , and enters the next, $i + 1$, or

$$r_j^{i+1,i} = R^{i+1} + A^{i+1} \bar{u}_{jp}^{i+1} - R^i - A^i \bar{u}_{jp}^i \tag{6.13}$$

The variation of $\delta d^{i+1,i}$ is,

$$\delta d^{i+1,i} = \frac{\partial d^{i+1,i}}{\partial q^{i+1,i}} \delta q^{i+1,i} = \frac{1}{2} \left(r_j^{i+1,iT} r_j^{i+1,i} \right)^{-\frac{1}{2}} \left(2 r_j^{i+1,iT} \right) \frac{\partial r_j^{i+1,i}}{\partial q^{i+1,i}} \delta q^{i+1,i}$$

Or,

$$\delta d^{i+1,i} = \left(\frac{r_j^{i+1,iT}}{\left(r_j^{i+1,iT} r_j^{i+1,i} \right)^{\frac{1}{2}}} \right) \frac{\partial r_j^{i+1,i}}{\partial q^{i+1,i}} \delta q^{i+1,i} \tag{6.14}$$

where $\delta q^{i+1,i}$ is a subset of δq corresponding to bodies $i + 1$ and i . It is known that the denominator of Eqn. (6.14) is equivalent to the length of the tendon segment corresponding to each joint, Eqn. (6.14), or

$$\delta d^{i+1,i} = \left(\frac{r_j^{i+1,iT}}{d^{i+1,i}} \right) \frac{\partial r_j^{i+1,i}}{\partial q^{i+1,i}} \delta q^{i+1,i} \quad (6.15)$$

Substituting Eqn. (6.11) in the above equation,

$$\delta d^{i+1,i} = \frac{r_j^{i+1,iT}}{d^{i+1,i}} \left(\frac{\partial (R^{i+1} + A^{i+1} \bar{u}_j^{i+1} - R^i - A^i \bar{u}_j^i)}{\partial q^{i+1,i}} \right) \delta q^{i+1,i}$$

Or,

$$\delta d^{i+1,i} = \frac{r_j^{i+1,iT}}{d^{i+1,i}} \left[I \quad A_\theta^{i+1} \bar{u}_{jp}^{i+1} \quad -I \quad -A_\theta^i \bar{u}_{jp}^i \right] \begin{Bmatrix} \delta R^{i+1} \\ \delta \theta^{i+1} \\ \delta R^i \\ \delta \theta^i \end{Bmatrix} \quad (6.16)$$

Incorporating the B matrix, the equation can be expressed in terms of δq_i ,

$$\delta d^{i+1,i} = \frac{r_j^{i+1,iT}}{d^{i+1,i}} \left[I \quad A_\theta^{i+1} \bar{u}_{jp}^{i+1} \quad -I \quad -A_\theta^i \bar{u}_{jp}^i \right] \begin{Bmatrix} B(R^{i+1}, :) \delta q_i \\ \delta \theta^{i+1} \\ B(R^i, :) \delta q_i \\ \delta \theta^i \end{Bmatrix} \quad (6.17)$$

where $B(R^i, :)$ represents the row of the B matrix that corresponds to the dependent coordinates R^i . Rearranging,

$$\delta d^{i+1,i} = \frac{r_j^{i+1,iT}}{d^{i+1,i}} \left[A_\theta^{i+1} \bar{u}_{jp}^{i+1} \quad -A_\theta^i \bar{u}_{jp}^i \quad I \quad -I \right] \begin{Bmatrix} \delta \theta^{i+1} \\ \delta \theta^i \\ B(R^{i+1}, :) \delta q_i \\ B(R^i, :) \delta q_i \end{Bmatrix}$$

Expanding,

$$\delta d^{i+1,i} = \frac{r_j^{i+1,iT}}{d^{i+1,i}} \left([A_\theta^{i+1} \bar{u}_{jp}^{i+1} \quad -A_\theta^i \bar{u}_{jp}^i] \begin{Bmatrix} \delta \theta^{i+1} \\ \delta \theta^i \end{Bmatrix} + (B(R^{i+1}, :) - B(R^i, :)) \delta q_i \right) \quad (6.18)$$

As can be seen, $\delta d^{i+1,i}$ is function of the variations of the three independent coordinates.

The work done by the digit weights is in terms of δR_y^i , we simply write it in terms of δq_i ,

$$\begin{aligned} & -m^2 g \delta R_y^2 - m^3 g \delta R_y^3 - m^4 g \delta R_y^4 = \\ & -m^2 g B(R_y^2, :) \delta q_i - m^3 g B(R_y^3, :) \delta q_i - m^4 g B(R_y^4, :) \delta q_i \end{aligned} \quad (6.19)$$

Expressing the above equation in terms of the independent variables,

$$\begin{aligned} & -m^2 g B(R_y^2, :) \delta q_i - m^3 g B(R_y^3, :) \delta q_i - m^4 g B(R_y^4, :) \delta q_i = \\ & \quad \left(-m^2 g B(R_y^2, 1) - m^3 g B(R_y^3, 1) - m^4 g B(R_y^4, 1) \right) \delta \theta^2 \\ & \quad + \left(-m^2 g B(R_y^2, 2) - m^3 g B(R_y^3, 2) - m^4 g B(R_y^4, 2) \right) \delta \theta^3 \\ & \quad + \left(-m^2 g B(R_y^2, 3) - m^3 g B(R_y^3, 3) - m^4 g B(R_y^4, 3) \right) \delta \theta^4 \end{aligned} \quad (6.20)$$

Since the virtual displacements in the virtual work equation cannot be zero, the coefficients of the virtual displacements must equal zero, leading to the following three equations:

For $\delta \theta^2$,

$$\begin{aligned} & T(\delta d_{\theta_2}^{21} + \delta d_{\theta_2}^{32} + \delta d_{\theta_2}^{43}) \\ & + (a_A(\theta^0 - \theta^2)^2 + b_A(\theta^0 - \theta^2)) \\ & - (a_B(\theta^2 - \theta^3)^2 + b_B(\theta^2 - \theta^3)) \\ & - m^2 g B(R_y^2, 1) - m^3 g B(R_y^3, 1) - m^4 g B(R_y^4, 1) = 0 \end{aligned} \quad (6.21)$$

Where the subscript, θ^2 , denotes the coefficient of $\delta \theta^2$ from Eqn. (6.15). For $\delta \theta^3$,

$$\begin{aligned} & T(\delta d_{\theta_3}^{21} + \delta d_{\theta_3}^{32} + \delta d_{\theta_3}^{43}) \\ & + (a_B(\theta^2 - \theta^3)^2 + b_B(\theta^2 - \theta^3)) \\ & - (a_C(\theta^3 - \theta^4)^2 + b_C(\theta^3 - \theta^4)) \\ & - m^2 g B(R_y^2, 2) - m^3 g B(R_y^3, 2) - m^4 g B(R_y^4, 2) = 0 \end{aligned} \quad (6.22)$$

For $\delta\theta^4$,

$$\begin{aligned} & T(\delta d_{\theta_4}^{21} + \delta d_{\theta_4}^{32} + \delta d_{\theta_4}^{43}) \\ & + (a_c(\theta^3 - \theta^4)^2 + b_c(\theta^3 - \theta^4)) \\ & - m^2 g B(R_y^2, 3) - m^3 g B(R_y^3, 3) - m^4 g B(R_y^4, 3) = 0 \end{aligned} \quad (6.23)$$

We now have three equations and four unknowns, T , θ^2 , θ^3 , and θ^4 . To solve for a unique solution, we must define at least one of the unknown variables. Since our goal is to understand how a tension load on the tendon deflects the fingers, we will define the tension, T , which will lead to unique joint angles.

6.2 Experimentation

6.2.1 Materials and preparation

The original finger joint and digit design for the prosthetic hand utilized a cylindrical shaped connection, see Chapter 4; these were modified to rectangular to reduce the possibility of the joint slippage and twisting in the channels of the digits. The proximal, middle, and distal joints have the same geometric design, Figure 6.3. The dimensions of the joints can be found in Table 6.2.

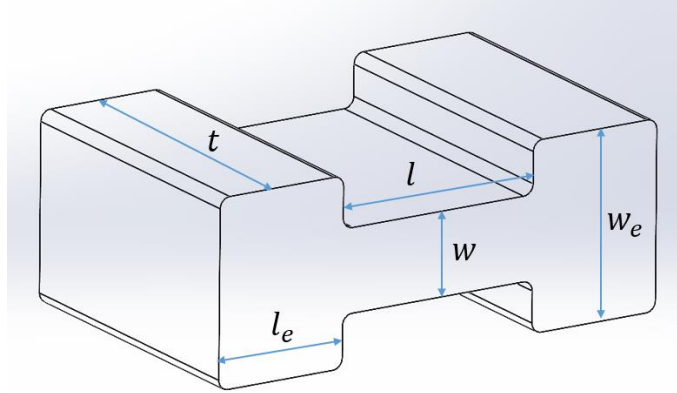


Figure 6.3: Diagram of modified finger joints

Table 6.2: Dimensions of proximal and middle/distal joints

Configuration	l (mm)	w (mm)	t (mm)	l_e (mm)	w_e (mm)
Proximal	10.0	4.0	15.0	6.5	9.0
Middle/Distal	10.0	2.0	12.0	4.5	6.5

The joints were designed using SolidWorks® and uploaded to the slicing software Cura® Lulzbot Edition to create the printer g-code, [53,76]. All joints were printed on a Lulzbot Taz Mini 2, [55], with the same print parameters, Table 6.3. Three sets of joints were printed for testing.

Table 6.3: Lulzbot Taz Mini 2 printing parameters for finger joints

Print Settings	Value
Print Temperature	235°C
Infill Density	100%
Infill Pattern	Lines
Wall Line Count	2

To assist in image processing and model validation, raised circular markers, 3 mm in diameter, were added to the digits, Figure 6.4(a). These markers allowed the identification of the digits. Paint was applied to these markers.

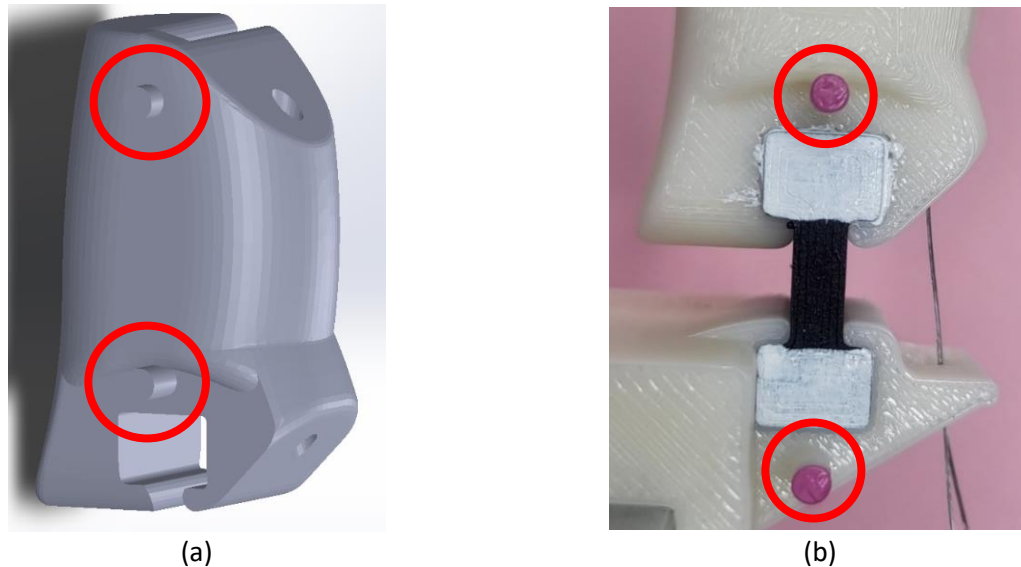


Figure 6.4: Painted ends of the finger joints and markers; a) raised markers on digits; b) painted markers and joint ends

A custom bracket was designed to hold the finger mechanism fixed during experiments, Figure 6.5. The base bracket was printed on a Stratasys Fortus 250mc with ABSplus P430 filament at 100% infill, [64,65]. The bracket contains a channel to fix the finger proximal joint and to maintain the finger in a vertical configuration when unloaded. A channel running the length of the base bracket allowed for fixing the base to an optical table using two $\frac{1}{4}$ x20 bolts to be inserted. A small guide hole ensured that the actuating tendon does not deviate during the flexion of the finger. A painted marker was added to the base bracket to represent the base in the image processing phase.

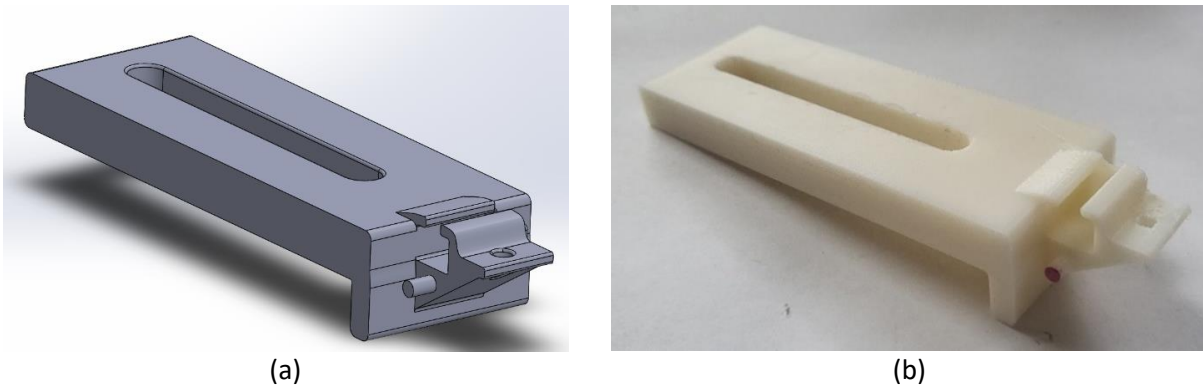
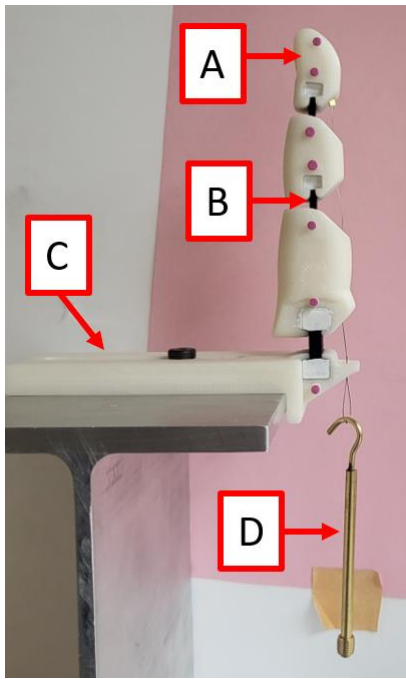


Figure 6.5: Base bracket design; a) CAD model; b) printed bracket

6.2.2 Experimental setup

Firstly, the finger digits and base bracket were assembled with the corresponding finger joints. A 0.38 mm braided stainless-steel tendon was fixed to the distal joint and ran through the tendon channels in each digit and out of the guide in the base bracket. The finger and base bracket were then bolted to a fixed table or mounting point, Figure 6.6.



(a)



(b)

Figure 6.6: Assembled finger bending experiment setup; (a) finger with diagram: A) finger digits; B) finger joints; C) base bracket; D) hook for holding applied weights; (b) typical bent finger

Next, a series of incrementing weights were attached to the free end of the tendon, letting the finger come to a static configuration before the next load was applied, Table 6.4.

Table 6.4: Full finger bending experiment loading conditions

Load Property	Applied Load Mass Value (g)
Hook Mass	8.2
Initial condition	0
Load Increment	20
Maximum Incremental Load	240
Maximum Total Load	248.2

All experiments and trials were recorded with a GoPro Hero 10 camera with a Nikon NIKKOR 18-140 mm lens in 5.3k resolution, or 15.8 MP, at 30 frames per second. The camera was located approximately 0.5 meters away, Figure 6.7. The experiment was conducted three times per set of joints, resulting in nine total trials.

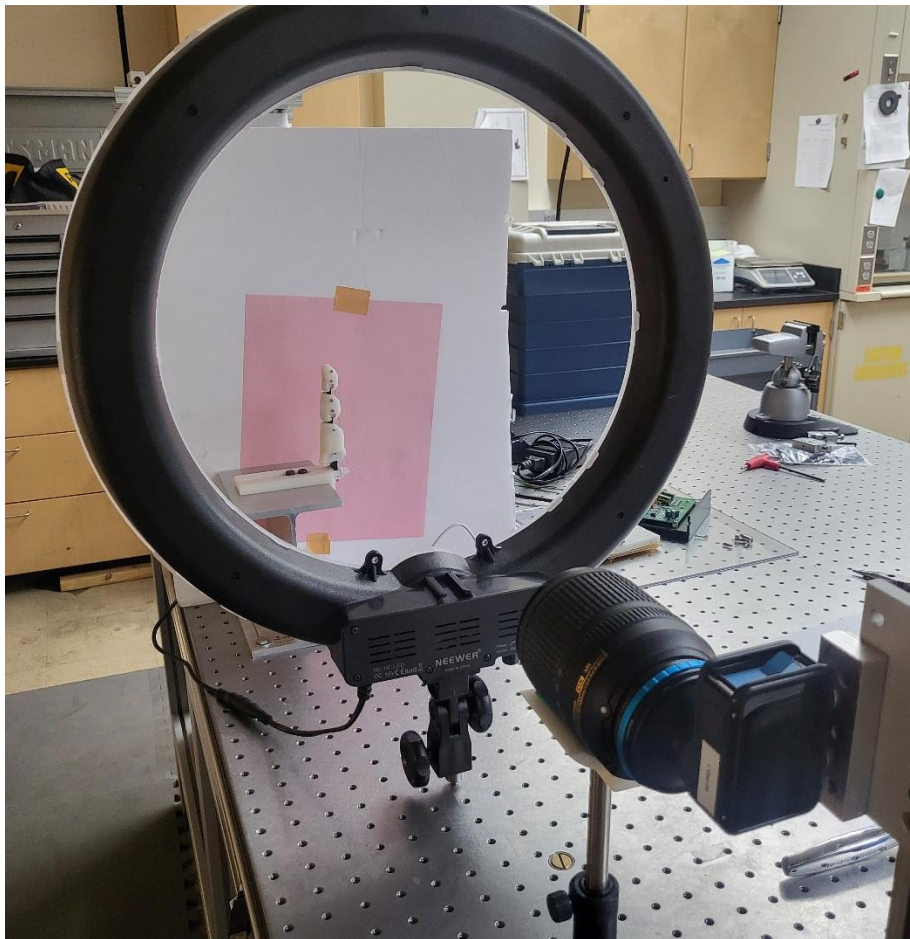


Figure 6.7: Experimental setup of 3-digit prosthetic finger experiment

6.2.3 Data processing

Images were extracted from the experimental videos corresponding to the steady state position of the finger after each load was applied. After being cropped to reduce excess data, Figure 6.8(a), the images were then converted from RGB color to gray scale, Figure 6.8(b). A binary conversion based on the intensity values of the painted markers was conducted to isolate them from the rest of the image. Any regions of the image that remained that were not associated with the markers were removed, thus fully isolating them for processing, Figure 6.8(c). The center coordinates of all seven markers were identified, Figure 6.8(d). Marker D1 was used as a (0,0) datum, and all other markers were adjusted accordingly.

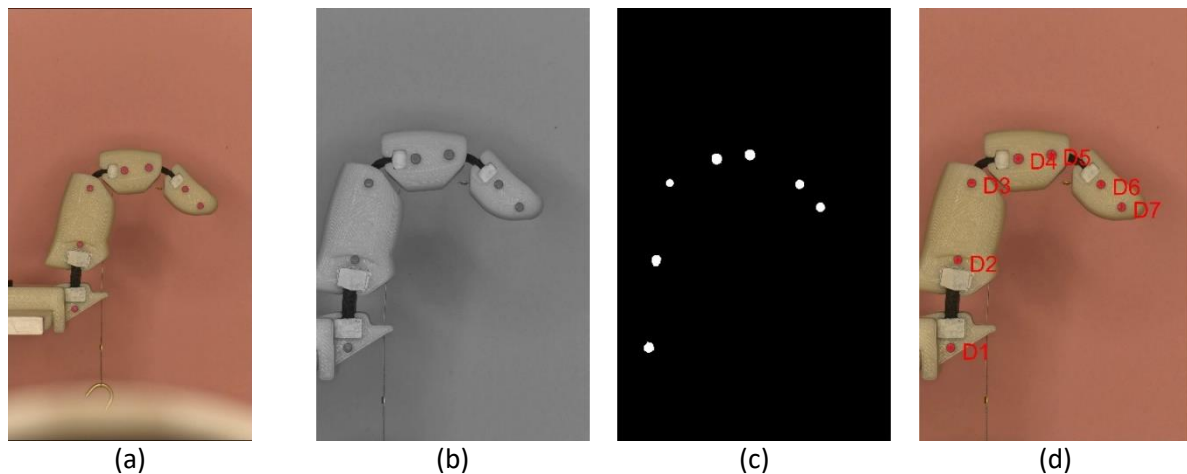


Figure 6.8: Image processing of finger flexion experiments; a) cropped image from pulled from video; b) image converted to gray scale; c) image converted to binary and markers isolated; d) markers identified in image

6.3 Results and comparison

6.3.1 Measured model parameters

To aid in comparing the model to the experimental finger, the same markers were added to the model finger, Figure 6.9. The local coordinates, Table 6.5, of the markers were transformed to global coordinates once the static solution was found for each tensile load applied.

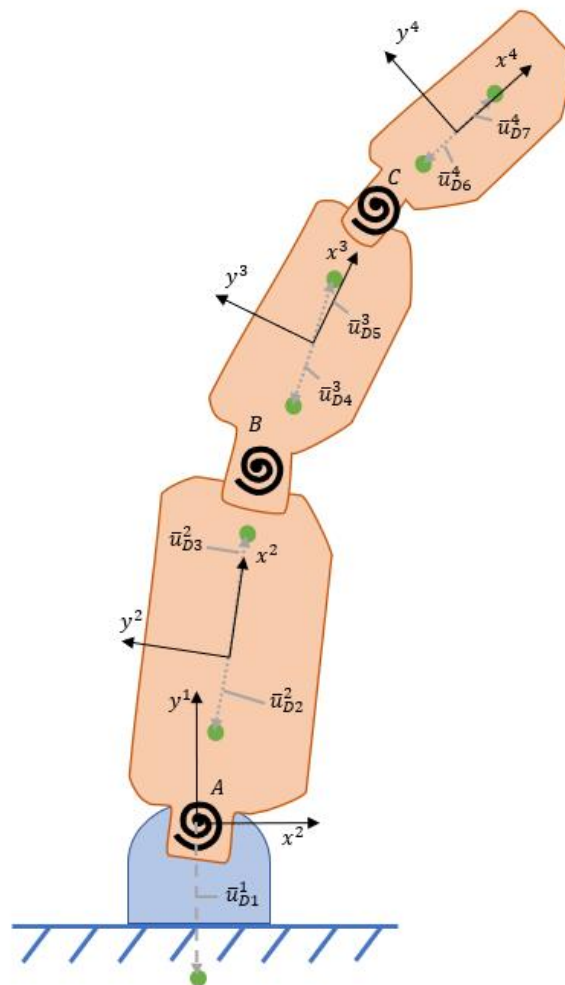


Figure 6.9: Diagram of marker locations in full finger model

The locations of the markers were calculated when the static equilibrium equations were solved, using the following example equation,

$$\begin{Bmatrix} x_{Dj} \\ y_{Dj} \end{Bmatrix} = R^i + A^i \bar{u}_{Dj}^i \quad (6.24)$$

where j is the marker number and the local coordinate vectors of the markers are defined in Table 6.5.

Table 6.5: Definition of the local coordinate vectors for each digit markers

Local Marker	Local x coordinate (mm)
$\bar{u}_{D1}^1 = [u_{D1x}^1 \ u_{D1y}^1]^T$	Location of marker D1 on Body 1, with respect to frame x^1, y^1
$\bar{u}_{D2}^2 = [u_{D2x}^2 \ u_{D2y}^2]^T$	Location of marker D2 on Body 2, with respect to frame x^2, y^2
$\bar{u}_{D3}^2 = [u_{D3x}^2 \ u_{D3y}^2]^T$	Location of marker D3 on Body 2, with respect to frame x^2, y^2
$\bar{u}_{D3}^3 = [u_{D4x}^3 \ u_{D4y}^3]^T$	Location of marker D4 on Body 3, with respect to frame x^3, y^3
$\bar{u}_{D5}^3 = [u_{D5x}^3 \ u_{D5y}^3]^T$	Location of marker D5 on Body 3, with respect to frame x^3, y^3
$\bar{u}_{D6}^4 = [u_{D6x}^4 \ u_{D6y}^4]^T$	Location of marker D6 on Body 4, with respect to frame x^4, y^4
$\bar{u}_{D7}^4 = [u_{D7x}^4 \ u_{D7y}^4]^T$	Location of marker D7 on Body 4, with respect to frame x^4, y^4

The constants used in the analytical model are defined in Table 6.6. The masses of each 3D printed digit were measured and recorded, Table 6.7. Springs were represented as nonlinear torsional springs that follow the following formula:

$$k_{Tk}(\theta) = 2a_k\theta + b_k \quad k = 1, 2, 3 \quad (6.25)$$

where, a_k and b_k are the torsional spring coefficients, which can be found in Table 6.8. An explanation of the torsional stiffness coefficient calculations is found in Appendix E. The middle and distal joints, joints B and C, were the same in the original Flexy-Hand 2 design, so it was kept the same for consistency. The spring constants for the proximal joint were significantly higher

than those of the middle and distal joints. This behavior is expected since the proximal joint is twice as thick and slightly wider than the other two.

Table 6.6: Kinematic constants used in the analytical model

Variable	Value (mm)	Variable	Value (mm)
\bar{u}_A^1	$[0, 0]^T$	u_{D1}^1	$[0, -14.5]^T$
\bar{u}_A^2	$[-24.0, -0.9]^T$	u_{D2}^2	$[-9.5, -0.9]^T$
\bar{u}_B^2	$[22.9, -0.9]^T$	u_{D3}^2	$[15.7, -0.9]^T$
\bar{u}_B^3	$[-14.7, -1.1]^T$	u_{D4}^3	$[-2.2, -1.1]^T$
\bar{u}_C^3	$[15.8, -0.1]^T$	u_{D5}^3	$[8.6, -0.1]^T$
\bar{u}_C^4	$[-14.8, -0.2]^T$	u_{D6}^4	$[-2.3, -0.2]^T$
\bar{u}_{Ap}^1	$[10.0, -7.0]^T$	u_{D7}^4	$[7.7, -0.2]^T$
\bar{u}_{Ap}^2	$[-14.6, -12.2]^T$		
\bar{u}_{Bp}^2	$[13.5, -11.1]^T$		
\bar{u}_{Bp}^3	$[-7.3, -9.2]^T$		
\bar{u}_{Cp}^3	$[8.6, -8.0]^T$		
\bar{u}_{Cp}^4	$[-9.0, -6.7]^T$		

Table 6.7: Mass of 3D printed finger digits

Digit	Mass (g)
Proximal	11.1
Middle	5.6
Distal	4.2

Table 6.8: Torsional spring coefficients used in the analytical model

Joint	$a_k \left(\frac{Nm}{rad^2} \right)$	$b_k \left(\frac{Nm}{rad} \right)$
A	-0.007	0.135
B	-0.001	0.022
C	-0.001	0.022

The neutral position of Bodies 2, 3, and 4 were defined based on the mean, unloaded position of the experimental fingers, and were used to initialize the model. The resultant finger joint angles are as follows,

$$\begin{aligned}\theta_0^2 &= 1.6 \\ \theta_0^3 &= 1.5 \\ \theta_0^4 &= 1.4\end{aligned}\tag{6.26}$$

6.3.2 Experimental results

The dimensions of the three sets of joints tested were measured and averaged, Table 6.9. The low standard deviation between specimens suggests that the joints should behave consistently across all trials.

Table 6.9: Measured dimensions and mass of experimental finger joints

Joint	l (St. Dev.) (mm)	w (St. Dev.) (mm)	t (St. Dev.) (mm)	m (St. Dev.) (g)
Nominal	10	4	15	2.80
Proximal	9.98 (0.05)	4.02 (0.01)	15.06 (0.06)	2.54 (0.01)
Nominal	10	2	12	1.12
Middle/Distal	10.05 (0.08)	2.02 (0.03)	11.90 (0.13)	0.99 (0.01)

The marker coordinates for all nine trials of the experiment were averaged and the standard deviations were found, Figure 6.9. The standard deviation error bars show that digit markers further from the fixed base point had higher deviations than those closer, as position error propagates further from the fixed point. Similarly, as the load on the tendon increased, the

deviation for respective markers increased as well. This was to be expected, as error from previous loads will compound.

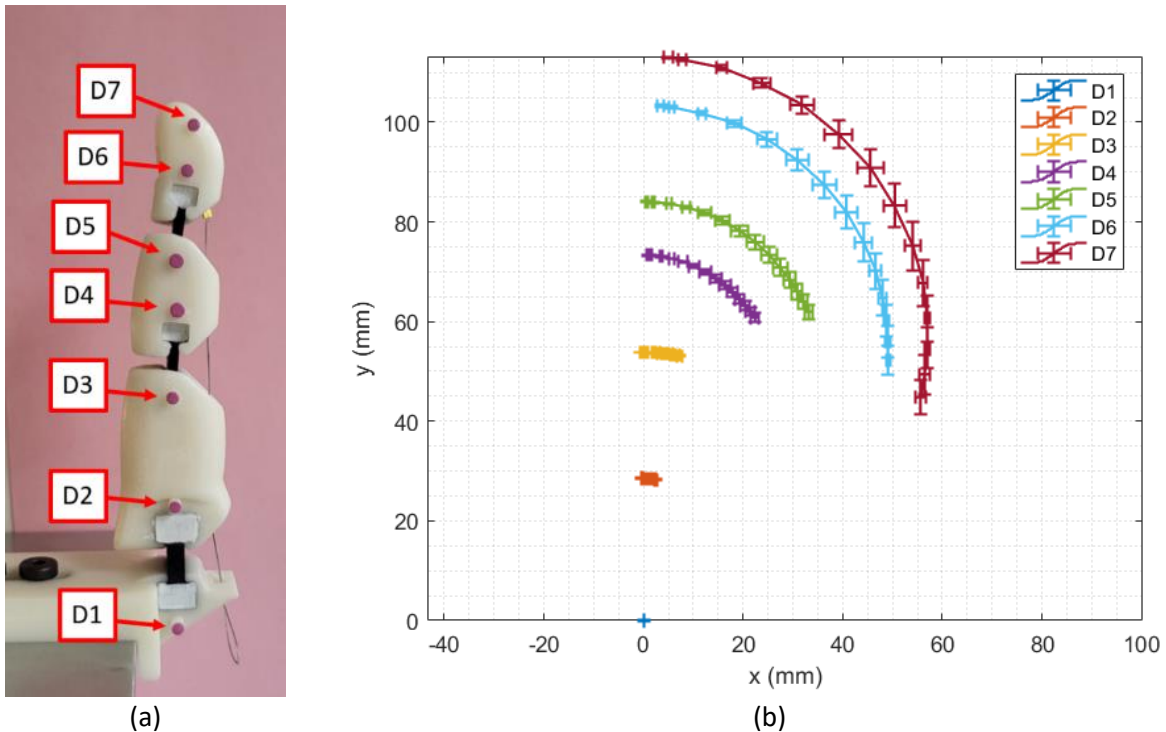


Figure 6.10: Markers for image processing flexion; a) labeled markers on finger digits; b) mean flexion results for all nine trials

The stiffness differences between finger joints were displayed as well, Figure 6.9(b). The markers on the proximal digit, D2 and D3, show little flexion under tension in comparison to the other markers.

6.3.3 Comparison of the model and experiment

The model markers on each digit were compared to the experimental coordinates for each tensile load to confirm the validity of the proposed model, Figure 6.10. As the tendon tension increased,

the difference between the markers, especially at the distal marks, became more significantly pronounced. This behavior is expected since the error compounds in the distal direction. Nevertheless, the results show that the model followed the same flexion behavior as the experimental results for all applied loads. The experimental and model flexions were compared, Figure 6.11.

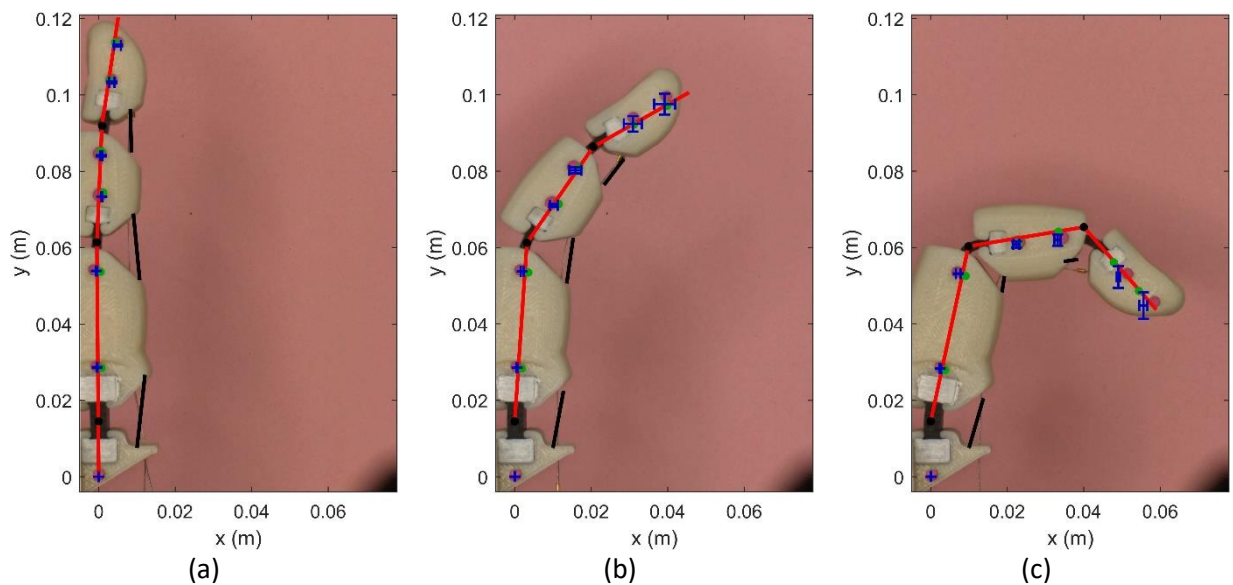


Figure 6.11: Comparison of finger model and prosthetic finger; a) unloaded initial condition; b) flexion under 1.06 N tension; c) final flexion under 2.43 N tension. The red line represents the finger digits from the model, the green dots represent the model markers, the black lines represent the model tendons, and the blue error bars represent the experimental markers.

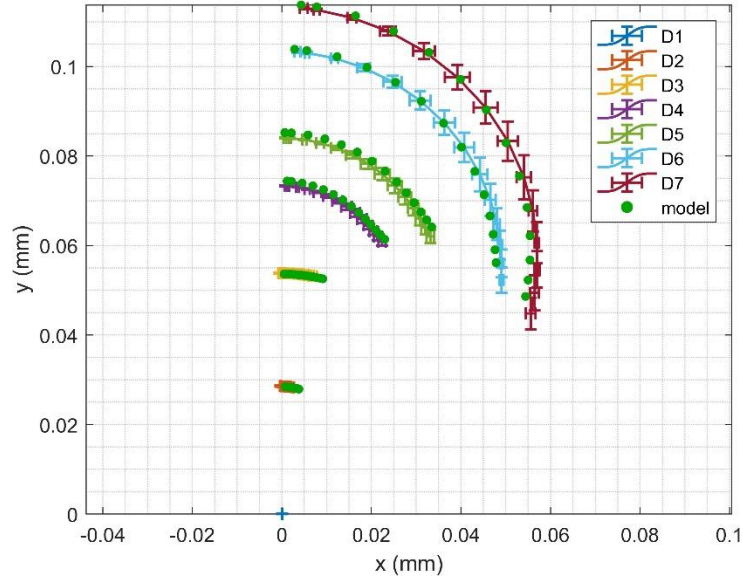


Figure 6.12: Comparison of the experimental results and the modeling marker coordinates

To quantitatively compare the validity of the model, an error function was defined, Eq. 6.27.

$$E_m = \sqrt{\frac{(x_e - x_m)^2 + (y_e - y_m)^2}{x_e^2 + y_e^2}} \quad (6.27)$$

where x and y represented the coordinates of the markers, the subscript e represented the experimental results, and m represented the model results. The error for each marker was calculated, Figure 6.11.

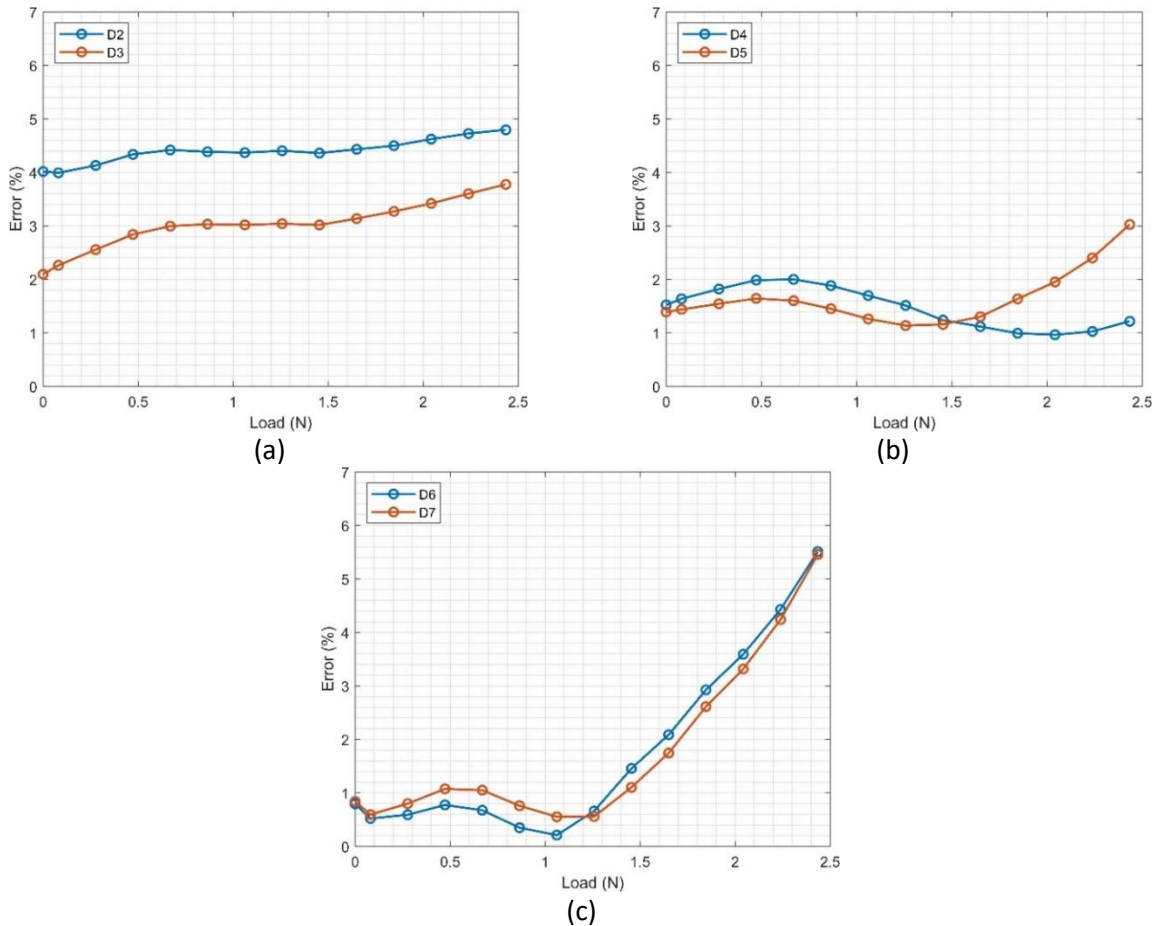


Figure 6.13: Flexion error of markers on each digit; a) body 2, proximal digit markers; b) body 3, middle digit markers; c) body 4, distal digit markers

Overall, the model was able to describe the flexion of the finger well, with errors ranging from 0.5-5.5%. The error for each digit starts very small. As the loads were increased; the error was compounded. A likely source of this was the substitution of the flexible beam behavior for torsional springs; the flexible beam experiences both extensions, as well as rotation when loaded, while the torsional spring does not allow for relative motion in the x and y direction. Despite this, our hypothesis of torsional spring substitution was proven correct, as the model error is low. Similarly, we were able to sufficiently describe the flexion behavior of the prosthetic finger with respect to tension applied to the tendon, as we hypothesized.

Chapter 7: Conclusion and future work

The need for prosthetic hands is high and will persist for the foreseeable future. Even though advancements in technology have led to incredible prosthetic developments, advanced hands require sophisticated control models and come with costs that are often unattainable. Simple, 3D printed, underactuated prostheses offer a low-cost alternative that can serve as an alternative to the high cost of modern hand prostheses. In particular, the Flexy-Hand 2 is a common option that fits these criteria. The aim of this research was to provide a comprehensive understanding of an important component of these hands: 3D printed TPU joints. This allowed for an accurate model of the flexion of a 3-digit finger in response to tendon tension.

The effect of 3D printing parameters on the mechanical characteristics of TPU components was first investigated. The extrusion temperature and filament deposition method (wall and infill) for NinjaFlex® were studied. The resulting stress-strain curves were used to determine the coefficients of the 3rd Order Mooney-Rivlin constitutive model for each experimental group. The models were then validated using FEA to confirm their accuracy and applicability. The results show that, as the extrusion temperature increases, the effect of the deposition method becomes more limited. Additionally, wall deposition leads to parts with higher elastic modulus, flexural modulus, and stress for a given strain.

The constitutive models were then used to model the behavior of the flexible joints of the Flexy-Hand 2. A relatively simple model, based on fundamental beam theory: the modified Euler–Bernoulli (MEB), for predicting the flexion of 3D printed hyperplastic components was developed. This model accounted for the large deformations and planar motion of the specimens. A finite

element analysis was also conducted to predict the bending behavior. A series of experiments were conducted on 18 different cantilever specimens with significantly different flexibilities. The results of this MEB model and FEA were compared to the experimental data, indicating that both approaches produced accurate results for most specimens. However, the MEB underestimated the overall deflection, while the FEA resulted in a significantly larger retraction of the specimens under load. MEB can sufficiently provide an accurate prediction of deformation for a large range of hyperelastic 3D printed polymer specimens and has several advantages over FEA, including simplicity and speed. MEB exhibited consistently more accurate retraction prediction, with the deflection of the tip point aligning with the experimental results; however, the deflection in the y-direction was underestimated.

A model was derived of the prosthetic finger which successfully described flexion with respect to tendon tension. Nine experimental trials were conducted, applying incrementing loads to the 3D printed finger. Overall, the tendon-actuation and nonlinear behavior of the flexible, 3D printed beam joints were accurately described, with marker coordinates having less than 5.5% error. As expected with this system prosthetic finger, the error naturally increased for digits further from the fixed support and while under increasingly larger loads. The model results show that the beam joints can be sufficiently substituted for a hinge joint with torsional springs; however, key assumptions in this substitution removed the small translations experienced by the beam joint itself, which would compound for digits further along the finger, such as the middle and distal digits.

This work presents many avenues for future work. The material characterization presented in Chapter 3 can be expanded upon by studying the many other printing parameters

that are used in 3D printing, such as the infill geometry, print speed, or layer thickness. The structure of the specimens should also be studied, investigating how gyroid or cellular specimens behave under various loads. Modeling the behavior of NinjaFlex® could be improved as well. In Chapter 5, excessive retraction in axial direction of the cantilever beam was noticed in the finite element models. This may be a result of insufficient material models for the TPU while it is under compressive loads. If the compressed underside of the bent specimens is experiencing a stiffer response than previously modeled, it may explain the gap in the x-direction.

The initial modeling efforts presented in Chapter 6 proved successful at predicting finger flexion under tendon tension; the next steps include modeling the interaction of objects with the prosthetic finger to study the grip strength of the prosthetic. Then, optimization of the Flexy-Hand 2 design can be conducted. There are many improvements that can be made to the prosthesis, however the most common complaints from users concern the grip/grasping ability, [77]. Therefore, the goal of optimization should be to improve the grip strength of the 3D printed Flexy-Hand 2. The parameters to be optimized are the physical dimensions of the prosthetic hand, namely the joint sizes and joint locations. Similarly, the limitations of the user are also considered, such as wrist joint flexion strength and range of motion. To confirm the results of the optimized hand prosthesis, the grip force will need to be compared to the original hand design through a series of experiments by applying tensile loads to the tendons and compare the grasping strength between the two. Successful optimization would allow for user specific designs to be created to best suit individual needs and abilities.

Appendix A: Mooney-Rivlin constitutive model derivation

The following text derives the stress strain relationship of the Mooney-Rivlin material model. To begin, the directions in the Cartesian coordinates are defined:

$$\begin{aligned}\xi &= x + u \\ \eta &= y + v \\ \zeta &= z + w\end{aligned}\tag{A.1}$$

Where $\xi, \eta,$ and ζ represent the deformed position of an elementary unit from the original coordinates $x, y,$ and z with deflections $u, v,$ and $w,$ respectively.

Fundamentally, it is known that the strain energy of a system, $W,$ is,

$$\begin{aligned}W &= \int \sigma d\varepsilon \\ \partial W &= \sigma d\varepsilon \\ \frac{dW}{d\varepsilon} &= \sigma\end{aligned}\tag{A.2}$$

Therefore, the stress acting on a unit element is equivalent to the change in strain energy with respect to the change in strain. To start, the forces acting on the faces of the elementary unit are defined as,

$$\begin{aligned}t_{xx}\Delta\eta\Delta\zeta + t_{xy}\Delta\zeta\Delta\xi + t_{xz}\Delta\xi\Delta\eta \\ t_{yx}\Delta\eta\Delta\zeta + t_{yy}\Delta\zeta\Delta\xi + t_{yz}\Delta\xi\Delta\eta \\ t_{zx}\Delta\eta\Delta\zeta + t_{zy}\Delta\zeta\Delta\xi + t_{zz}\Delta\xi\Delta\eta\end{aligned}\tag{A.3}$$

Next, the total virtual work done in the relative displacements $\delta(\Delta u), \delta(\Delta v),$ and $\delta(\Delta w):$

$$\begin{aligned}\delta W_{virt} &= (t_{xx}\Delta\eta\Delta\zeta + t_{xy}\Delta\zeta\Delta\xi + t_{xz}\Delta\xi\Delta\eta)\delta(\Delta u) \\ &+ (t_{yx}\Delta\eta\Delta\zeta + t_{yy}\Delta\zeta\Delta\xi + t_{yz}\Delta\xi\Delta\eta)\delta(\Delta v) \\ &+ (t_{zx}\Delta\eta\Delta\zeta + t_{zy}\Delta\zeta\Delta\xi + t_{zz}\Delta\xi\Delta\eta)\delta(\Delta w)\end{aligned}\tag{A.4}$$

Now the partial differential of the stored strain energy, $W,$ is

$$\delta W = \frac{\partial W}{\partial u_\xi} \frac{\partial(\Delta u)}{\Delta \xi} + \frac{\partial W}{\partial u_\eta} \frac{\partial(\Delta u)}{\Delta \eta} + \frac{\partial W}{\partial u_\zeta} \frac{\partial(\Delta u)}{\Delta \zeta} + \frac{\partial W}{\partial v_\xi} \frac{\partial(\Delta v)}{\Delta \xi} + \frac{\partial W}{\partial v_\eta} \frac{\partial(\Delta v)}{\Delta \eta} + \frac{\partial W}{\partial v_\zeta} \frac{\partial(\Delta v)}{\Delta \zeta} + \frac{\partial W}{\partial w_\xi} \frac{\partial(\Delta w)}{\Delta \xi} + \frac{\partial W}{\partial w_\eta} \frac{\partial(\Delta w)}{\Delta \eta} + \frac{\partial W}{\partial w_\zeta} \frac{\partial(\Delta w)}{\Delta \zeta} \quad (A.5)$$

Where $\frac{\partial W}{\partial u_\xi}$ is equivalent to $\frac{\lim_{\delta u \rightarrow 0} \delta W}{\frac{\Delta(\delta u)}{\Delta \xi}}$, and so on.

It should be noted that the stored energy per unit volume is equivalent to the virtual work done per unit volume,

$$\delta W \Delta x \Delta y \Delta z = \delta W_{virt} \quad (A.6)$$

Therefore,

$$\begin{aligned} t_{xx} &= \frac{1}{\tau} \frac{\partial W}{\partial u_\xi} & t_{xy} &= \frac{1}{\tau} \frac{\partial W}{\partial u_\eta} & t_{xz} &= \frac{1}{\tau} \frac{\partial W}{\partial u_\zeta} \\ t_{yx} &= \frac{1}{\tau} \frac{\partial W}{\partial v_\xi} & t_{yy} &= \frac{1}{\tau} \frac{\partial W}{\partial v_\eta} & t_{yz} &= \frac{1}{\tau} \frac{\partial W}{\partial v_\zeta} \\ t_{zx} &= \frac{1}{\tau} \frac{\partial W}{\partial w_\xi} & t_{zy} &= \frac{1}{\tau} \frac{\partial W}{\partial w_\eta} & t_{zz} &= \frac{1}{\tau} \frac{\partial W}{\partial w_\zeta} \end{aligned} \quad (A.7)$$

Since this work is concerned with the uniaxial relationship of NinjaFlex[®], the first stress, t_{xx} , will be analyzed,

$$t_{xx} = \frac{1}{\tau} \lim_{\substack{\delta u \rightarrow 0 \\ \Delta \xi \rightarrow 0}} \frac{\delta W}{\frac{\Delta(\delta u)}{\Delta \xi}} \quad (A.8)$$

If $\xi = x + u$, then

$$\Delta \xi = (1 + u_x) \Delta x + u_y \Delta y + u_z \Delta z \quad (A.9)$$

Therefore,

$$t_{xx} = \frac{1}{\tau} \lim_{\substack{\delta u \rightarrow 0 \\ \Delta x, \Delta y, \Delta z \rightarrow 0}} \frac{\delta W}{\Delta(\delta u)} [(1 + u_x) \Delta x + u_y \Delta y + u_z \Delta z] \quad (A.10)$$

Or,

$$t_{xx} = \frac{1}{\tau} \left[(1 + u_x) \frac{\partial W}{\partial u_x} + u_y \frac{\partial W}{\partial u_y} + u_z \frac{\partial W}{\partial u_z} \right] \quad (A.11)$$

When the material of the elementary unit is considered isotropic, the stored energy W is a symmetric function of the stretches λ_1, λ_2 , and λ_3 , which in turn is a function of λ_1^2, λ_2^2 , and λ_3^2 .

Therefore, the stored energy, W , can be defined as a function of the strain invariants,

$$W = W(I_1, I_2, I_3) \quad (A.12)$$

Applying this to the strain equation,

$$t_{xx} = \frac{1}{\tau} \left[\begin{array}{l} (1 + u_x) \left(\frac{\partial W}{\partial I_1} \frac{\partial I_1}{\partial u_x} + \frac{\partial W}{\partial I_2} \frac{\partial I_2}{\partial u_x} + \frac{\partial W}{\partial I_3} \frac{\partial I_3}{\partial u_x} \right) + \\ u_y \left(\frac{\partial W}{\partial I_1} \frac{\partial I_1}{\partial u_y} + \frac{\partial W}{\partial I_2} \frac{\partial I_2}{\partial u_y} + \frac{\partial W}{\partial I_3} \frac{\partial I_3}{\partial u_y} \right) + \\ u_z \left(\frac{\partial W}{\partial I_1} \frac{\partial I_1}{\partial u_z} + \frac{\partial W}{\partial I_2} \frac{\partial I_2}{\partial u_z} + \frac{\partial W}{\partial I_3} \frac{\partial I_3}{\partial u_z} \right) \end{array} \right] \quad (A.13)$$

Or,

$$\begin{aligned} t_{xx} = \frac{1}{\tau} & \left[(1 + u_x) \frac{\partial I_1}{\partial u_x} + u_y \frac{\partial I_1}{\partial u_y} + u_z \frac{\partial I_1}{\partial u_z} \right] \frac{\partial W}{\partial I_1} + \\ & \frac{1}{\tau} \left[(1 + u_x) \frac{\partial I_2}{\partial u_x} + u_y \frac{\partial I_2}{\partial u_y} + u_z \frac{\partial I_2}{\partial u_z} \right] \frac{\partial W}{\partial I_2} + \\ & \frac{1}{\tau} \left[(1 + u_x) \frac{\partial I_3}{\partial u_x} + u_y \frac{\partial I_3}{\partial u_y} + u_z \frac{\partial I_3}{\partial u_z} \right] \frac{\partial W}{\partial I_3} \end{aligned} \quad (A.14)$$

This can be reduced further with the following strain functions:

$$\begin{aligned} \varepsilon_{xx} &= u_x + \frac{1}{2}(u_x^2 + v_x^2 + w_x^2) \\ \varepsilon_{yy} &= v_y + \frac{1}{2}(u_y^2 + v_y^2 + w_y^2) \\ \varepsilon_{zz} &= w_z + \frac{1}{2}(u_z^2 + v_z^2 + w_z^2) \end{aligned} \quad (A.15)$$

Similarly with the strain invariants,

$$I_1 = 3 + 2(\varepsilon_{xx} + \varepsilon_{yy} + \varepsilon_{zz}) \quad (A.16)$$

$$I_2 = (1 + 2\varepsilon_{yy})(1 + 2\varepsilon_{zz}) + (1 + 2\varepsilon_{zz})(1 + 2\varepsilon_{xx}) \\ + (1 + 2\varepsilon_{xx})(1 + 2\varepsilon_{yy}) - \varepsilon_{yz}^2 - \varepsilon_{zx}^2 - \varepsilon_{xy}^2 \quad (A.17)$$

$$I_3 = (1 + 2\varepsilon_{xx})(1 + 2\varepsilon_{yy})(1 + 2\varepsilon_{zz}) + 2\varepsilon_{yz}\varepsilon_{zx}\varepsilon_{xy} \\ - (1 + 2\varepsilon_{xx})\varepsilon_{yz}^2 - (1 + 2\varepsilon_{yy})\varepsilon_{zx}^2 - (1 + 2\varepsilon_{zz})\varepsilon_{xy}^2 \quad (A.18)$$

Leading to

$$t_{xx} = \frac{2}{\tau} \left[(1 + 2\varepsilon_{xx}) \frac{\partial W}{\partial I_1} - (1 - 2\varepsilon_{\xi\xi}) I_3 \frac{\partial W}{\partial I_2} + \left(I_3 \frac{\partial W}{\partial I_3} + I_2 \frac{\partial W}{\partial I_2} \right) \right] \quad (A.19)$$

It is known that,

$$\lambda_1 = 1 + \varepsilon_x \\ \lambda_2 = 1 + \varepsilon_y \\ \lambda_3 = 1 + \varepsilon_z \quad (A.20)$$

When $\lambda_1, \lambda_2,$ and λ_3 are parallel to the x, y, and z axes respectively. This leads to the relations:

$$u = (\lambda_1 - 1)x \\ v = (\lambda_2 - 1)y \\ w = (\lambda_3 - 1)z \quad (A.21)$$

Applying this to the stress equation yields

$$t_{xx} = \frac{2}{\tau} \left[\lambda_1^2 \frac{\partial W}{\partial I_1} - \frac{I_3}{\lambda_1^2} \frac{\partial W}{\partial I_2} + I_3 \frac{\partial W}{\partial I_3} + I_2 \frac{\partial W}{\partial I_2} \right] \quad (A.22)$$

This stress equation represents the stress in the principle x direction for a compressible material. It can be reduced further based on uniaxial extension and incompressible assumption used with the TPU filament. When the material is only distorted under a uniaxial load, the stretches are reduced to

$$\begin{aligned}\lambda_1 &= \lambda \\ \lambda_2 &= \frac{1}{\sqrt{\lambda}} \\ \lambda_3 &= \frac{1}{\sqrt{\lambda}}\end{aligned}\tag{A.23}$$

From

$$\lambda_1 \lambda_2 \lambda_3 = 1\tag{A.24}$$

Next, under the incompressible assumption,

$$\begin{aligned}\tau &= 1 \\ I_3 &= 1 \text{ (Identity)}\end{aligned}$$

The stress in the uniaxial direction, in this case t_{xx} , becomes

$$t_{xx} = 2 \left(\lambda^2 - \frac{1}{\lambda} \right) \left(\frac{\partial W}{\partial I_1} + \frac{1}{\lambda} \frac{\partial W}{\partial I_2} \right)\tag{A.25}$$

To calculate the stress for the given system, the strain energy equation must be defined. Mooney proposes the following strain energy equation, [58,78]:

$$W = \sum_{p,q=0}^N C_{p,q} (\bar{I}_1 - 3)^p (\bar{I}_2 - 3)^q\tag{A.26}$$

Where N can equal infinity, however, it is sufficiently accurate at $N = 1$ for most materials. $C_{p,q}$ are the coefficients of the material model, and \bar{I}_1 and \bar{I}_2 are the invariants of the left Cauchy-Green tensor, or

$$\bar{I}_1 = J^{-\frac{2}{3}} I_1\tag{A.27}$$

$$\bar{I}_2 = J^{-\frac{4}{3}} I_2\tag{A.28}$$

If the material is considered incompressible, then $J = 1$. Expanded, the strain energy equation, expanded to the third order, becomes:

$$W = C_{10}(I_1 - 3) + C_{01}(I_2 - 3) + C_{11}(I_1 - 3)(I_2 - 3) \quad (\text{A. 29})$$

Now the derivatives of the strain energy are found to apply to the stress equation,

$$\frac{\partial W}{\partial I_1} = \frac{\partial}{\partial I_1} (C_{10}(I_1 - 3) + C_{01}(I_2 - 3) + C_{11}(I_1 - 3)(I_2 - 3)) \quad (\text{A. 30})$$

$$\frac{\partial W}{\partial I_1} = C_{10} + C_{11}(I_2 - 3) \quad (\text{A. 31})$$

$$\frac{\partial W}{\partial I_1} = C_{10} + C_{11} \left(2\lambda + \frac{1}{\lambda^2} - 3 \right) \quad (\text{A. 32})$$

Next, the second invariant derivative,

$$\frac{\partial W}{\partial I_2} = \frac{\partial}{\partial I_2} (C_{10}(I_1 - 3) + C_{01}(I_2 - 3) + C_{11}(I_1 - 3)(I_2 - 3)) \quad (\text{A. 33})$$

$$\frac{\partial \omega}{\partial I_2} = C_{01} + C_{11}(I_1 - 3) \quad (\text{A. 34})$$

$$\frac{\partial \omega}{\partial I_2} = C_{01} + C_{11} \left(\lambda^2 + \frac{2}{\lambda} - 3 \right) \quad (\text{A. 35})$$

Plugging the derivatives into the stress equation,

$$t_{xx} = 2 \left(\lambda^2 - \frac{1}{\lambda} \right) \left(\left(C_{10} + C_{11} \left(2\lambda + \frac{1}{\lambda^2} - 3 \right) \right) + \frac{1}{\lambda} \left(C_{01} + C_{11} \left(\lambda^2 + \frac{2}{\lambda} - 3 \right) \right) \right) \quad (\text{A. 36})$$

This equation describes true stress as a function of stretch, λ , which is equivalent to $1 + \varepsilon$, where ε is strain. To convert to engineering stress, simply,

$$\sigma_{ENG} = \frac{t_{xx}}{1 + \varepsilon} \quad (\text{A. 37})$$

Appendix B: Derivation of modified Euler-Bernoulli (MEB) method for flexible joints

The following text derives the relationship between applied loads on a flexible joint and the resulting deflection in the x and y direction, Figure B.1. The system contains a fixed cantilever beam with a rigid bracket attached to the free end for applying the loads.

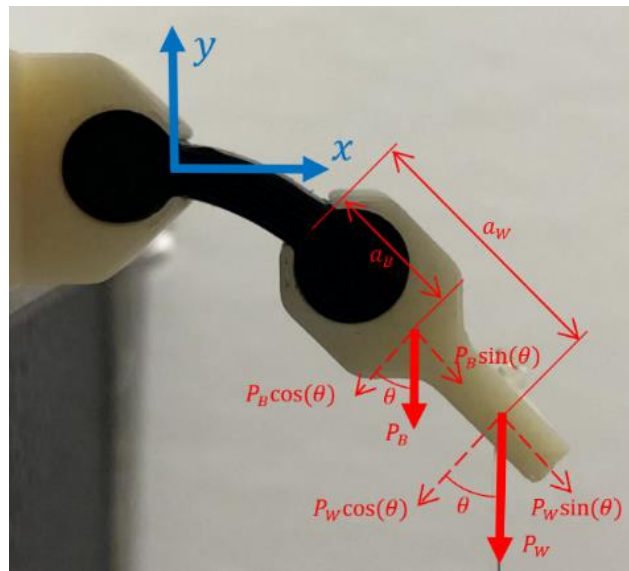


Figure B.1: Diagram of loads on flexible joints

The system in question can be simplified to a combined load and moment about the end of the beam, due to the rigidity of the free end bracket, Fig. B.2. The point loads can be combined, along with the respective moments.

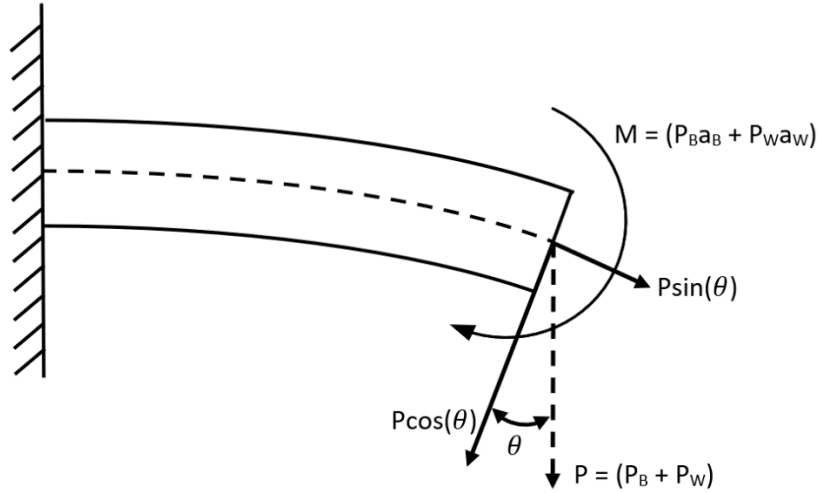


Figure B.2: Simplified system diagram

The system variables seen in Figure B.1 and B.2 are summarized in Table B.1 with the related units.

Table B.1: Variables of MEB method

Variable:	Represents:	Units:
l	Free Length	m
a_B	Moment Arm of Bracket Weight	m
a_W	Moment Arm of Applied Weight	m
P_B	Load Applied by Bracket Weight	N
P_W	Load Applied by Applied Weight	N
θ	Angle/Slope of the Free End	Rad
M	Combined Moment of all Applied Loads	Nm
P	Combined Load of all Applied Loads	N

To calculate the static equilibrium of the beam joint under the point load, the variations in virtual work are done by the external loads and the strain energies of the beam joint,

$$\delta W - \delta U_A - \delta U_B = 0 \quad (B.1)$$

where W is the virtual work, U_A is the axial strain energy, and U_B is the bending strain energy.

First, the work done on the system is defined as:

$$\begin{aligned}
 W = & (P_W + P_B)\sin(\theta(l))u(l) + \\
 & (P_W + P_B)\cos(\theta(l))v(l) + \\
 & (P_W a_W + P_B a_B)\cos(\theta(l))\theta(l)
 \end{aligned} \tag{B.2}$$

where P_W is the load from the applied weight, P_B is the load from the bracket weight, θ is the angle between the plane cross-section and the vertical axis, u is displacement in the x-direction of the beam, v is displacement in the y-direction of the beam, a_W is the moment arm from the applied weight on the free bracket to the free end of the beam, and a_B is the moment arm from the center of mass of the bracket to the free end of the beam.

Simplifying,

$$W = P \left(\sin(\theta(l))u(l) + \cos(\theta(l))v(l) \right) + M \cos(\theta(l))\theta(l) \tag{B.3}$$

where the total applied load is $P = P_W + P_B$ and the total applied moment is $M = P_W a_W + P_B a_B$.

It should be noted that the slope of the tip point is related to the deflection derivative using the following equation:

$$\theta(l) = \tan^{-1}(v_x(l)) \tag{B.4}$$

Next, the strain energy equations for both the axial and bending strain are defined, respectively, as:

$$U_A = \frac{1}{2}EA \int_0^l u_x^2 dx \quad (B.5)$$

$$U_B = \frac{1}{2}EI \int_0^l v_{xx}^2 dx \quad (B.6)$$

where E is the modulus of elasticity, A is the rectangular cross-sectional area, and I is the area moment of inertia of the rectangular cross-section. A and I are defined as:

$$A = wh \quad (B.7)$$

$$I = \frac{1}{12}wh^3 \quad (B.8)$$

Arbitrary virtual displacements were now applied to the work done by the external loading,

$$\begin{aligned} W &= P \left(\sin(\theta(l))u(l) + \cos(\theta(l))v(l) \right) + M \cos(\theta(l))\theta(l) \\ \delta W &= P \left(\begin{aligned} &\cos(\theta(l)) \left(\frac{1}{1+v_x^2(l)} \right) u(l) \delta v_x(l) + \sin(\theta(l)) \delta u(l) \\ &-\sin(\theta(l)) \left(\frac{1}{1+v_x^2(l)} \right) v(l) \delta v_x(l) + \cos(\theta(l)) \delta v(l) \end{aligned} \right) \\ &\quad + M \left(\begin{aligned} &-\sin(\theta(l)) \left(\frac{1}{1+v_x^2(l)} \right) \theta(l) \delta v_x(l) \\ &+ \cos(\theta(l)) \left(\frac{1}{1+v_x^2(l)} \right) \delta v_x(l) \end{aligned} \right) \end{aligned} \quad (B.9)$$

Eqn. (B.9) can be written with respect to the virtual variables,

$$\begin{aligned}
& \delta W = P \cos(\theta(L)) \delta v(L) \\
& + \left(\begin{aligned} & P \left(\cos(\theta(L)) \left(\frac{1}{1+v_x^2(L)} \right) u(L) - \sin(\theta(L)) \left(\frac{1}{1+v_x^2(L)} \right) v(L) \right) \\ & + M \left(-\sin(\theta(L)) \left(\frac{1}{1+v_x^2(L)} \right) \theta(L) + \cos(\theta(L)) \left(\frac{1}{1+v_x^2(L)} \right) \delta v_x(L) \right) \end{aligned} \right) \delta v_x(L) \\
& + P \sin(\theta(L)) \delta u(L)
\end{aligned} \tag{B.10}$$

Next, we can reduce the virtual work of the axial extension, Eqn. (B.5), via integration by parts,

or,

$$\begin{aligned}
U_A &= \frac{1}{2} EA \int_0^l u_x^2 dx \\
U_A &= EA \int_0^l u_x \delta u_x dx \\
\delta U_A &= EA \left(u_x \delta u \Big|_0^L - \int_0^L u_{xx} \delta u dx \right)
\end{aligned} \tag{B.11}$$

Expanding,

$$\delta U_A = EA \left(u_x(L) \delta u(L) - u_x(0) \delta u(0) - \int_0^L u_{xx} \delta u dx \right) \tag{B.12}$$

Next, the strain energy from bending the joint is expanded by applying virtual strain energy to

Eqn. (B.6),

$$\begin{aligned}
U_B &= \frac{1}{2} EI \int_0^L v_{xx}^2 dx \\
\delta U_B &= EI \int_0^L v_{xx} \delta v_{xx} dx
\end{aligned} \tag{B.13}$$

Now we can expand Eqn. (B.10) with integration by parts,

$$\delta U_B = EI \left(v_{xx} \delta v_x \Big|_0^L - v_{xxx} \delta v \Big|_0^L + \int_0^L v_{xxxx} \delta v dx \right) \tag{B.14}$$

Expanding,

$$\delta U_B = EI \left(v_{xx}(L)\delta v_x(L) - v_{xx}(0)\delta v_x(0) - v_{xxx}(L)\delta v(L) + v_{xxx}(0)\delta v(0) + \int_0^L v_{xxxx}\delta v dx \right) \quad (B.15)$$

Based on the displacement boundary conditions,

$$v_x(0) = v(0) = u(0) = 0$$

Therefore,

$$\delta v_x(0) = \delta v(0) = \delta u(0) = 0$$

Applying the displacement boundary conditions to Eqn. (B.12) and (B.15),

$$\begin{aligned} \delta U_A &= EA \left(u_x(L)\delta u(L) - u_x(0)\delta u(0) - \int_0^L u_{xx}\delta u dx \right) \\ \delta U_A &= EA \left(u_x(L)\delta u(L) - \int_0^L u_{xx}\delta u dx \right) \end{aligned} \quad (B.16)$$

$$\begin{aligned} \delta U_B &= EI \left(v_{xx}(L)\delta v_x(L) - v_{xx}(0)\delta v_x(0) - v_{xxx}(L)\delta v(L) + v_{xxx}(0)\delta v(0) + \int_0^L v_{xxxx}\delta v dx \right) \\ \delta U_B &= EI \left(v_{xx}(L)\delta v_x(L) - v_{xxx}(L)\delta v(L) + \int_0^L v_{xxxx}\delta v dx \right) \end{aligned} \quad (B.17)$$

Now, the integrals of Eqn. (B.16) and (B.17) can be expanded. Solving the two differential equations,

$$\begin{aligned} u_{xx} &= 0 \\ u_x &= D \\ u &= Dx + S \end{aligned} \quad (B.18)$$

Where $u(0) = 0$, therefore,

$$u(x) = Dx$$

Next,

$$\begin{aligned}v_{xxxx} &= 0 \\v_{xxx} &= B \\v_{xx} &= Bx + C \\v_x &= \frac{1}{2}Bx^2 + Cx + G \\v &= \frac{1}{6}Bx^3 + \frac{1}{2}Cx^2 + Gx + H\end{aligned}\tag{B.19}$$

Applying the displacement boundary conditions, $v(0) = 0$, $v_x(0) = 0$,

$$\begin{aligned}v_x(0) = 0 &= \frac{1}{2}B(0)^2 + C(0) + G \\0 &= G\end{aligned}\tag{B.20}$$

$$\begin{aligned}v(0) = 0 &= \frac{1}{6}B(0)^3 + \frac{1}{2}C(0)^2 + H \\0 &= H\end{aligned}\tag{B.21}$$

Therefore,

$$v(x) = \frac{1}{6}Bx^3 + \frac{1}{2}Cx^2\tag{B.22}$$

From Eqn. (B.1),

$$\delta W = \delta U_A + \delta U_B\tag{B.23}$$

The force boundary conditions can be applied to the strain energy equations,

$$P\cos(\theta(l)) = -EIv_{xxx}(l) \quad (B.24)$$

$$\begin{aligned} & -P\sin(\theta(l))\left(\frac{1}{1+v_x^2(l)}\right)v(l) - M\sin(\theta(l))\left(\frac{1}{1+v_x^2(l)}\right)\theta(l) \\ & + M\cos(\theta(l))\left(\frac{1}{1+v_x^2(l)}\right) + P\cos(\theta(l))\left(\frac{1}{1+v_x^2(l)}\right)u(l) = EIv_{xx}(l) \end{aligned} \quad (B.25)$$

$$P\sin(\theta(l)) = EAU_x(l) \quad (B.26)$$

Or,

$$P\cos(\theta(l)) = -EIv_{xxx}(l) \quad (B.27)$$

$$\left(\frac{1}{1+v_x^2(l)}\right)\left((Pu(l) + M)\cos(\theta(l)) - (Pv(l) + M\theta(l))\sin(\theta(l))\right) = EIv_{xx}(l) \quad (B.28)$$

$$P\sin(\theta(l)) = EAU_x(l) \quad (B.29)$$

In order to solve the deflection equations completely, the coefficients A, B, and H need to be found. Starting with Eqn. (B.29),

$$P\sin(v_x(L)) = EAU_x(L)$$

Or,

$$\frac{P}{EA}\sin(v_x(L)) = u_x(L) \quad (B.30)$$

Substituting the solution from Eqn. (B.18)

$$u_x(L) = D = \frac{P}{EA} \sin(v_x(L)) \quad (B.31)$$

Next, we can solve for A and B. Starting with Equation. (B.27),

$$P \cos(\theta(l)) = -EI v_{xxx}(l)$$

Therefore,

$$v_{xxx}(L) = B = -\frac{P}{EI} \cos(\theta(l)) \quad (B.32)$$

Add a sentence describing what you are going to do

$$\left(\frac{1}{1 + v_x^2(l)} \right) \left((Pu(l) + M) \cos(\theta(l)) - (Pv(l) + M\theta(l)) \sin(\theta(l)) \right) = EI v_{xx}(L)$$

Or,

$$\frac{1}{EI} \left(\left(\frac{1}{1 + v_x^2(l)} \right) \left((Pu(l) + M) \cos(\theta(l)) - (Pv(l) + M\theta(l)) \sin(\theta(l)) \right) \right) = BL + C \quad (B.33)$$

Where we can substitute B from Eqn. (B.32),

$$C = \frac{1}{EI} \left(\left(\frac{1}{1 + v_x^2(l)} \right) \left((Pu(l) + M) \cos(\theta(l)) - (Pv(l) + M\theta(l)) \sin(\theta(l)) \right) \right) + \frac{PL}{EI} \cos(\theta(L))$$

Or

$$C = \frac{\left((Pu(l) + M) \cos(\theta(l)) - (Pv(l) + M\theta(l)) \sin(\theta(l)) \right) + PL \cos(\theta(l))}{EI(1 + v_x^2(l))}$$

We now have three equations for the three unknown coefficients B, C, and D.

$$B = -\frac{P}{EI} \cos(\theta(l)) \quad (B.34)$$

$$C = \frac{\left((Pu(l) + M) \cos(\theta(l)) - (Pv(l) + M\theta(l)) \sin(\theta(l)) \right) + PL \cos(\theta(l))}{EI(1 + v_x^2(l))} \quad (B.35)$$

$$D = \frac{P}{EA} \sin(\theta(l)) \quad (B.36)$$

These three nonlinear algebraic equations should be solved simultaneously. Now, using any preferred method, the coefficients can be found and plugged into the following for the deflection equations. Now to solve for the unknown coefficients B, C, and D.

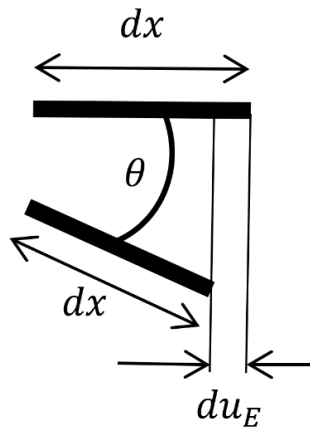


Figure B.3: Differential unit for retraction calculation

These deflection equations only described bending and axial deflection. They do not, however, account for the retraction along the x direction that is typically associated with large

deformation, [68]. Based on Figure B.2, the differential retraction, du_E , of the beam can be expressed as:

$$du_E = dx(1 - \cos(\theta)) = dx \left(2\sin^2 \left(\frac{\theta}{2} \right) \right) \quad (B.37)$$

The angle, θ , of the beam can be substituted with Eqn. (B.3). By integrating this equation, the retraction of the tip point, u_E , can be obtained:

$$u_E = - \int_0^l \left(2\sin^2 \left(\frac{\tan^{-1}(v_x)}{2} \right) \right) dx \quad (B.38)$$

The equation for v_x from Eqn. (B.19) can be applied, and the tip point retraction equation becomes:

$$u_E = - \int_0^l \left(2\sin^2 \left(\frac{\tan^{-1} \left(\frac{1}{2} Bx^2 + Cx \right)}{2} \right) \right) dx \quad (B.39)$$

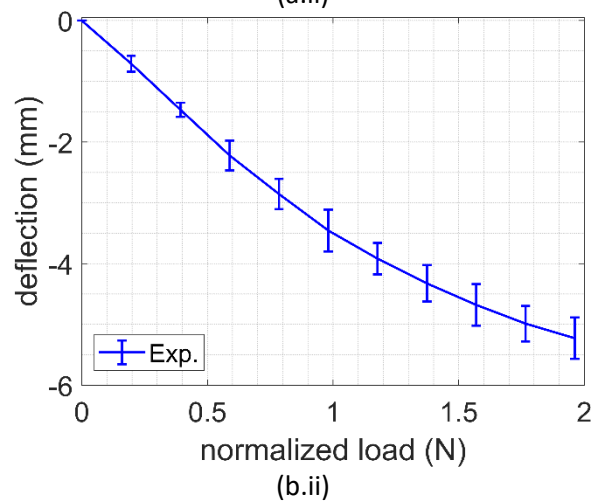
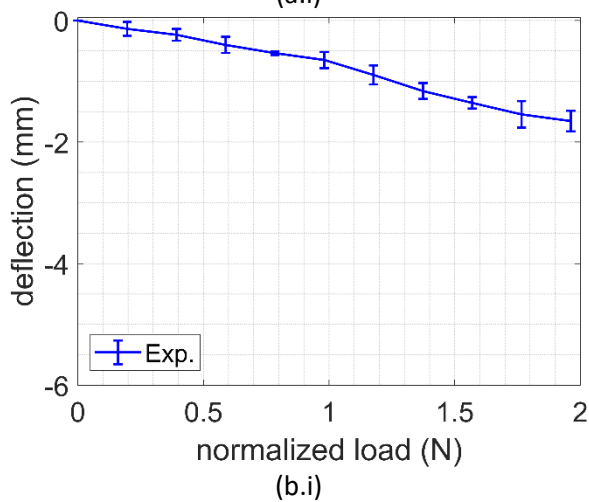
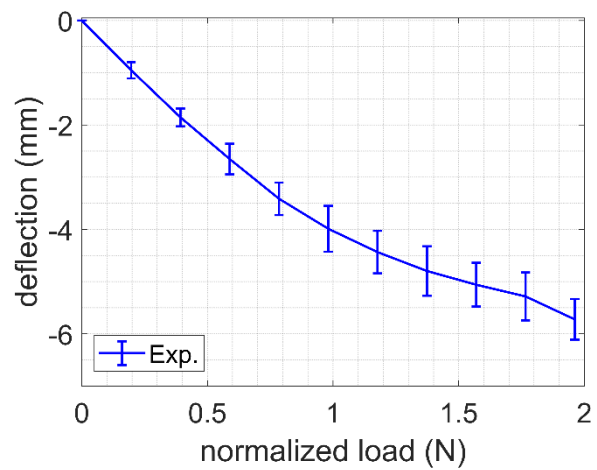
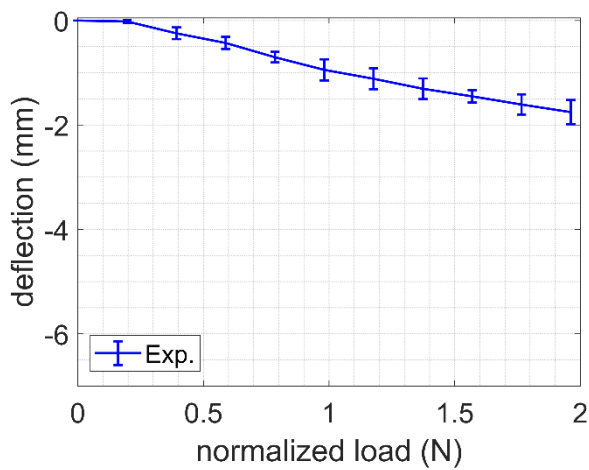
The total deformation of the tip point can be expressed as a combination of this retraction in addition to the extension caused by the axial portion of the applied loads, $(P_W + P_B)\sin(\theta(l))$:

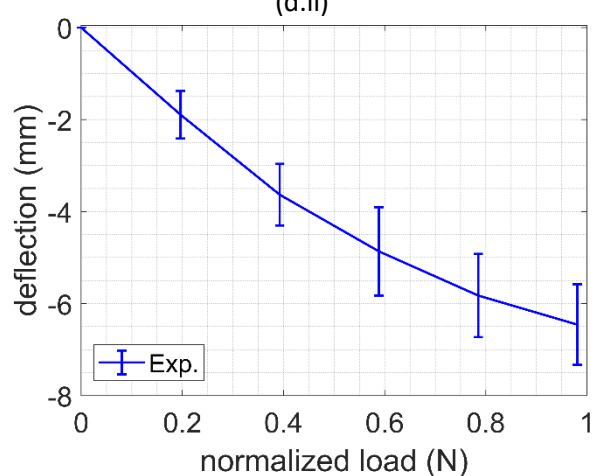
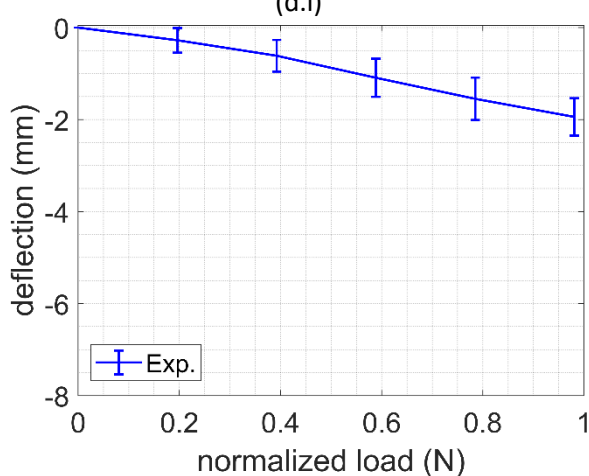
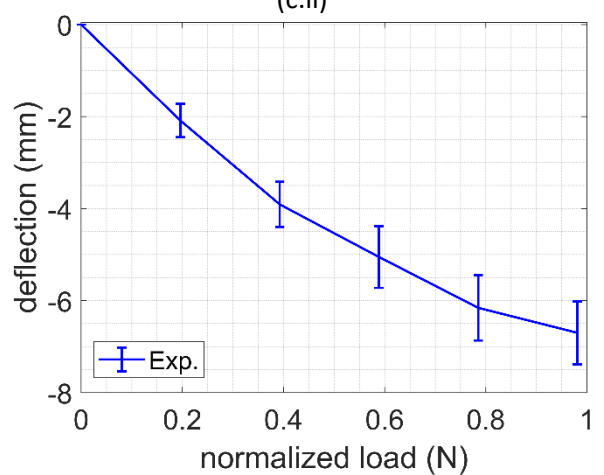
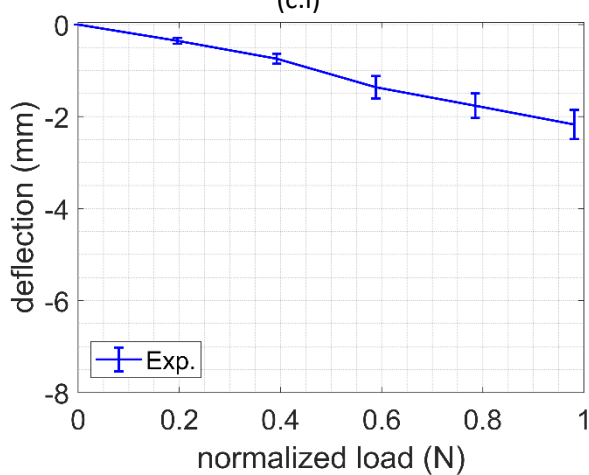
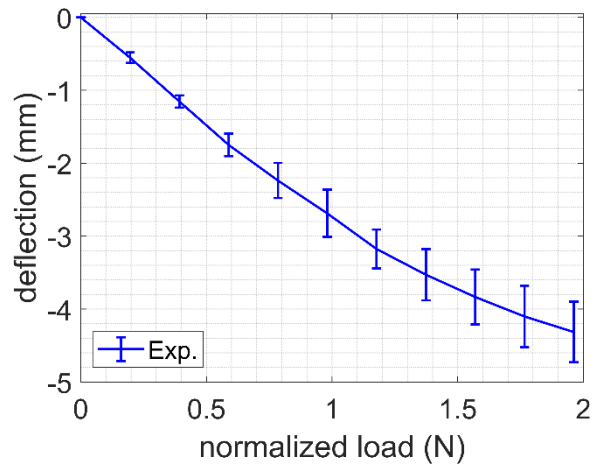
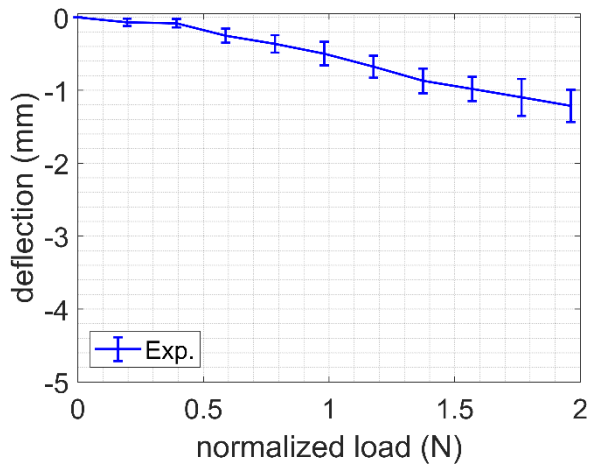
$$u(l) = - \int_0^l \left(2\sin^2 \left(\frac{\tan^{-1} \left(\frac{1}{2} Bx^2 + Cx \right)}{2} \right) \right) dx + Dl \quad (B.40)$$

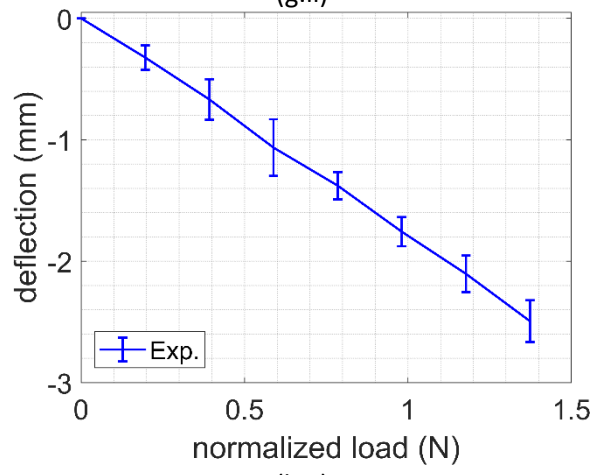
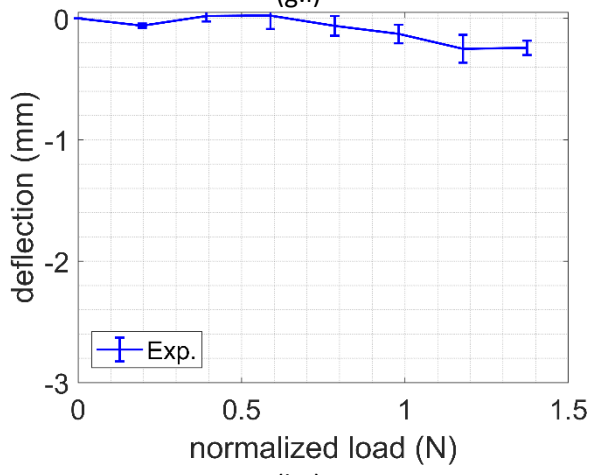
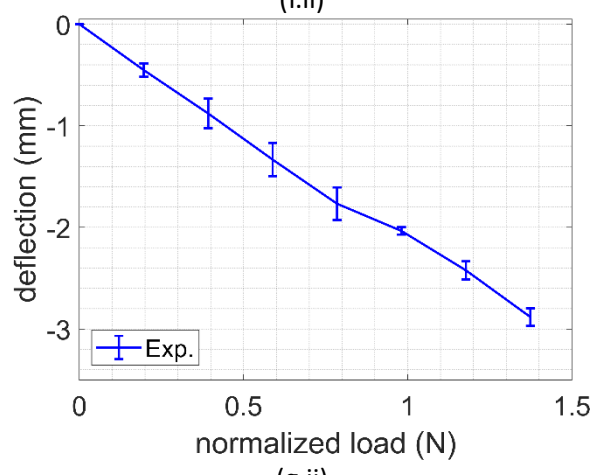
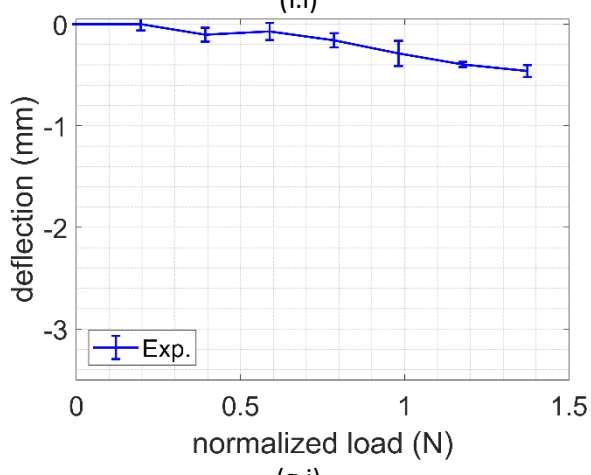
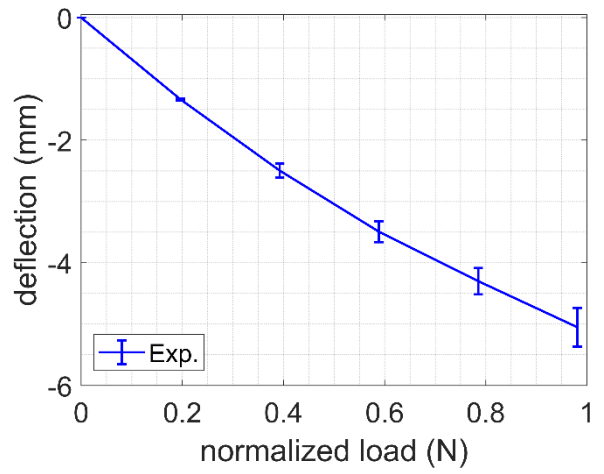
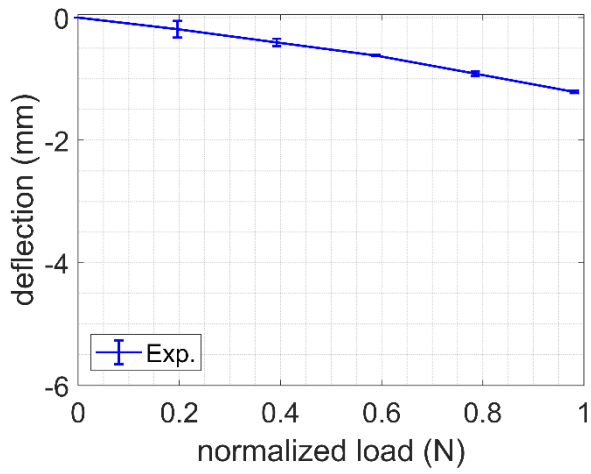
$$v(l) = \frac{1}{6} Bl^3 + \frac{1}{2} Cl^2 \quad (B.41)$$

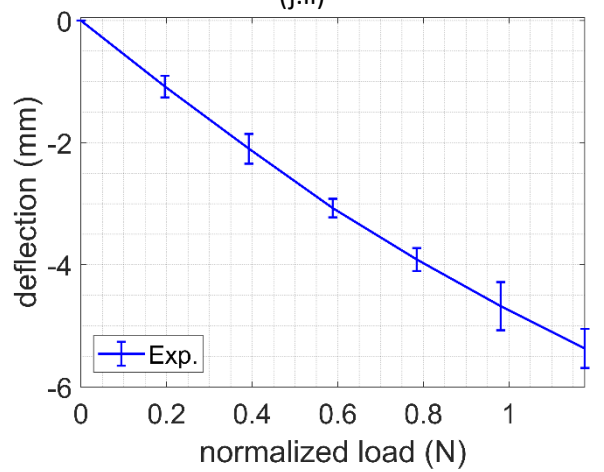
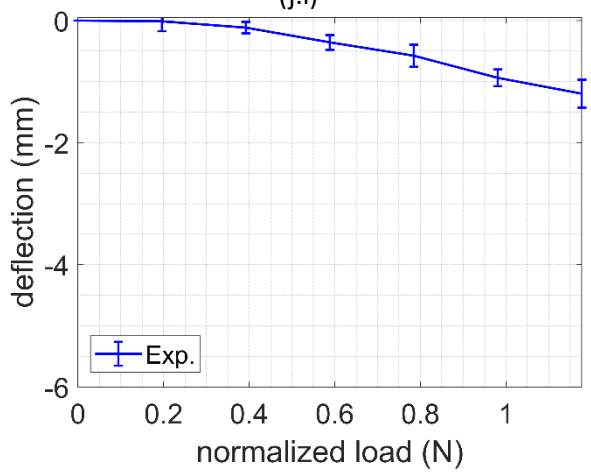
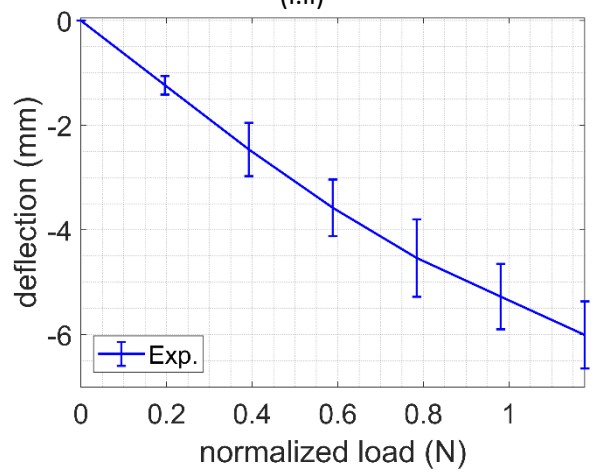
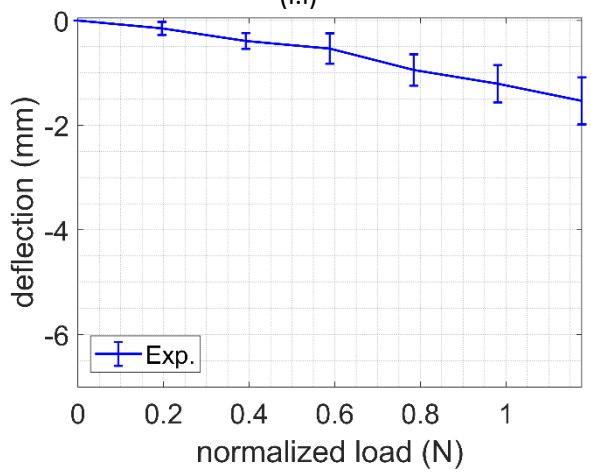
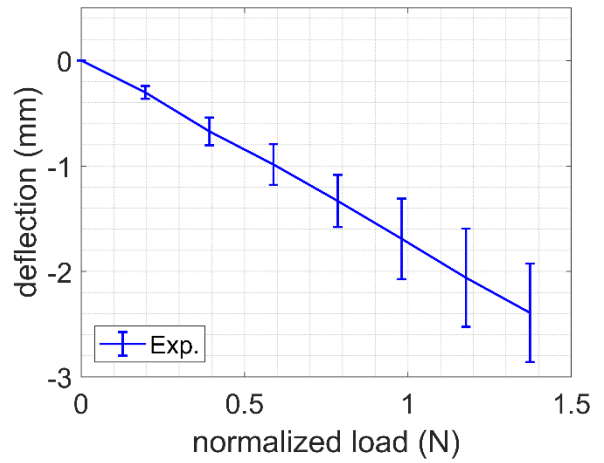
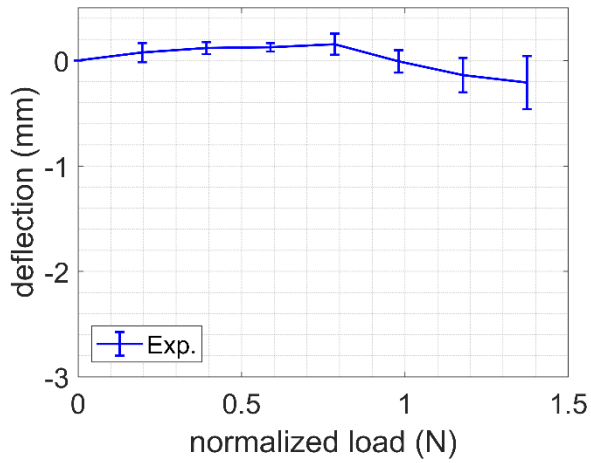
Appendix C: Results of flexible beam experiment

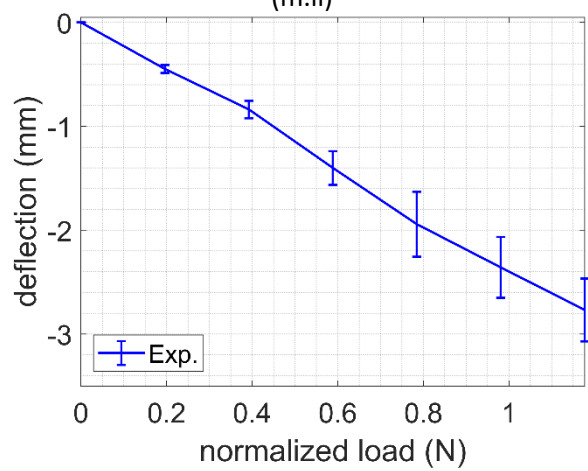
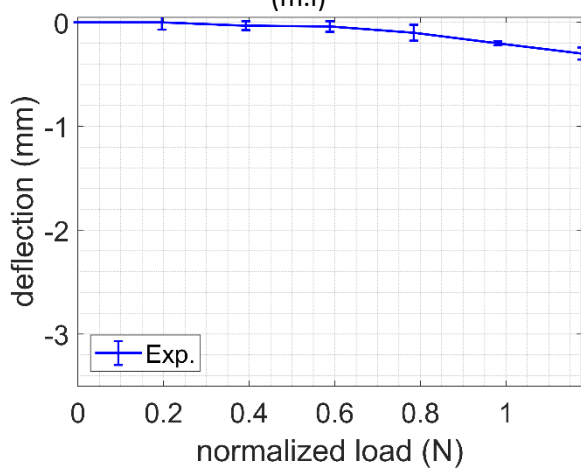
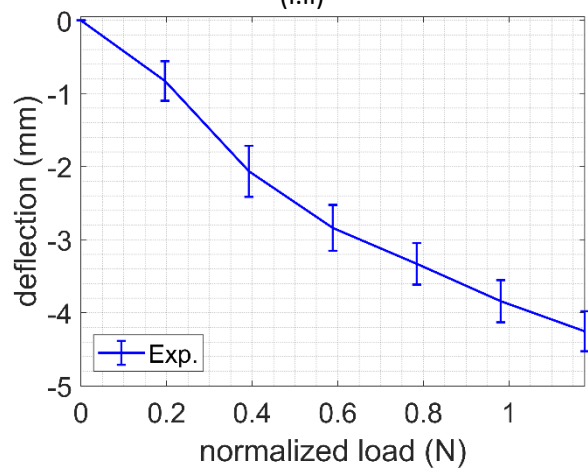
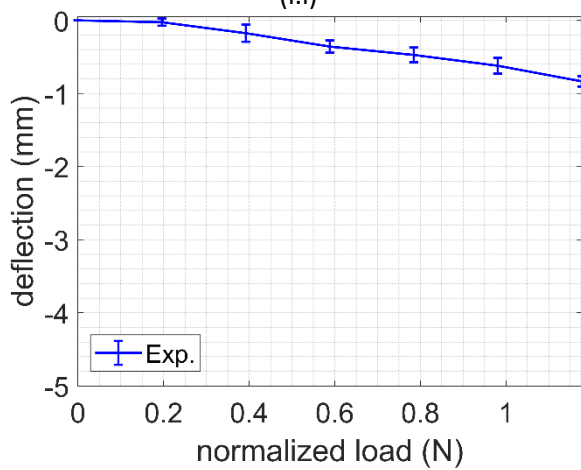
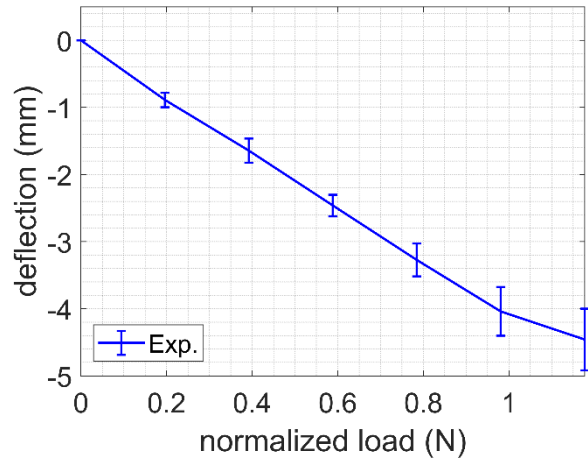
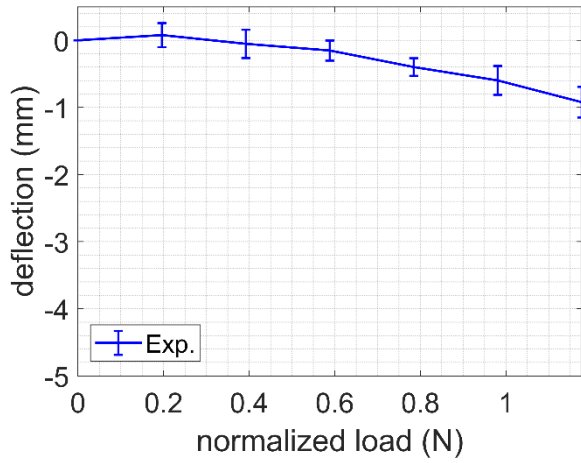
The experimental results of all 18 specimen configurations of flexible beam joints tested in Chapter 3 are presented here, Figure C.1. The x and y deflection for each beam is separated for clarity and includes the average and standard deviation. Table C.1 describes the specimen dimensions for each configuration ID. It should be noted that the flexible specimens angularly deflected more than the stiff ones, as seen in the x-axis ranges.

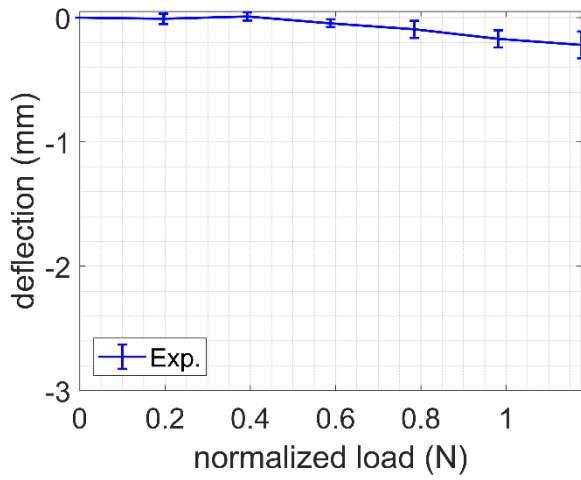




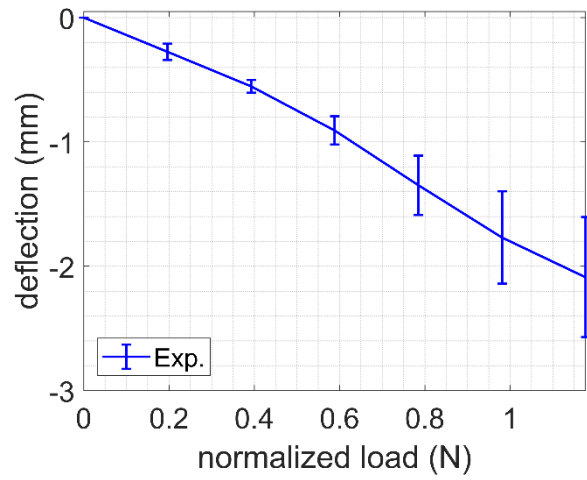




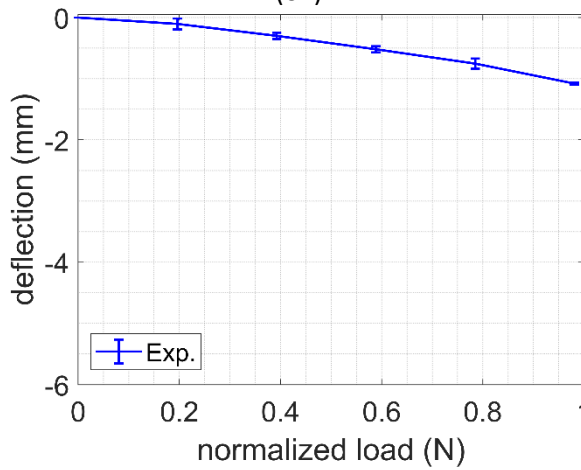




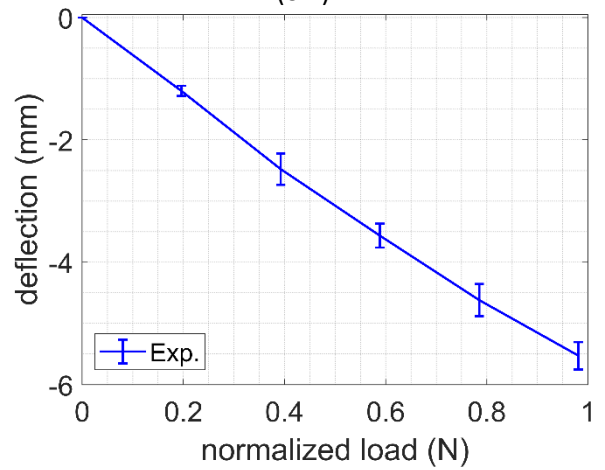
(o.i)



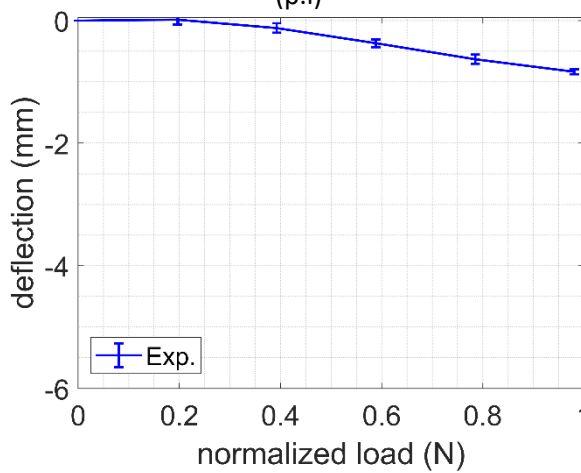
(o.ii)



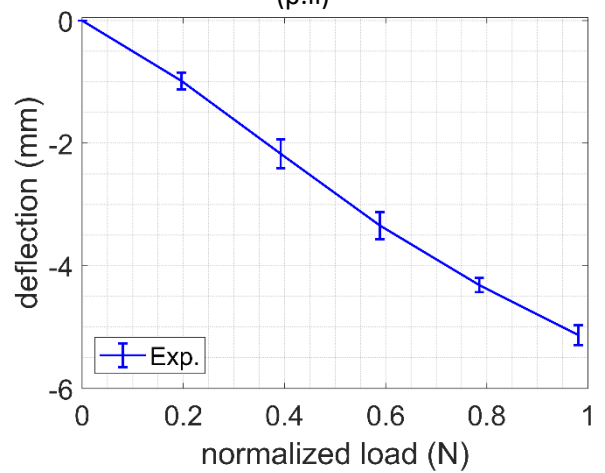
(p.i)



(p.ii)



(q.i)



(q.ii)

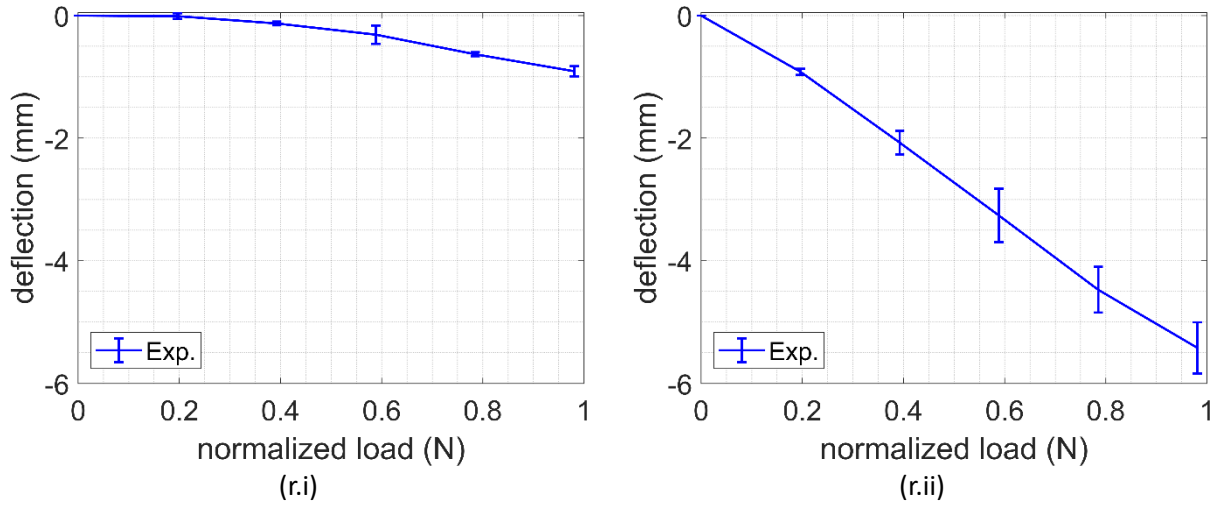


Figure C.1: Experimental results of flexible beam joints, in the x (i) and y (ii) directions; (a) specimen 1; (b) specimen 2; (c) specimen 3; (d) specimen 4; (e) specimen 5; (f) specimen 6; (g) specimen 7; (h) specimen 8; (i) specimen 9; (j) specimen 10; (k) specimen 11; (l) specimen 12; (m) specimen 13; (n) specimen 14; (o) specimen 15; (p) specimen 16; (q) specimen 17; (r) specimen 18

Table C.1: ID and dimensions of flexible beam joints

Specimen ID	l (mm)	h (mm)	w (mm)
1			8
2	10.0	1.8	10
3			12
4			8
5	15.0	1.8	10
6			12
7			8
8	10.0	2.7	10
9			12
10			8
11	15.0	2.7	10
12			12
13			8
14	10.0	3.6	10
15			12
16			8
17	15.0	3.6	10
18			12

Appendix D: Kinematic component derivations and definitions

When deriving the kinematics of the prosthetic finger, several key matrices and vectors must be defined to describe the configuration of the system. A body in a 2D system will be composed of three global coordinates, X , Y , and θ , which are used to translate and transform the local position vector, \bar{u}_p^i , of an arbitrary point, P^i , to the global position vector, r_p^i , Figure D.1.

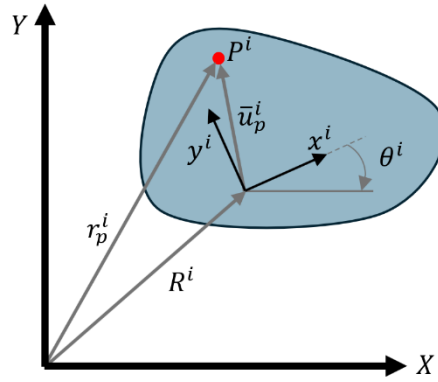


Figure D.1: Global position matrices of an arbitrary point P^i

To begin, the point P^i has a local position of,

$$\bar{u}_p^i = [\bar{x}_p^i \ \bar{y}_p^i]^T \quad (D.1)$$

where \bar{x}_p^i and \bar{y}_p^i are in the local frame x^i, y^i .

To represent the local position vector \bar{u}_p^i in the global frame as u_p^i , the transformation matrix, A^i , is used to account for the rotation of the local frame by θ^i ,

$$A^i = \begin{bmatrix} \cos(\theta^i) & -\sin(\theta^i) \\ \sin(\theta^i) & \cos(\theta^i) \end{bmatrix} \quad (D.2)$$

Or,

$$u_p^i = A^i \bar{u}_p^i \quad (D.3)$$

The global position of the local frame is written as,

$$R^i = [X \ Y]^T \quad (D.4)$$

Where X and Y are the global coordinates of origin i . Now the global position of P^i is written as the addition of the global position vector with the transformed local position vector,

$$r_p^i = R^i + A^i \bar{u}_p^i$$

When deriving the kinematics for a system, a constrain matrix, $C(q)$, is needed to limit the degrees of freedom, where C is the constrain matrix and q are the coordinates of the system bodies. One of the most common constraint equations describes the limitations of two bodies attached together by a hinged joint,

$$C(q^i, q^{i+1}) = R^{i+1} + A^{i+1} \bar{u}_p^{i+1} - R^i - A^i \bar{u}_p^i \quad (D.5)$$

Where p represents the joint connecting bodies $i + 1$ and i .

Appendix E: Converting flexible cantilever beams to torsional springs using flexible beam FEA modeling

The bending behavior of the 3D printed, hyperelastic thermoplastic polyurethane, NinjaFlex®, was experimentally evaluated in Chapter 4 and verified through closed form and FEA modeling in Chapter 5 with sufficient accuracy. To simplify the analysis of Chapter 6, it was decided to replace each beam joint by an equivalent combination of hinge joint and a nonlinear torsional spring, Figure E.1. Due to the consistency of the FEA modeling from Chapter 5, the angular displacement for each joint was calculated using the simulated *load* and *COM* locations.

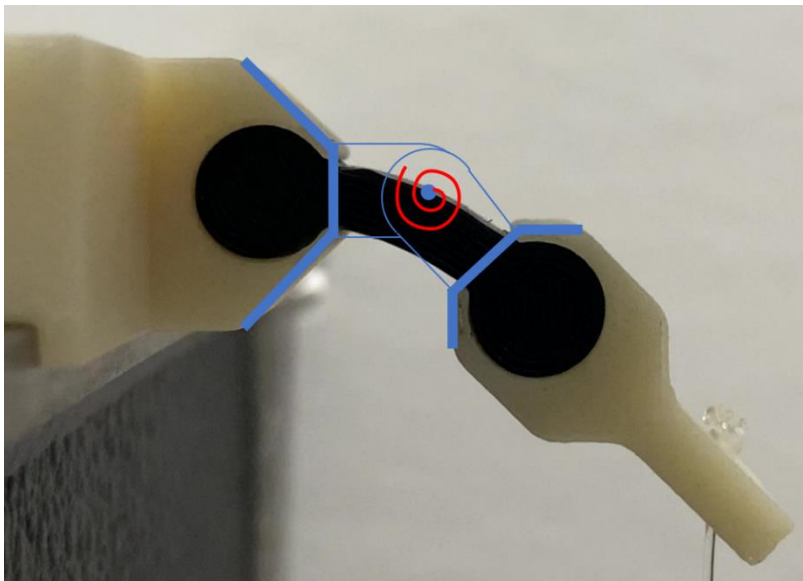


Figure E.1: Representation of the hinge/joint nonlinear spring equivalent of a beam joint

To determine the equivalent spring stiffness parameters, the relationship between the angular deflection and the moment acting on the joint must be defined. The angular deflection

of the beam joint can be calculated based on comparing two known points on the free end bracket, the center of mass (C) and the load location (L) with respect to a frame fixed at the other end of the beam joint, Figure E.2. The inverse tangent of the vector connecting these two points yielded the angle of the beam joint, Eqn. (E.1).

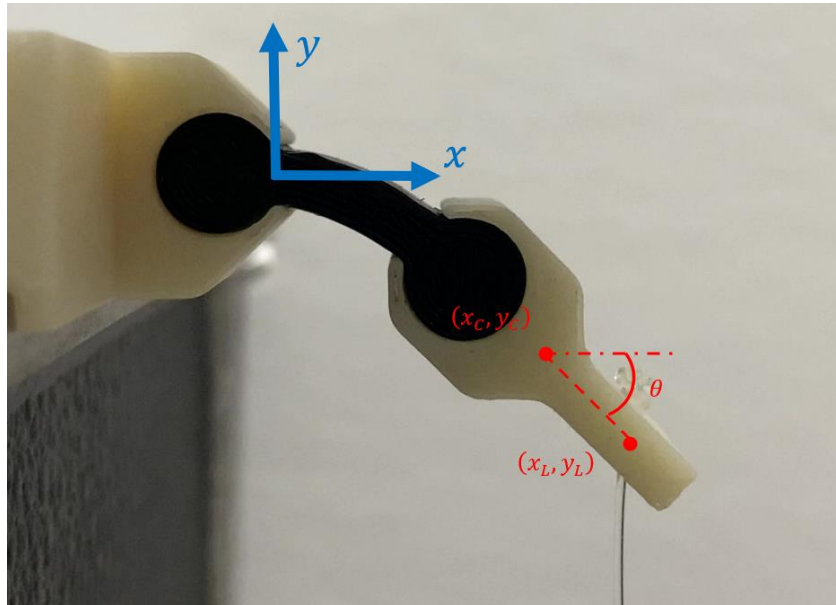


Figure E.2: Calculation of angular deflection

$$\theta_n = \tan^{-1} \left(\frac{y_{L,n} - y_{C,n}}{x_{L,n} - x_{C,n}} \right) \quad (E.1)$$

where the subscript n is the respective applied load number.

Next, the corresponding moment that induces the angular deflection was determined based on both the mass of the free end bracket and each induced load, Figure E.3.

$$M_{eq,n} = a_B P_B \cos(\theta_n) + a_W P_{W,n} \cos(\theta_n) \quad (E.2)$$

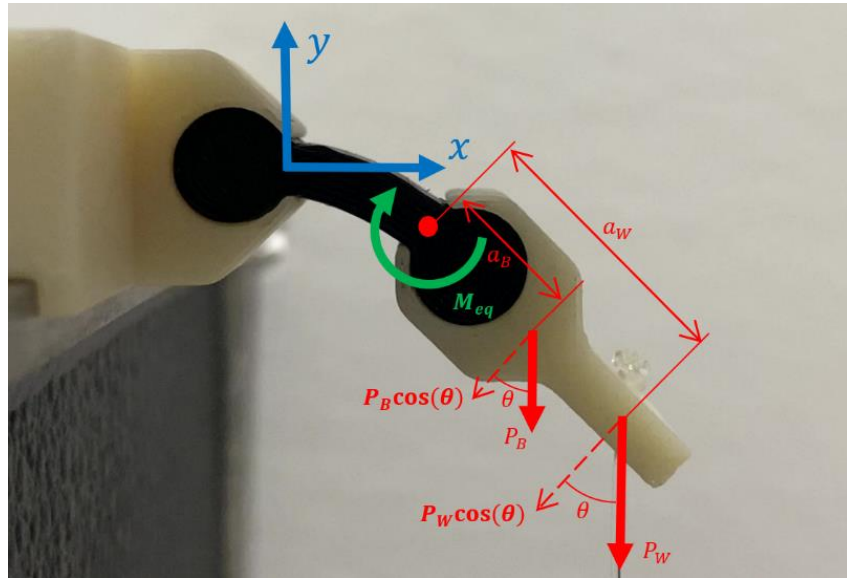


Figure E.3: Calculation of equivalent moment for torsional stiffness

The moment and angular displacement were plotted for a typical specimen 1, Figure E.4. A second order polynomial regression was fitted to the plotted data, Eqn. (E.3); while the data for some specimen configurations initially appears linear, the curvature of the torsional stiffness was more apparent in other specimen configurations. Therefore, a second order polynomial was used for all specimens for consistency.

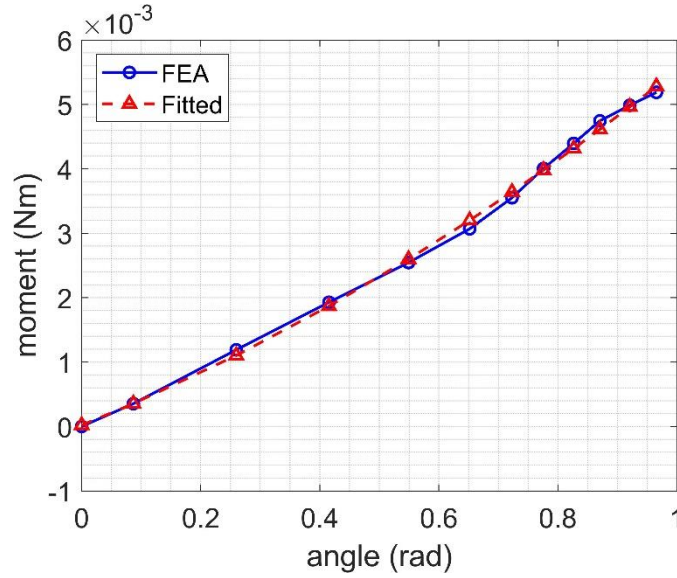


Figure E.4: Example of angular displacement with respect to moment

$$M_{eq}(\theta) = a\theta^2 + b\theta + c \quad (E.3)$$

The first derivative of the fitted curve provides the torsional stiffness, k_T , of the flexible beam joint, Eqn. (E.4), which describes the torsional stiffness as the angle changes.

$$k_T(\theta) = 2a\theta + b \quad (E.4)$$

The coefficients of the moment-angle curve, a , b , and c are needed for use in modeling the flexible beams.

The fitted curve provides the coefficients needed for Eqn. (E.3), with an R^2 value of 0.9979. The fitted plots for all remaining joint configurations are found in figure E.6, and their respective coefficients and R^2 values are found in Table E.1. As the intercept of the plots are set to (0,0), the coefficient c becomes zero as well. It was noted that the torsional stiffness behavior

of stiffer specimens tended towards more a more linear behavior and more flexible specimens had a more prominent nonlinear behavior.

Table E.1: Nonlinear torsional stiffness coefficients and R^2 values

Specimen ID	l (mm)	h (mm)	w (mm)	a	b	R^2
1	10.0	1.8	8	0.002	0.004	0.998
2			10	0.003	0.004	0.997
3			12	0.003	0.006	0.997
4	15.0	1.8	8	0.003	0.002	0.997
5			10	0.003	0.002	0.996
6			12	0.002	0.003	0.997
7	10.0	2.7	8	-0.002	0.015	1.000
8			10	-0.002	0.019	1.000
9			12	-0.002	0.023	1.000
10	15.0	2.7	8	-0.001	0.010	1.000
11			10	-0.001	0.012	1.000
12			12	-0.001	0.014	1.000
13	10.0	3.6	8	-0.005	0.035	1.000
14			10	-0.005	0.043	1.000
15			12	-0.007	0.051	1.000
16	15.0	3.6	8	-0.003	0.022	1.000
17			10	-0.004	0.027	1.000
18			12	-0.003	0.032	1.000

The dimensions of the flexible joints used in 3-digit finger modeling in Chapter 6 are slightly different than the dimensions of the joints tested so far. To find the nonlinear torsional stiffness values that correspond to these different dimensioned joints, they were simulated in the same manner. The results of the proximal and middle/distal joints are found in Figure E.5, and the respective coefficients and R^2 are found in Table E.2. Torsional coefficients for the thumb joints of the original Flexy-Hand 2 were approximated from similarly sized beams in Table E.1 and provided in Table E.2.

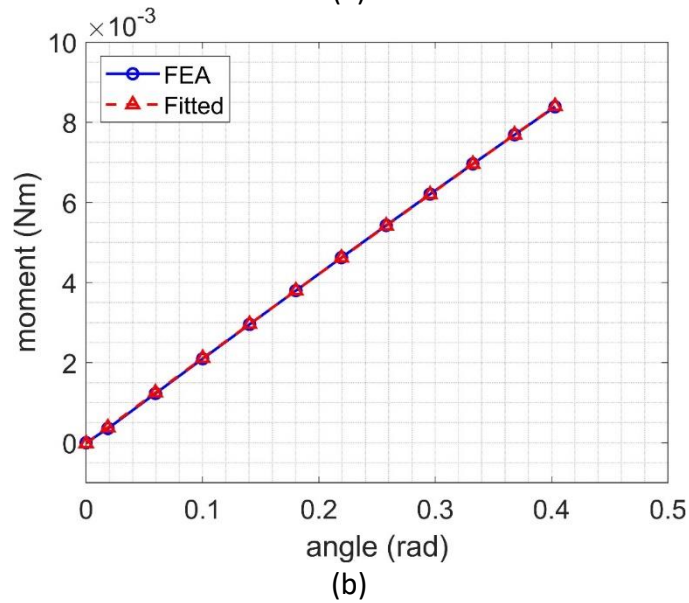
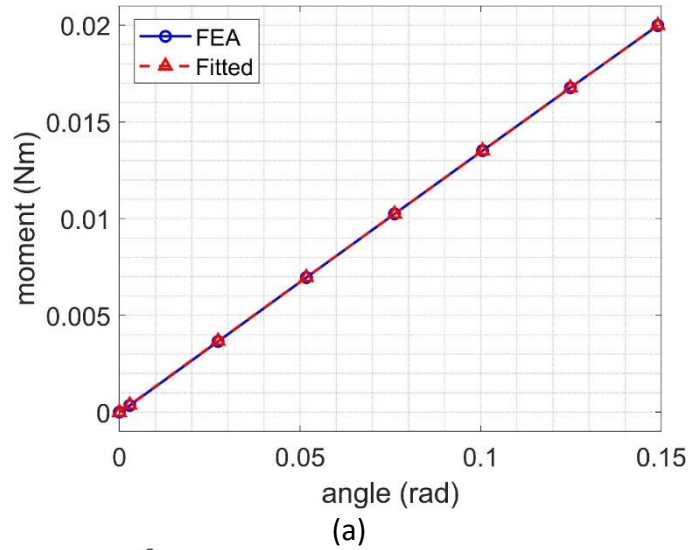


Figure E.5: Moment-angle plot for finding nonlinear stiffness coefficients of proximal and middle/distal joints in the 3-digit finger modeling; (a) proximal joint; (b) middle/distal joint

Table E.2: Nonlinear torsional stiffness coefficients and R^2 values for 3-digit finger

Joint	a	b	R^2
Proximal	-0.007	0.135	1.000
Middle/Distal	-0.001	0.022	1.000
Thumb	0.003	0.006	0.997

References

- [1] Jung, Y. H., Yoo, J. Y., Vázquez-Guardado, A., Kim, J. H., Kim, J. T., Luan, H., Park, M., Lim, J., Shin, H. S., Su, C. J., Schloen, R., Trueb, J., Avila, R., Chang, J. K., Yang, D. S., Park, Y., Ryu, H., Yoon, H. J., Lee, G., Jeong, H., Kim, J. U., Akhtar, A., Cornman, J., Kim, T. il, Huang, Y., and Rogers, J. A., 2022, "A Wireless Haptic Interface for Programmable Patterns of Touch across Large Areas of the Skin," *Nat Electron*, **5**(6), pp. 374–385.
- [2] Iberite, F., Muheim, J., Akouissi, O., Gallo, S., Rognini, G., Morosato, F., Clerc, A., Kalff, M., Gruppioni, E., Micera, S., and Shokur, S., 2023, "Restoration of Natural Thermal Sensation in Upper-Limb Amputees," *Science* (1979), **380**(6646), pp. 731–735.
- [3] Inouye, J. M., and Valero-Cuevas, F. J., 2014, "Anthropomorphic Tendon-Driven Robotic Hands Can Exceed Human Grasping Capabilities Following Optimization," *International Journal of Robotics Research*, **33**(5), pp. 694–705.
- [4] Blough, D. K., Hubbard, S., McFarland, L. V., Smith, D. G., Gambel, J. M., and Reiber, G. E., 2010, "Prosthetic Cost Projections for Servicemembers with Major Limb Loss from Vietnam and OIF/OEF," *J Rehabil Res Dev*, **47**(4), pp. 387–402.
- [5] 2022, "Upper and Lower Limb Reduction Defects," Center for Disease Control and Prevention.

- [6] Østlie, K., Lesjø, I. M., Franklin, R. J., Garfelt, B., Skjeldal, O. H., and Magnus, P., 2012, "Prosthesis Rejection in Acquired Major Upper-Limb Amputees: A Population-Based Survey," *Disabil Rehabil Assist Technol*, **7**(4), pp. 294–303.
- [7] Messimer, P., O'Toole, B., and Trabia, M., 2019, "Identification of the Mechanical Characteristics of 3D Printed NinjaFlex®," *ASME International Mechanical Engineering Congress and Exposition, Proceedings (IMECE)*, **9**, pp. 1–9.
- [8] Pitaru, A. A., Lacombe, J. G., Cooke, M. E., Beckman, L., Steffen, T., Weber, M. H., Martineau, P. A., and Rosenzweig, D. H., 2020, "Investigating Commercial Filaments for 3D Printing of Stiff and Elastic Constructs with Ligament-like Mechanics," *Micromachines (Basel)*, **11**(9), pp. 1–15.
- [9] Reppel, T., and Weinberg, K., 2018, "Experimental Determination of Elastic and Rupture Properties of Printed Ninjaflex," *Technische Mechanik*, **38**(1), pp. 104–112.
- [10] Holmes, D. W., Singh, D., Lamont, R., Daley, R., Forrestal, D. P., Slattery, P., Pickering, E., Paxton, N. C., Powell, S. K., and Woodruff, M. A., 2022, "Mechanical Behaviour of Flexible 3D Printed Gyroid Structures as a Tuneable Replacement for Soft Padding Foam," *Addit Manuf*, **50**.
- [11] Manero, A., Smith, P., Sparkman, J., Dombrowski, M., Courbin, D., Kester, A., Womack, I., and Chi, A., 2019, "Implementation of 3D Printing Technology in the Field of Prosthetics: Past, Present, and Future," *Int J Environ Res Public Health*, **16**.

- [12] Votta, A. M., Gunay, S. Y., Zylich, B., Skorina, E., Rameshwar, R., Erdogmus, D., and Onal, C. D., 2020, "Kinematic Optimization of an Underactuated Anthropomorphic Prosthetic Hand," *2020 IEEE/RSJ International Conference on Intelligent Robots and Systems (IROS)*, IEEE, pp. 3397–3403.
- [13] Omarkulov, N., Telegenov, K., Zeinullin, M., Begalinova, A., and Shintemirov, A., 2015, "Design and Analysis of an Underactuated Anthropomorphic Finger for Upper Limb Prosthetics," *Proceedings of the Annual International Conference of the IEEE Engineering in Medicine and Biology Society, EMBS*, Institute of Electrical and Electronics Engineers Inc., pp. 2474–2477.
- [14] Belter, J. T., Segil, J. L., Dollar, A. M., and Weir, R. F., 2013, "Mechanical Design and Performance Specifications of Anthropomorphic Prosthetic Hands: A Review," *J Rehabil Res Dev*, **50**(5), pp. 599–618.
- [15] Xiong, C. H., Chen, W. R., Sun, B. Y., Liu, M. J., Yue, S. G., and Chen, W. Bin, 2016, "Design and Implementation of an Anthropomorphic Hand for Replicating Human Grasping Functions," *IEEE Transactions on Robotics*, **32**(3), pp. 652–671.
- [16] You, W. S., Lee, Y. H., Kang, G., Oh, H. S., Seo, J. K., and Choi, H. R., 2019, "Kinematic Design Optimization for Anthropomorphic Robot Hand Based on Interactivity of Fingers," *Intell Serv Robot*, **12**(2), pp. 197–208.
- [17] Omarkulov, N., Telegenov, K., Zeinullin, M., Begalinova, A., and Shintemirov, A., 2015, "Design and Analysis of an Underactuated Anthropomorphic Finger for Upper Limb Prosthetics," *Proceedings of the Annual International Conference of*

the IEEE Engineering in Medicine and Biology Society, EMBS, Institute of Electrical and Electronics Engineers Inc., pp. 2474–2477.

- [18] Biddiss, E., and Chau, T., 2007, “Upper Limb Prosthesis Use and Abandonment: A Survey of the Last 25 Years,” *Prosthet Orthot Int*, **31**(3), pp. 236–257.
- [19] Cabibihan, J. J., Alkhatib, F., Mudassir, M., Lambert, L. A., Al-Kwafi, O. S., Diab, K., and Mahdi, E., 2021, “Suitability of the Openly Accessible 3D Printed Prosthetic Hands for War-Wounded Children,” *Front Robot AI*, **7**.
- [20] Zuniga, J., Katsavelis, D., Peck, J., Stollberg, J., Petrykowski, M., Carson, A., and Fernandez, C., 2015, “Cyborg Beast: A Low-Cost 3d-Printed Prosthetic Hand for Children with Upper-Limb Differences,” *BMC Res Notes*, **8**(1), p. 10.
- [21] Gyrobot, 2014, “Flexy-Hand 2,” Thingiverse.
- [22] Alturkistani, R., Kavin, A., Devasahayam, S., Thomas, R., Colombini, E. L., Cifuentes, C. A., Homer-Vanniasinkam, S., Wurdemann, H. A., and Moazen, M., 2020, “Affordable Passive 3D-Printed Prosthesis for Persons with Partial Hand Amputation,” *Prosthet Orthot Int*, **44**(2), pp. 92–98.
- [23] Ku, I., Lee, G. K., Park, C. Y., Lee, J., and Jeong, E., 2019, “Clinical Outcomes of a Low-Cost Single-Channel Myoelectric-Interface Three-Dimensional Hand Prosthesis,” *Arch Plast Surg*, **46**(4), pp. 303–310.

- [24] Castro, M. C. F., Pinheiro, W. C., and Rigolin, G., 2022, "A Hybrid 3D Printed Hand Prosthesis Prototype Based on SEMG and a Fully Embedded Computer Vision System," *Front Neurorobot*, **15**.
- [25] Dong, H., Asadi, E., Qiu, C., Dai, J., and Chen, I. M., 2018, "Geometric Design Optimization of an Under-Actuated Tendon-Driven Robotic Gripper," *Robot Comput Integr Manuf*, **50**, pp. 80–89.
- [26] Inouye, J. M., and Valero-Cuevas, F. J., 2014, "Anthropomorphic Tendon-Driven Robotic Hands Can Exceed Human Grasping Capabilities Following Optimization," *International Journal of Robotics Research*, **33**(5), pp. 694–705.
- [27] Wahit, M. A. A., Ahmad, S. A., Marhaban, M. H., Wada, C., and Izhar, L. I., 2020, "3d Printed Robot Hand Structure Using Four-Bar Linkage Mechanism for Prosthetic Application," *Sensors (Switzerland)*, **20**(15), pp. 1–22.
- [28] Omarkulov, N., Telegenov, K., Zeinullin, M., Begalinova, A., and Shintemirov, A., 2015, "Design and Analysis of an Underactuated Anthropomorphic Finger for Upper Limb Prosthetics," *Proceedings of the Annual International Conference of the IEEE Engineering in Medicine and Biology Society, EMBS*, Institute of Electrical and Electronics Engineers Inc., pp. 2474–2477.
- [29] Kashef, S. R., Amini, S., and Akbarzadeh, A., 2020, "Robotic Hand: A Review on Linkage-Driven Finger Mechanisms of Prosthetic Hands and Evaluation of the Performance Criteria," *Mech Mach Theory*, **145**.

- [30] Yoon, D., Lee, G., Lee, S., and Choi, Y., 2016, "Underactuated Finger Mechanism for Natural Motion and Self-Adaptive Grasping towards Bionic Partial Hand," *6th IEEE RAS/EMBS International Conference on Biomedical Robotics and Biomechanics (BioRob)*, IEEE, UTown, Singapore, pp. 548–553.
- [31] Qi, H. J., and Boyce, M. C., 2005, "Stress-Strain Behavior of Thermoplastic Polyurethanes," *Mechanics of Materials*, **37**(8), pp. 817–839.
- [32] Wang, Y., Luo, W., Huang, J., Peng, C., Wang, H., Yuan, C., Chen, G., Zeng, B., and Dai, L., 2020, "Simplification of Hyperelastic Constitutive Model and Finite Element Analysis of Thermoplastic Polyurethane Elastomers," *Macromol Theory Simul*, **29**(4).
- [33] Alici, G., Canty, T., Mutlu, R., Hu, W., and Sencadas, V., 2018, "Modeling and Experimental Evaluation of Bending Behavior of Soft Pneumatic Actuators Made of Discrete Actuation Chambers," *Soft Robot*, **5**(1).
- [34] Rismalia, M., Hidajat, S. C., Permana, I. G. R., Hadisujoto, B., Muslimin, M., and Triawan, F., 2019, "Infill Pattern and Density Effects on the Tensile Properties of 3D Printed PLA Material," *4th Annual Applied Science and Engineering Conference, Journal of Physics: Conference Series*, IOP Publishing Ltd.
- [35] El Magri, A., Bencaid, S. E., Vanaei, H. R., and Vaudreuil, S., 2022, "Effects of Laser Power and Hatch Orientation on Final Properties of PA12 Parts Produced by Selective Laser Sintering," *Polymers (Basel)*, **14**(3674).

- [36] Vanaei, H. R., Magri, A. El, Rastak, M. A., Vanaei, S., Vaudreuil, S., and Tcharkhtchi, A., 2022, "Numerical–Experimental Analysis toward the Strain Rate Sensitivity of 3D-Printed Nylon Reinforced by Short Carbon Fiber," *Materials*, **15**(24), p. 8722.
- [37] Ouassil, S., El Magri, A., Vanaei, H. R., and Vaudreuil, S., 2023, "Investigating the Effect of Printing Conditions and Annealing on the Porosity and Tensile Behavior of 3D-printed Polyetherimide Material in Z-direction," *J Appl Polym Sci*, **140**(4).
- [38] Yarwindran, M., Azwani Sa'aban, N., Ibrahim, M., and Periyasamy, R., 2016, "Thermoplastic Elastomer Infill Pattern Impact on Mechanical Properties 3D Printed Customized Orthotic Insole," *Journal of Engineering and Applied Sciences*, **11**(10), pp. 6519–6524.
- [39] Gao, G., Dwivedi, A., and Liarokapis, M., 2023, "The New Dexterity Adaptive Humanlike Robot Hand: Employing a Reconfigurable Palm for Robust Grasping and Dexterous Manipulation," *2023 IEEE International Conference on Robotics and Automation (ICRA)*, IEEE, London, United Kingdom, pp. 10310–10316.
- [40] Stoppa, M. H., and Carvalho, J. C. M., 2015, "KINEMATIC MODELING OF A MULTI-FINGERED HAND PROSTHESIS FOR MANIPULATION TASKS," *Congresso Nacional de Matematica Aplicada a Industria*, pp. 779–788.
- [41] Cosenza, C., Niola, V., and Savino, S., 2018, "A Mechanical Hand for Prosthetic Applications: Multibody Model and Contact Simulation," *Proceedings of the Institution of Mechanical Engineers, Part H: Journal of Engineering in Medicine*, SAGE Publications Ltd, pp. 819–825.

- [42] Oh, D. J., Li, Z. Y., Kim, J. H., Choi, H. R., Moon, H., and Koo, J. C., 2020, "A Flexible Self-Recovery Finger Joint for a Tendon-Driven Robot Hand," *Review of Scientific Instruments*, **91**(11).
- [43] Neha, E., Suhaib, M., Mukherjee, S., and Shrivastava, Y., 2023, "Kinematic Analysis of Four-Fingered Tendon Actuated Robotic Hand," *Australian Journal of Mechanical Engineering*, **21**(2), pp. 541–551.
- [44] Lee, H. C., 2018, "DESIGN AND ANALYSIS OF A BODY-POWERED UNDERACTUATED PROSTHETIC HAND," School of Mechanical Engineering, Purdue University.
- [45] Kontoudis, G. P., Liarokapis, M., Vamvoudakis, K. G., and Furukawa, T., 2019, "An Adaptive Actuation Mechanism for Anthropomorphic Robot Hands," *Front Robot AI*, **6**.
- [46] Kontoudis, G. P., Liarokapis, M., and Vamvoudakis, K. G., 2019, "An Adaptive, Humanlike Robot Hand with Selective Interdigitation: Towards Robust Grasping and Dexterous, In-Hand Manipulation," *2019 IEEE 19th International Conference on Humanoid Robots (Humanoids)*, IEEE, Toronto, pp. 251–258.
- [47] Tarvainen, T. V. J., Yu, W., and Gonzalez, J., 2012, "Development of MorphHand: Design of an Underactuated Anthropomorphic Rubber Finger for a Prosthetic Hand Using Compliant Joints," *IEEE International Conference on Robotics and Biomimetics*, IEEE, Guangzhou, pp. 142–147.

- [48] Kaya, Z. E., and Yilmaz, A., 2019, "Modeling and Simulation of an Anthropomorphic Hand Prosthesis with an Object Interaction," *Comput Methods Programs Biomed*, **183**.
- [49] Lubombo, C., and Huneault, M. A., 2018, "Effect of Infill Patterns on the Mechanical Performance of Lightweight 3D-Printed Cellular PLA Parts," *Mater Today Commun*, **17**, pp. 214–228.
- [50] Alafaghani, A., Qattawi, A., Alrawi, B., and Guzman, A., 2017, "Experimental Optimization of Fused Deposition Modelling Processing Parameters: A Design-for-Manufacturing Approach," *Procedia Manufacturing*, Elsevier B.V., pp. 791–803.
- [51] Coppola, B., Cappetti, N., Maio, L. Di, Scarfato, P., and Incarnato, L., 2018, "3D Printing of PLA/Clay Nanocomposites: Influence of Printing Temperature on Printed Samples Properties," *Materials*, **11**(10).
- [52] Yang, C., Tian, X., Li, D., Cao, Y., Zhao, F., and Shi, C., 2017, "Influence of Thermal Processing Conditions in 3D Printing on the Crystallinity and Mechanical Properties of PEEK Material," *J Mater Process Technol*, **248**, pp. 1–7.
- [53] LulzBot, "Cura LulzBot Edition."
- [54] ASTM, 2014, "Standard Test Method for Tensile Properties of Plastics," *Book of Standards*, ASME.
- [55] LulzBot, "LulzBot Taz Mini 2," FAME 3D.

- [56] Yap, H. K., Ng, H. Y., and Yeow, C. H., 2016, "High-Force Soft Printable Pneumatics for Soft Robotic Applications," *Soft Robot*, **3**(3), pp. 144–158.
- [57] NinjaTek, 2016, *Technical Specifications: NinjaFlex 3D Printing Filament*.
- [58] Kim, B., Lee, S. B., Lee, J., Cho, S., Park, H., Yeom, S., and Park, S. H., 2012, "A Comparison among Neo-Hookean Model, Mooney-Rivlin Model, and Ogden Model for Chloroprene Rubber," *International Journal of Precision Engineering and Manufacturing*, **13**(5), pp. 759–764.
- [59] Mihai, L. A., and Goriely, A., 2017, "How to Characterize a Nonlinear Elastic Material? A Review on Nonlinear Constitutive Parameters in Isotropic Finite Elasticity," *Proceedings of the Royal Society A: Mathematical, Physical and Engineering Sciences*, Royal Society Publishing.
- [60] Gkouti, E., Yenigun, B., Jankowski, K., and Czekanski, A., 2020, "NON-LINEAR STRETCH MODULUS OF MATERIALS UNDER SIMPLE TENSION," *Proceedings of the Canadian Society for Mechanical Engineering International Congress 2020*, CSME, Charlottetown, PE, Canada.
- [61] Beer, F. P., Johnston, E. R. Jr., DeWolf, J. T., and Mazurek, D. F., 2015, *Mechanics of Materials*, McGraw-Hill Education, New York.
- [62] Ding, S., Zou, B., Wang, P., and Ding, H., 2019, "Effects of Nozzle Temperature and Building Orientation on Mechanical Properties and Microstructure of PEEK and PEI Printed by 3D-FDM," *Polym Test*, **78**.

- [63] ASTM, "Standard Test Method for Tensile Properties of Plastics," *Book of Standards*, ASTM International.
- [64] Stratasys™, "ABSplus P430," Stratasys Ltd.
- [65] Stratasys™, "Fortus 250MC," Stratasys Ltd.
- [66] MathWorks Inc., 2021, "MATLAB: Image Processing Toolbox."
- [67] Hussain, I., Iqbal, Z., Malvezzi, M., Seneviratne, L., Gan, D., and Prattichizzo, D., 2018, "Modeling and Prototyping of a Soft Prosthetic Hand Exploiting Joint Compliance and Modularity," *2018 IEEE International Conference on Robotics and Biomimetics (ROBIO)*, IEEE, pp. 65–70.
- [68] Kim, N.-H., Sankar, B. V., and Kumar, A. V., 2018, *Introduction to Finite Element Analysis and Design*, Wiley.
- [69] Bhandari, S., and Lopez-Anido, R., 2018, "Finite Element Analysis of Thermoplastic Polymer Extrusion 3D Printed Material for Mechanical Property Prediction," *Addit Manuf*, **22**, pp. 187–196.
- [70] Catana, D.-I., Pop, M.-A., and Brus, D.-I., 2021, "Comparison between Tests and Simulations Regarding Bending Resistance of 3D Printed PLA Structures," *Polymers (Basel)*, **13**, p. 4371.
- [71] ANSYS Inc., 2021, "ANSYS Workbench."
- [72] Hylinger, P. R., and Reddy, J. N., 1988, "A Higher Order Beam Finite Element for Bending and Vibration Problems," *J Sound Vib*, **126**(2), pp. 309–326.

- [73] Chen, L., 2010, "An Integral Approach for Large Deflection Cantilever Beams," *Int J Non Linear Mech*, **45**(3), pp. 301–305.
- [74] Bisshopp, K. E., and Drucker, D. C., 1945, "Large Deflection of Cantilever Beams," *Q Appl Math*, **3**(3), pp. 272–275.
- [75] Shabana, A. A., 2010, *Computational Dynamics*, John Wiley & Sons Ltd.
- [76] Dassault Systemes, 2021, "SolidWorks."
- [77] Cordella, F., Ciancio, A. L., Sacchetti, R., Davalli, A., Cutti, A. G., Guglielmelli, E., and Zollo, L., 2016, "Literature Review on Needs of Upper Limb Prosthesis Users," *Front Neurosci*, **10**(MAY).
- [78] Mooney, M., 1940, "A Theory of Large Elastic Deformation," *J Appl Phys*, **11**(9), pp. 582–592.

Curriculum Vitae

Lucas Gallup

lucasgallup@gmail.com

EDUCATION

Doctor of Philosophy – Mechanical Engineering
University of Nevada, Las Vegas Expected Graduation May 2024

Master of Science in Mechanical Engineering
University of Nevada, Las Vegas December 2023

Bachelor of Science in Mechanical Engineering
University of Nevada, Las Vegas May 2019

SKILLS

- MATLAB, SolidWorks, ANSYS Mechanical, 3D printing, MS Office, LabVIEW
- Proficient in presenting to both technical and non-technical audiences, detail oriented, works well individually and in groups, eagerly willing to learn new skills, information, or technology.

WORK EXPERIENCE

University of Nevada, Las Vegas August 2019-Current
Graduate Assistant, Mechanical Engineering Department

Modeling of Underactuated 3D Printed Prosthetic Fingers

- Derived a model to predict the deflection of a tendon-actuated, underactuated 3D printed prosthetic finger with respect to tendon tension.
- The models were experimentally validated; deflection error for all three digits were less than 6%.

Mechanical Characterization of 3D Printing Filament

- Designed experimental test brackets and equipment to test the mechanical characteristics of a 3D printed hyperelastic thermoplastic polyurethane under bending and tensile loads
- Derived a closed form solution to the large deflection bending of cantilever beams 3D printed from NinjaFlex®
- Developed quasi-static Finite Element Analysis simulations of hyperelastic, nonlinear, large deflection models for experimental validation

Traffic Signal Failure Study

- Developed finite element models of key traffic signal components for stress and deflection responses and determined the fatigue life and potential source of failure

Colorectal Anastomosis Staple Failure Study

- Conducted burst testing on porcine colorectal anastomoses which were conducted using two common methods in human surgical practice

Finite Element Analysis of Glenoid Reverse Shoulder Arthroplasty

- Simulated common load conditions of a total reverse shoulder arthroplasty to understand patient limitations for successful bone integration

University of Nevada, Las Vegas

August 2023-Current

Instructor

Mechanical Engineering Department

- ME 302L – Mechanical Testing Lab

University of Nevada, Las Vegas

August 2019-May 2020

Instructor

Mechanical Engineering Department

- ME 423L – Instrument and Control Laboratory

PUBLICATIONS

Journal Publications

Fahmy, Y., Trabia, M. B., Ward, B., **Gallup, L.**, & Froehlich, M. (2024). Development of an Anisotropic Hyperelastic Material Model for Porcine Colorectal Tissues. *Bioengineering*, 11(1), 64. <https://doi.org/10.3390/bioengineering11010064>

Gallup, L.; Trabia, M.; O’Toole, B.; Fahmy, Y. Predicting the Bending of 3D Printed Hyperelastic Polymer Components. *Polymers (Basel)* **2023**, 15, 368, doi:10.3390/polym15020368.

Conference Proceedings

Youssef Fahmy, Mohamed Trabia, Brian Ward, **Lucas Gallup** and Whitney Elks, “A Comparison of the Pressure Failure of Two Colorectal Anastomoses Stapling Techniques,” *Design of Medical Devices (DMD2023)*, Minneapolis, MN, April 2023.

Lucas K. Gallup, Mohamed Trabia, Brendan O’Toole, Youssef Fahmy, “Toward Understanding Large Deflection Bending of 3d Printed Ninjaflex®,” *WIT Transactions on Engineering Sciences*, pp. 55-65, January 2021.

Technical Reports

M. Ren, M. Trabia, Y. Fahmy, **L. Gallup**, E. Zeigler, "Failure Assessment of a Traffic Signal Pole," Clark County, Traffic Management Division, 2023.

CONFERENCE PRESENTATIONS AND POSTERS

Lucas Gallup, Mohamed Trabia, Brendan O'Toole, Youssef Fahmy, "Effect of filament deposition on mechanical characteristics of 3d printed thermoplastic polyurethane," MaterialsToday Conference 2023 (MATA23), Singapore, August 2023.

B. O'Toole, **L. Gallup**, Y. Fahmy, M. Trabia, "3D Printing Process for Biomedical Applications", American Academy of Orthopaedic Surgeons (AAOS), Limb Lengthening and Reconstruction Society, March 7, 2023. (Invited presentation)

L. Gallup, Y. Fahmy, B. O'Toole, M. Trabia, "3D Printed Prosthetics", American Academy of Orthopaedic Surgeons (AAOS), Limb Lengthening and Reconstruction Society, March 7, 2023. (Invited presentation)

Brian C. Ward, Mary Froehlich, Whitney Elks, Mohamed B. Trabia, **Lucas Gallup**, Youssef Fahmy, "Preventing Colorectal Anastomosis Failure with Finite Element Method (FEM) Validated with Ex-VIVO Model," Mountain West CTR-IN Program: 2022 Annual Meeting, November 2022, Las Vegas, NV.

Lucas Gallup, Youssef Fahmy, Mohamed Trabia, Brendan O'Toole, "Hyperelastic Thermoplastic polyurethane (TPU) Material Characterization using Analytical and FEA Modeling," NNCI Nano + Additive Manufacturing Summit, Louisville, KY, August 2022.

L. Gallup, M. Trabia, B. O'Toole, Y. Fahmy, "Toward Understanding Large Deflection Bending of 3D Printed NinjaFlex[®]", 10th International Conference on Computational Methods and Experiments in Material and Contact Characterisation, (online) July 7 – 9, 2021.

HONORS AND AWARDS

- Recipient of the Howe Foundation Biomedical Fellowship for research into improvement of 3D printed prosthetic hands at the University of Nevada, Las Vegas, during Fall 2023 semester.
- Recipient of the Nuclear Engineering Doctoral Fellowship at UNLV funded by the US Nuclear Regulatory Commission, NRC, for the application and development of 3D printing in the nuclear field, May 2023
- Awarded 2nd place for best poster presentation of "Understanding Large Deflection Bending of 3D Printing Material", UNLV College of Engineering Graduate Celebration Poster Session, March 24, 2022.
- Finalist in the UNLV Rebel Grad Slam, 3-Minute Thesis Competition, for presenting research in hyperelastic TPU 3D printing filament and its application in prostheses, Fall 2020 and Fall 2022
- Recipient of the Top Tier Doctoral Graduate Research Assistantship to conduct research on underactuated hand prostheses, Fall 2020-Spring 2023